

DESIGN OF AN AUTONOMOUS LANDING CONTROL ALGORITHM FOR A
FIXED WING UAV

A THESIS SUBMITTED TO
THE GRADUATE SCHOOL OF NATURAL AND APPLIED SCIENCES
OF
MIDDLE EAST TECHNICAL UNIVERSITY

BY

VOLKAN KARGIN

IN PARTIAL FULFILLMENT OF THE REQUIREMENTS

FOR

THE DEGREE OF MASTER OF SCIENCE

IN

AEROSPACE ENGINEERING

OCTOBER 2007

Approval of the thesis:

**DESIGN OF AN AUTONOMOUS LANDING CONTROL
ALGORITHM FOR A FIXED WING UAV**

submitted by **VOLKAN KARGIN** in partial fulfillment of the requirements for
the degree of **Master of Science in Aerospace Engineering Department,**
Middle East Technical University by,

Prof. Dr. Canan Özgen
Dean, Graduate School of **Natural and Applied Sciences**

Prof. Dr. İsmail H. Tuncer
Head of Department, **Aerospace Engineering**

Dr. İlkey Yavrucuk
Supervisor, **Aerospace Engineering Dept., METU**

Examining Committee Members:

Prof. Dr. Ozan Tekinalp
Aerospace Engineering Dept., METU

Prof. Dr. Ünver Kaynak
Mechanical Engineering Dept., ETU

Assoc. Prof. Dr. Serkan Özgen
Aerospace Engineering Dept., METU

Asst. Prof. Dr. İlkey Yavrucuk
Aerospace Engineering Dept., METU

Dr. Volkan Nalbantoğlu
MGEO , ASELSAN

Date: _____

I hereby declare that all information in this document has been obtained and presented in accordance with academic rules and ethical conduct. I also declare that, as required by these rules and conduct, I have fully cited and referenced all material and results that are not original to this work.

Volkan KARGIN

ABSTRACT

DESIGN OF AN AUTONOMOUS LANDING CONTROL ALGORITHM FOR A FIXED
WING UAV

Kargin, Volkan

M.S., Department of Aerospace Engineering

Supervisor: Dr. İlkyay Yavrucuk

October 2007, 96 pages

This thesis concerns with the design and development of automatic flight controller strategies for the autonomous landing of fixed wing unmanned aircraft subject to severe environmental conditions. The Tactical Unmanned Aerial Vehicle (TUAV) designed at the Middle East Technical University (METU) is used as the subject platform. In the first part of this thesis, a dynamic model of the TUAV is developed in FORTRAN environment. The dynamic model is used to establish the stability characteristics of the TUAV. The simulation model also incorporates ground reaction and atmospheric models. Based on this model, the landing trajectory that provides shortest landing distance and smallest approach time is determined. Then, an automatic flight control system is designed for the autonomous landing of the TUAV. The controller uses a model inversion approach based on the dynamic model characteristics. Feed forward and mixing terms are added to increase performance of the autopilot. Landing strategies are developed under adverse atmospheric conditions and performance of three different classical controllers are compared. Finally, simulation results are presented to demonstrate the

effectiveness of the design. Simulation cases include landing under crosswind, head wind, tail wind, wind shear and turbulence.

Keywords: control autopilot UAV autonomous landing simulation flight dynamics

ÖZ

SABİT KANATLI BİR İHA'NIN OTOMATİK İNİŞ SİSTEMİ İÇİN KONTROL ALGORİTMASI TASARIMI

Kargin, Volkan

Yüksek Lisans, Havacılık ve Uzay Mühendisliği Bölümü

Tez Yöneticisi: Dr. İlkey Yavrucuk

Ekim 2007, 96 sayfa

Bu tez çalışması, sabit kanatlı bir İnsansız Hava Aracının (İHA) sert hava koşulları altında otonom inişi için otomatik uçuş kontrol stratejileri tasarımı ile ilgilenmektedir. Platform olarak Orta Doğu Teknik Üniversitesi'nde tasarlanan Taktik İnsansız Hava Aracı kullanılmıştır. Bu tezin ilk kısmında bu İHA'nın dinamik modelinin FORTAN ortamında geliştirilmesi anlatılmaktadır. Bu model İHA'nın kararlılık özelliklerini saptamak için kullanılmıştır. Simulasyon modeli aynı zamanda yer tepkileri ve atmosfer modellerini de içermektedir. Bu model üzerinden, en kısa iniş mesafesi ve en düşük yaklaşma zamanını sağlayacak iniş yörüngesi belirlenmiştir. Daha sonra İHA'nın otomatik inişi için bir uçuş kontrol sistemi tasarlanmıştır. Kontrolcüde, dinamik modelin karakteristikleri üzerine kurulu tersine çevrilmiş kontrolcü yaklaşımı kullanılmıştır. Kontrolcünün performansını arttırmak için ileri besleme terimleri eklenmiştir. Elverişsiz hava koşullarına karşı iniş stratejileri geliştirilmiş ve üç farklı klasik kontrolcününün performansları karşılaştırılmıştır. Son olarak, simulasyon sonuçları kontrolcünün etkinliğini göstermek için sunulmuştur. Simulasyon durumları yan rüzgar, baş rüzgar, arka rüzgar, hızı değişken olan

rüzgar ve türbülansı içermektedir.

Anahtar Kelimeler: kontrol otopilot İHA otonom iniş simülasyon uçuş dinamiği

aieme...

ACKNOWLEDGMENTS

I would like to express my sincere gratitude to Dr. İlkey Yavrucuk who supervised in all steps of this work and provided the necessary resources of his knowledge and experience. His energy, support and guidance helped me to complete this work.

Special thanks to Dr. Altan Kayran for his assistance in the UAV project. I am very glad to have a chance working with him. Thanks to Prof.Dr. Nafiz Alemdaroğlu for giving me the opportunity to work on METU TUAV. I would like to thank Dr. Oğuz Uzol, Dr. Volkan Nalbantoğlu and Dr. Abhay Pashilkar for their suggestions.

I wish to state my thanks to the other members of the UAV project, Fikri Akçalı, Sercan Soysal, Serhan Yüksel and Hüseyin Yiğitler for their assistance. I definitely learned a lot from them during sleepless nights.

I appreciate the useful discussions we had with Tahit Turgut, Onur Tarımcı, Deniz Yılmaz and Emrah Zaloğlu during this thesis. Thanks to Eser Kübalı for implementation of the dynamic model to FlightGear. I specially thank Mustafa Kaya who always responded me when I requested help.

I also thank to Erman Özer, Gökhan Şimşek, Emre Altuntaş, Zeynep Kocabaş, Ozan Göker, Tolga Yapıcı and Levent Çomoğlu (a.k.a "aejackals") who have boosted me with positive energy in all periods of my university life.

Finally, I would like to express my deepest thanks to my parents and grandmother for their endless support throughout my life. This thesis wouldn't be done without them.

TABLE OF CONTENTS

ABSTRACT	iv
ÖZ	vi
DEDICATON	viii
ACKNOWLEDGMENTS	ix
TABLE OF CONTENTS	x
LIST OF TABLES	xiii
LIST OF FIGURES	xiv
LIST OF SYMBOLS	xviii
CHAPTERS	
1 INTRODUCTION	1
2 6-DOF MATHEMATICAL MODELING	6
2.1 Platform	6
2.2 Aerodynamic Model	7
2.3 Propulsion Model	10
2.4 Mass-Inertia Model	14
2.5 Atmospheric Model	14
2.6 Wind-Turbulence Model	15
2.7 Actuator Model	18
2.8 Landing Gear Model	19
2.9 Ground Reaction Modeling	20
2.10 Reference Frames, Coordinate Systems and Transformations	22

2.11	6-DOF Equations of Motion	23
2.12	Linear Equations of Motion and Analysis	24
2.12.1	Longitudinal Dynamics	24
2.12.2	Lateral Dynamics	26
2.13	Open Loop Simulation	28
3	LANDING TRAJECTORY GENERATION	31
3.1	Commanded Trajectory Generation	31
3.1.1	Landing Phases	31
3.1.1.1	Descent Phase	31
3.1.1.2	Flare Phase	33
3.1.1.3	Taxi Phase	34
3.2	Landing Maneuvers	34
4	CONTROLLER DESIGN	36
4.1	Onboard Sensors	36
4.2	Inner Loop Controller Design	37
4.2.1	Model Inversion Control	37
4.2.2	Command Filter	38
4.2.3	Attitude Controller	39
4.3	Longitudinal Outer Loop Controller	40
4.3.1	Forward Velocity Controller	40
4.3.2	Altitude Control	42
4.4	Lateral Outer Loop Controller	44
4.4.1	Lateral Trajectory Control	44
4.4.1.1	Lateral Trajectory Controller A	44
4.4.1.2	Lateral Trajectory Controller B	48
4.4.1.3	Lateral Trajectory Controller C	51
4.4.1.4	Comparison of Lateral Controllers	53
4.4.2	Decrab Control	53

5	SIMULATION RESULTS	57
5.1	Case 1: No Wind, No Turbulence	58
5.2	Case 2: 15 m/s Head Wind + Turbulence	64
5.3	Case 3: 2.5 m/s Tail Wind + Turbulence	71
5.4	Case 4: 10 m/s Crosswind + Turbulence	78
5.5	Case 5: Windshear + Turbulence	85
6	CONCLUSION	92
	REFERENCES	95

LIST OF TABLES

TABLES

Table 2.1	Specifications of the METU Tactical UAV	7
Table 2.2	Longitudinal non-dimensional derivatives of the A/C	10
Table 2.3	Lateral non-dimensional derivatives of the A/C	10
Table 2.4	Geometric properties of the METU TUAV propeller sections	13
Table 2.5	Mass and inertias of the A/C	14
Table 2.6	Damping and spring coefficients of the landing gears	20
Table 2.7	Position of the wheels w.r.t the cg in the body axis($x_{cg} = 0.3MAC$)	20
Table 2.8	Longitudinal mode characteristics	26
Table 2.9	Dutch roll mode characteristics	27
Table 2.10	Roll and spiral mode characteristics	28
Table 4.1	Command filter characteristics	38
Table 4.2	Inner loop gains	39
Table 4.3	Transient characteristics of the inner loop controller	39
Table 4.4	h controller gains	43
Table 4.5	y controller gains	50
Table 5.1	Competitor study on wind limits of UAVs	57

LIST OF FIGURES

FIGURES

Figure 2.1	METU Tactical UAV	7
Figure 2.2	Variation of the A/C lift coefficient with angle of attack for different velocities	9
Figure 2.3	Variation of the A/C pitching moment coefficient with angle of attack for different center of gravity locations	9
Figure 2.4	Change in lift, drag and pitching moment coefficients with altitude due to ground effect	11
Figure 2.5	Power required and SFC vs RPM of Limbach L275E[8]	12
Figure 2.6	Thrust and power coefficients of 11”x7” propeller	13
Figure 2.7	Comparison of propeller section 6 with NACA 3410 airfoil	13
Figure 2.8	Thrust and power coefficients of METU TUAV propeller	14
Figure 2.9	Variation of A/C mass and cg location with time.	15
Figure 2.10	Bode plots of velocity shaping filters of Dryden turbulence model	17
Figure 2.11	The variation of the wind speed with altitude in the wind shear model	18
Figure 2.12	Orientation of tire frame	20
Figure 2.13	Variation of μ_y with η	21
Figure 2.14	Friction forces acting on the UAV	22
Figure 2.15	Response of the system to elevator input	29
Figure 2.16	Response of the system to aileron input	30
Figure 2.17	Position change of the UAV in time due to 2m/s initial side velocity disturbance	30
Figure 3.1	Conceptual landing trajectory	32
Figure 3.2	Minimum landing velocities for different γ	33
Figure 3.3	Flare maneuver	34
Figure 3.4	Landing Procedure	35
Figure 4.1	Pitch channel command filter	38
Figure 4.2	Pitch channel autopilot	40
Figure 4.3	Response of the system to step input	41

Figure 4.4	Longitudinal autopilot	41
Figure 4.5	Forward velocity command filter	42
Figure 4.6	Response of the system to velocity input	42
Figure 4.7	Comparison of autopilots with and without feeding \dot{h} forward (trajectory with constant flight angle)	43
Figure 4.8	Comparison of autopilots with and without feeding \dot{h} forward (sinusoidal trajectory)	44
Figure 4.9	Effect of flaps on longitudinal autopilot	45
Figure 4.10	Lateral Controller Architecture A	45
Figure 4.11	Lateral guidance law introduced by [16]	46
Figure 4.12	Simulation results for different k	47
Figure 4.13	Simulation results for different k under crosswind	47
Figure 4.14	Effect of rudder-aileron mixing under crosswind	48
Figure 4.15	Effect of rudder-aileron mixing under turbulence	48
Figure 4.16	Lateral controller architecture B	49
Figure 4.17	Application of control law B to a circular trajectory	49
Figure 4.18	Comparison of autopilots with and without feeding $\dot{\psi}$ forward (circular trajectory)	51
Figure 4.19	Description of the maneuver in figure 4.20	51
Figure 4.20	Comparison of autopilots with and without feeding $\dot{\psi}$ forward (circular trajectory 2)	52
Figure 4.21	Lateral controller architecture C	52
Figure 4.22	Comparison of the lateral controllers following a straight trajectory (no wind)	54
Figure 4.23	Comparison of the lateral controllers following a straight trajectory (10 m/s crosswind)	54
Figure 4.24	Comparison of yaw and roll angle controls of autopilots under 10 m/s crosswind	55
Figure 4.25	Decrab control by rudder	55
Figure 4.26	Decrab control by aileron	55
Figure 4.27	Response of yaw angle at decrab maneuver	56
Figure 4.28	Response of roll angle at decrab maneuver	56
Figure 5.1	Longitudinal trajectory	58
Figure 5.2	Altitude error	59
Figure 5.3	Lateral trajectory	59
Figure 5.4	Forward velocity	60
Figure 5.5	Flare maneuver	60
Figure 5.6	Euler angles	61
Figure 5.7	Angle of attack and sideslip angle	61

Figure 5.8	Body angular rates	62
Figure 5.9	Side velocity and descend rate	62
Figure 5.10	Control surface deflections	63
Figure 5.11	Wind profiles	64
Figure 5.12	Longitudinal trajectory	65
Figure 5.13	Altitude error	65
Figure 5.14	Lateral trajectory	66
Figure 5.15	Forward velocity	66
Figure 5.16	Flare maneuver	67
Figure 5.17	Euler angles	67
Figure 5.18	Angle of attack and sideslip angle	68
Figure 5.19	Body angular rates	68
Figure 5.20	Side velocity and descend rate	69
Figure 5.21	Control surface deflections	70
Figure 5.22	Wind profiles	71
Figure 5.23	Longitudinal trajectory	72
Figure 5.24	Altitude error	72
Figure 5.25	Lateral trajectory	73
Figure 5.26	Forward velocity	73
Figure 5.27	Flare maneuver	74
Figure 5.28	Euler angles	74
Figure 5.29	Angle of attack and sideslip angle	75
Figure 5.30	Body angular rates	75
Figure 5.31	Side velocity and descend rate	76
Figure 5.32	Control surface deflections	77
Figure 5.33	Wind profiles	78
Figure 5.34	Forward velocity and rpm for $\gamma=3.5\text{deg}$	78
Figure 5.35	Longitudinal trajectory	79
Figure 5.36	Altitude error	80
Figure 5.37	Lateral trajectory	80
Figure 5.38	Forward velocity	81
Figure 5.39	Flare maneuver	81
Figure 5.40	Euler angles	82
Figure 5.41	Angle of attack and sideslip angle	82
Figure 5.42	Body angular rates	83
Figure 5.43	Side velocity and descend rate	83
Figure 5.44	Control surface deflections	84

Figure 5.45 Wind profiles	85
Figure 5.46 Longitudinal trajectory	86
Figure 5.47 Altitude error	86
Figure 5.48 Lateral trajectory	87
Figure 5.49 Forward velocity	87
Figure 5.50 Flare maneuver	88
Figure 5.51 Euler angles	88
Figure 5.52 Angle of attack and sideslip angle	89
Figure 5.53 Body angular rates	89
Figure 5.54 Side velocity and descend rate	90
Figure 5.55 Control surface deflections	91

LIST OF SYMBOLS

ROMAN SYMBOLS

A	System matrix
B	Input matrix
c	Damping coefficient
C_D	Drag coefficient
C_L	Lift coefficient
C'_L	Rolling moment coefficient
C_M	Pitching moment coefficient
C_N	Yawing moment coefficient
C_p	Power coefficient
C_t	Thrust coefficient
FC	Fuel consumption
h	Reference altitude
I	Inertia
J	Advance ratio
k	Spring coefficient
k, K	Controller gain
m	Mass
n	Revolution per second
p	Body roll rate
P	Pressure
P_A	Power available
P_R	Power required
Q	Body pitch rate
r	Body yaw rate
R	Universal gas constant
RPM	Revolution per minute
SFC	Specific fuel consumption
U	Body velocity in x-direction
V	Body velocity in y-direction
W	Body velocity in z-direction
X	Position of A/C in north direction
Y	Position of A/C in east direction
Z	Altitude of A/C

GREEK SYMBOLS

α	Angle of attack
β	Sideslip angle
ϕ	Roll angle
ψ	Yaw angle
ρ	Density
θ	Pitch angle
δ_e	Elevator deflection angle
δ_f	Flap deflection angle
δ_a	Aileron deflection angle
δ_r	Rudder deflection angle
μ	Friction coefficient, mean wind speed
σ	Standard deviation
ω	Angular rates
ν	Body velocities

SUBSCRIPTS

∞	Freestream values
com	Commanded values(Input of command filters)
c	Commanded values(Output of command filters)
des	Desired values
ref	Reference values
cr	cruise condition values
A	Aerodynamic forces and moments
T	Propulsive forces and moments
G	Ground forces and moments

CHAPTER 1

INTRODUCTION

The term Unmanned Aerial Vehicle (UAV) is defined as a type of powered aircraft that does not carry a human pilot, uses aerodynamic forces to provide lift, can fly autonomously or be remotely controlled, can be expendable or recoverable, and can carry a lethal or non-lethal payload[13]. The demand on UAVs has increased significantly in the recent years. They are preferred over piloted aircrafts due to:

- Low cost
- Multi mission capability
- Simplicity
- Ability to accomplish dirty and dangerous missions that can not be done by piloted A/C

UAVs are being used in military applications for missions like observation, surveillance, reconnaissance, air support and pipeline monitoring for many years. Their adaptation to civilian missions have become more mature in the recent years. Some of their civilian application fields are search and rescue, disaster monitoring, meteorological data acquisition and maritime monitoring.

Various landing techniques are developed for UAVs according to their size and mission profiles. Beside wheeled landing, methods like belly landing, parachute- airbag recovery, deep stall, sky-

hook recovery, net recovery and parafoil are used in UAV landing. Although all these solutions provide short landing distances and do not require good piloting skills, wheeled landing is still the most popular technique for landing tactical UAVs. This type of landing is preferred due to size constraints, reliability issues and control effectiveness. Aircrafts have to accomplish unique maneuvers with very high accuracy in wheeled landing. Data collected by Boeing showed that 54 percent of fatal large commercial jet plane accidents have occurred during approach and landing [34]. It is also noted that this ratio is very high since landing and approach covers only 4 percent of the total flight time. The reasons for these accidents are explained in three major topics [35];

- Weather factors
- Crew technique/Decision factors
- System factors

”Weather factors” are effects of environmental conditions on the aircraft and the runway. ”Crew technique/Decision factors” are pilot and crew errors. ”System factors” are malfunctions of aircraft subsystems.

Automatic landing of an A/C increases the overall autonomy of the system and adds consistency. Landing autopilot guarantees greater safety and simplicity reducing the load on pilot and crew in operations. It also increases wind limits of the A/C and enables landing under high winds, turbulence and wind shear. Hence, the design for an autopilot to be used during landing is desired, however is a challenge.

Creating a dynamic model of an aircraft is an important milestone in autopilot design. Dynamic models include detailed information about the system characteristics based on aerodynamics, propulsion system, mass-inertia properties and actuator dynamics. Moreover, ground reactions and landing gear models should be added to the system to demonstrate landing. There are studies in literature that concerns the modeling of UAVs. In Jodeh *et. al.* [1], a SIG Rascal 110 radio controlled aircraft is modeled in the MATLAB/Simulink environment. In this study, the aerodynamic and propulsion databases are created based on semi-empirical methods. Inertia

of the aircraft is found through experiments. Simulations build using such methods offer low cost and time efficient solutions for small UAVs. In a paper by Karakaş *et. al.* [36], the static aerodynamic derivatives of a Medium Altitude Long Endurance(MALE) UAV are obtained by using computational fluid dynamics(CFD), whereas the dynamic derivatives are found using semi-empirical formulae. CFD results are more reliable than empirical methods, but, obtaining them requires more time. In the work of Ippolito *et. al.* [37], dynamic characteristics of the system is obtained from flight testing. The modes of the one quarter scale of a radio controlled Cessna 182 is excited by commanding a series of inputs. The data collected by an on-board flight computer were post-processed with a least-squares regression in frequency domain to identify the system. System identification using flight tests might result in accurate data. However, it can be expensive for larger UAVs and many of the maneuvers might not be possible to be risked. Ground reaction dynamics and landing gears of the Kingfisher UAV are modeled in [18]. The damping and spring coefficients of the landing gears are adjusted by measuring time to half amplitude from experiments.

Autopilots are used to stabilize a system if it is unstable and adjust the response to a desired shape. In classical linear feedback control theory, A/C dynamics are linearized around a trim point and feedback gains that will provide the required performance are found. Since A/C dynamics are non-linear, this procedure is applied to several other trim conditions and a gain scheduling approach is used to cover the whole flight range. The autopilot may not be able to control the A/C if the dynamics of the system no longer matches the design condition, for instance when unforeseen events occur (control surface failure, damage on the aircraft, etc.).

In modern control theory, some methods like adaptive control, robust control, fuzzy logic are introduced to account for the uncertainties caused by the non-linearities. The transition from forward flight to stationary hover of a fixed wing UAV is achieved by Johnson *et. al.* [28] by adding an online learning neural network to a model inversion based classical controller to account for uncertainties. Although the dynamics of the UAV is very different in hover and forward flight, the neural network is able to compensate for the difference in the mentioned study.

Landing autopilots usually consist of an inner loop and an outer loop. In the inner loop, the faster dynamics which are rotational dynamics are controlled. Position and velocities are controlled in the outer loop. A challenging part of the landing maneuver is the decrab maneuver which is necessary to align the A/C heading with the runway just before touchdown. During this maneuver, roll and yaw angles are commanded directly instead of position or velocity.

Recent studies concern the design of automatic landing systems and strategies. In a study by Riseborough of BAE Systems[18], hardware in loop landing simulations of the Kingfisher UAV under crosswind are presented. Similarly the automatic landing of the Heron UAV under crosswinds is investigated in Attar *et. al.* [19]. Another popular method is the recovery of the UAV through a net. In [21], the net recovery of the Silver Fox UAV onto a moving ship has been studied. Longitudinal control of the landing of the SWAN UAV is studied in [23]. Some studies also incorporate advanced controller design. In [15], online learning neural networks are added to the controller of a fighter aircraft to cope with actuator failures and severe winds during landing. Feed forward terms are integrated to feedback loops to increase the performance of the autopilot. Rosa *et. al.* [22] designed controllers for the landing of a small UAV using H_2 robust controller. Comparison of neural aided landing controllers are compared with classical controllers for heavy transport aircrafts in Hsiao *et. al.* [24].

This thesis is organized as follows: Chapter 2 describes the geometric properties and details the 6-DOF modeling of the platform. Aerodynamics of the system is modeled using semi-empirical formulae. Engine model is created from test data. Propeller is modeled from blade element theory(BET). Inertia properties are obtained from the modeling program CATIA. Landing gear and ground reaction models are included to simulate touchdown and taxi. In addition, atmosphere and wind and turbulence models are shown in this part. After the model is created, the system is linearized around a cruise condition and the open loop characteristics of the system are investigated. Chapter 3 addresses the design of the landing trajectory and establishing the optimum landing parameters. It also describes the landing maneuvers. Chapter 4 presents the controller design. Model inversion based classical controllers are used in the design. Longitudinal and lateral dynamics are treated as if they are uncoupled and controlled

individually. Several algorithms are investigated in the lateral channel and their results are compared. The effect of the flaps and the feed forward terms on the closed loop system are also presented. Chapter 5 presents simulation results for different weather conditions. Simulation results include landing for a no wind case, a turbulent weather with crosswind, tail wind, head wind and windshear. Chapter 6 presents conclusions and recommendations for future work. The scope of this thesis can be summarized as the following:

- Develop an accurate dynamic model of the METU Tactical UAV. The model should be generic to cope with future design changes.
- Investigate open loop characteristics of the UAV.
- Obtain the flight trajectory that the UAV should follow for the shortest landing time and shortest landing distance.
- Design longitudinal and lateral autopilots that will land the UAV in severe environmental conditions without exceeding desired parameters.

CHAPTER 2

6-DOF MATHEMATICAL MODELING

In this chapter the generation of the dynamic model of the METU TUAV is presented.

Modeling is an important step in controller design and analysis. An accurate dynamic model leads to a more accurate autopilot. A 6-DOF model of the METU UAV is created for this purpose. The model includes aerodynamic, propulsion databases, ground dynamics, mass-inertia, landing gear and wind- turbulence models.

2.1 Platform

A UAV project was started in Middle East Technical University in 2004 with the support of State Planning Department. Under this project, a short range UAV, METU TUAV, is planned to be designed and manufactured. Currently, design of the UAV is complete and the first prototype is under production. A mock-up of the UAV is shown in Figure 2.1. The mission of this UAV is defined as the aerial observation of an area and the transmittal of related data to the ground station in real time. UAV will carry a Forward Looking Infrared (FLIR) camera. It will also be used as a test-bed for research and development at the Middle East Technical University. The UAVs propulsion system consists of a 21 HP Limbach piston engine and a pusher propeller. It has wheeled take-off and landing capability with its tricycle landing gear. Control surfaces of the METU TUAV include a starboard aileron, port aileron, starboard rudder, port

rudder, elevator, starboard flap and port flap. In addition, the throttle and the nose landing gear can be controlled. The specifications of the METU TUAV are shown in Table 2.1



Figure 2.1: METU Tactical UAV

Table 2.1: Specifications of the METU Tactical UAV

Wing Span:	4.3 m
Length:	1.8 m
Maximum Take-off Weight:	105 kg
Payload Weight:	25 kg
Cruise Velocity:	40-35 m/s
Maximum Range:	150 km
Maximum Endurance:	4-3 hr
Operation Altitude:	3000 m
Payload:	FLIR Camera
Propulsion:	21 HP Two Cylinder Gasoline Engine

2.2 Aerodynamic Model

There are several ways to obtain aerodynamic coefficients of aircraft. These coefficients can be obtained based on flight tests, wind tunnel tests, CFD or semi-empirical methods. Flight tests are impossible during the initial stages of design. Time and cost constraints prevent

the use of wind tunnel tests and CFD solutions. Semi-empirical methods are used to create the aerodynamic database. Procedures for large aircrafts are well documented. However, the databases are not sufficient for smaller aircrafts. In [1], it is shown that methods of USAF DATCOM[2] are also applicable to small UAVs. Here, aerodynamic coefficients are calculated individually for the components of the A/C using geometric properties:

$$C_{A/C} = C_{wb} + C_{h.tail} + C_{v.tail} + \dots \quad (2.1)$$

Any future design change on the UAV can be adapted into the code fairly quickly.

Longitudinal and lateral-directional aerodynamics are investigated individually. Longitudinal non-dimensional coefficients, lift coefficient (C_L), drag coefficient (C_D) and pitching moment coefficient (C_M), are functions of angle of attack (α), forward speed (u), pitch rate (q), elevator deflection (δ_e) and flap deflection (δ_f):

$$[C_L, C_D, C_M] = f(\alpha, u, q, \delta_e, \delta_f) \quad (2.2)$$

The aircraft angle of attack is defined as the angle between the x-body axis and the projection of the freestream velocity onto the body x-z plane.

Most of the attention is paid to stall modeling in aerodynamic model. Experimental data of the wing section lift coefficients are corrected for 3-D effects, Reynolds number and body geometry from [2] and [3]. Aircraft lift coefficient (C_L) vs angle of attack (α) graphs for different velocities are shown in 2.2. The change in lift coefficient with velocity is very small since compressibility effects are not effective in these flight velocities. METU TUAV has a stall angle of attack of 12 degrees with a maximum C_L of 1.5. For the drag coefficient calculation, parasite drag of every component is estimated based on their shapes and frontal areas from Refs. [4] and [5]. Then, induced drag term is added to the drag equation from [4]. The drag coefficient is calculated from equation 2.3.

$$C_D = 0.02381 + 0.04175C_{L_{wb}}^2 + 0.024\alpha^2 + 0.21\alpha^3 \quad (2.3)$$

The pitching moment coefficient, C_M , is calculated by taking the moment of the lift forces around the cg. The contribution of drag on pitching moment is neglected. The variation of

C_M with α for three different cg locations are given in Figure 2.3. As the cg moves forward, C_{M_α} increases as expected. Other derivatives that contribute to the longitudinal coefficients are taken constant and are given in Table 2.2.

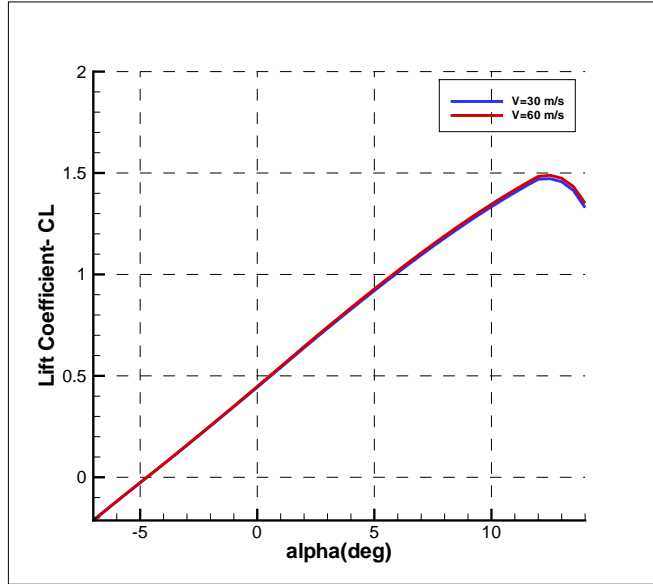


Figure 2.2: Variation of the A/C lift coefficient with angle of attack for different velocities

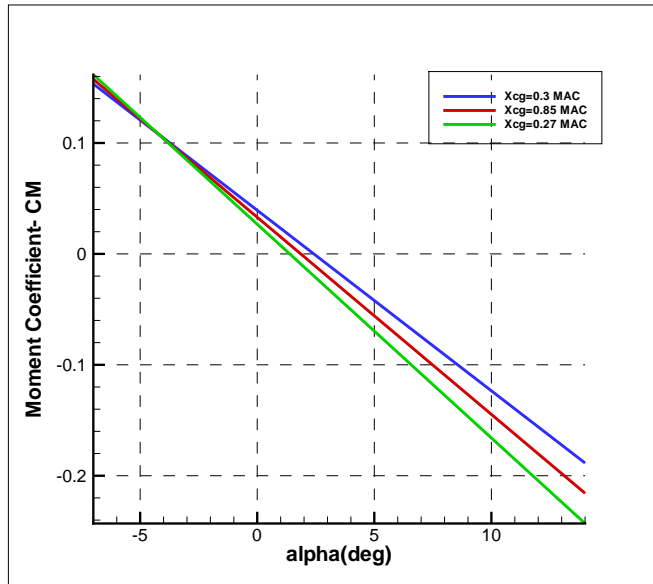


Figure 2.3: Variation of the A/C pitching moment coefficient with angle of attack for different center of gravity locations

Lateral non-dimensional coefficients, sideforce coefficient(C_Y), rolling moment coefficient(C'_L) and yawing moment coefficient(C_N), are functions of sideslip angle(β), roll rate(p), yaw rate(r),

Table 2.2: Longitudinal non-dimensional derivatives of the A/C

	C_L	C_D	C_M
u	0	0	0
q	6	0	-13.3
$\dot{\alpha}$	1.46	0	-4.38
δ_e	0.39	0	-1.17
δ_f	0.69	0	0

aileron deflection(δ_a) and rudder deflection(δ_r).

$$[C_Y, C'_L, C_N] = f(\beta, p, r, \delta_a, \delta_r) \quad (2.4)$$

Lateral coefficients are assumed to be changing linearly with these parameters. So, lateral aerodynamic derivatives are constant and given in Table 2.3.

Table 2.3: Lateral non-dimensional derivatives of the A/C

	C_Y	C'_L	C_N
β	-0.284	-0.029	0.049
p	-0.038	0.87	-0.065
r	0.127	0.158	-0.065
δ_a	0	0.787	-0.024
δ_r	0.31	0.034	-0.114

The ground effect is modeled according to [7]. The method replaces the ground with a mirror image of the aircraft and real and imaginary wings are assumed to be vortex systems with equal and opposite strengths. The change in lift, drag and pitching moment coefficients with altitude due to ground effect is shown in Figure 2.4. Ground effect ultimately increases lift, decreases drag and produces additional nose down pitching moment due to increased tail lift. The influence of ground effect increases with decreasing altitude, however, it is not very strong even when the aircraft has touched down. The primary reason for this is the high wing configuration of the UAV.

2.3 Propulsion Model

The propulsion model of the METU UAV consists of an engine model and a propeller model. The purpose of modeling the engine is to find the fuel consumption and determine the RPM limits. This information is used to update the mass and center of gravity(cg) position. Engine

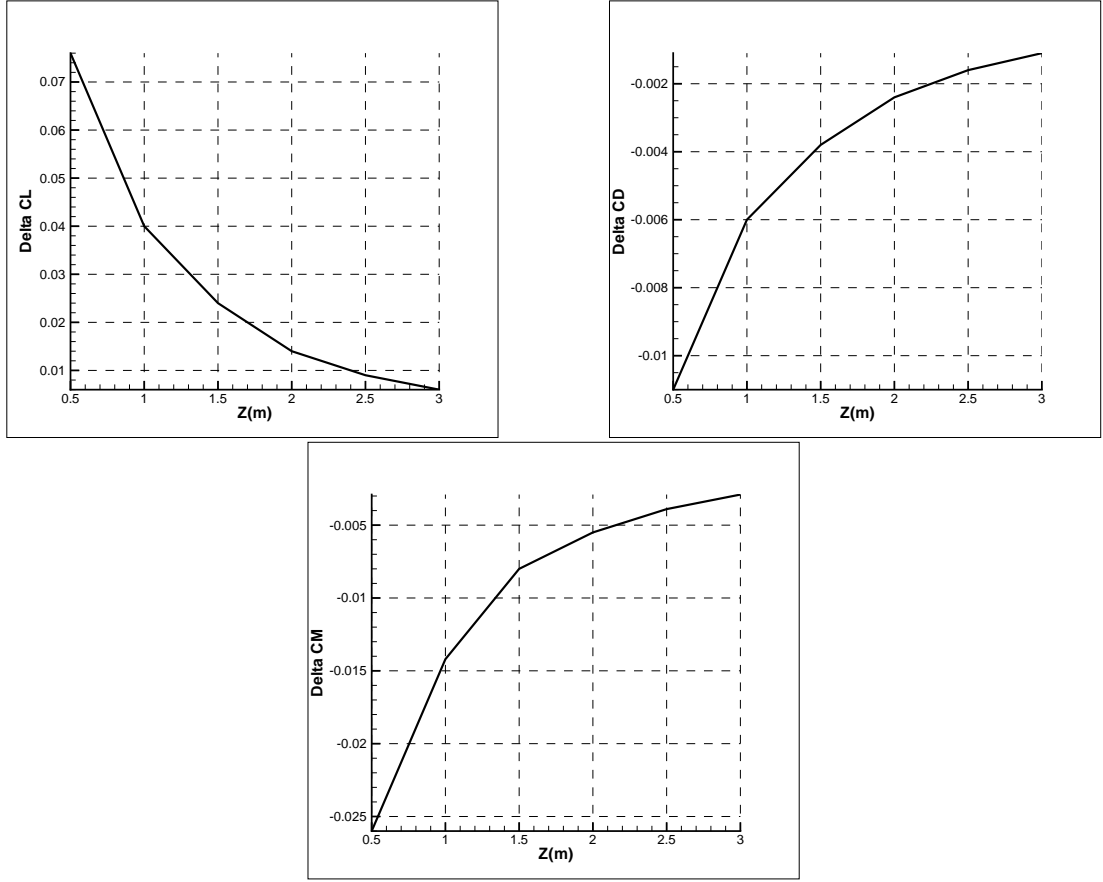


Figure 2.4: Change in lift, drag and pitching moment coefficients with altitude due to ground effect

data is obtained from the manufacturer, shown in Figure 2.5

This data includes variation of specific fuel consumption(SFC) and power required(P_R) with RPM between 4000 and 7000. Simulations show that this interval is the nominal operating RPM of the engine during cruise and climb. Variations of power and SFC for RPM less than 4000 is not provided and they are assumed to be changing linearly with RPM. Fuel consumption(FC) can be found from;

$$FC = SFC \cdot P_R \quad (2.5)$$

Figure 2.5 is valid for standard sea level(SSL) conditions. Maximum power available, P_A , decreases with decreasing density in air breathing engines. So, engine may not be able to create enough power to run the engine at desired RPM at higher altitudes. P_A at an altitude, h , is obtained using equation 2.6. P_{A_h} is used to determine maximum RPM.

$$P_{A_h} = P_{A_{SSL}} \frac{\rho_h}{\rho_{SSL}} \quad (2.6)$$

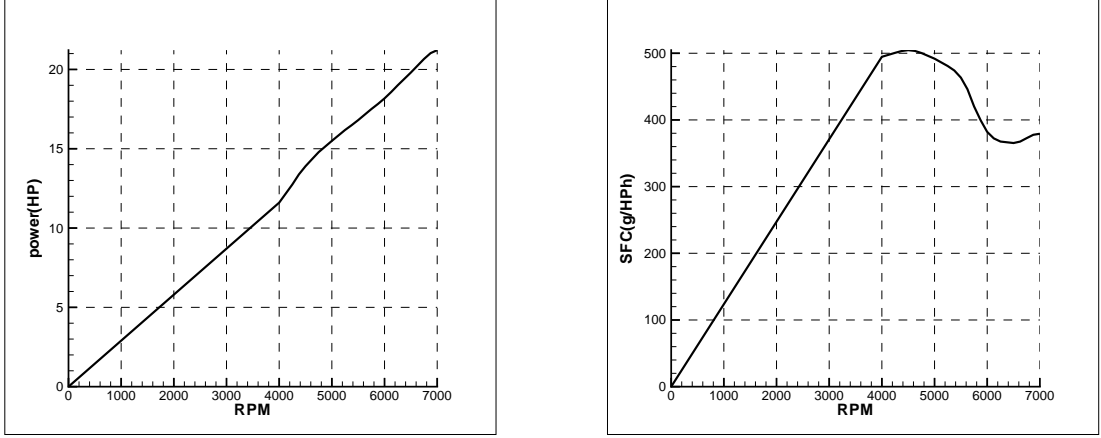


Figure 2.5: Power required and SFC vs RPM of Limbach L275E[8]

Propeller is modeled by blade element theory(BET)[9]. In BET, lift and drag generated by propeller sections are calculated and summed to find thrust and torque. Typical propeller characteristics are represented by variations of thrust and power coefficients, C_t and C_p with advance ratio, J .

$$C_t = \frac{Thrust}{\rho n^2 D^4} \quad (2.7)$$

$$C_p = \frac{Power}{\rho n^3 D^5} \quad (2.8)$$

$$J = \frac{V_\infty}{nD} \quad (2.9)$$

The propeller model subroutine is verified by comparing results of the 11" x7" propeller with experimental data.(Figure 2.6) The geometric data of propeller and experimental results are obtained from [14].

The propeller model gives fairly accurate results for advance ratios greater than 0.4. There are some differences in the model results for advance ratios between 0.2 and 0.4. The lift curve slope becomes non-linear in this advance ratio interval. Therefore the errors of the X-foil results in the non-linear region can be a reason for this shift. It should be mentioned that the advance ratio reduces to this interval only in takeoff, climb at high angles or in more challenging regimes of the flight envelope like the stall.

The propeller sections of the METU TUAV are obtained from 3-D drawings. The pitch angle and the distance of the sections are measured from the propeller root. Airfoils are approximated to NACA 4 digit series by maximum thickness, maximum camber and maximum camber lo-

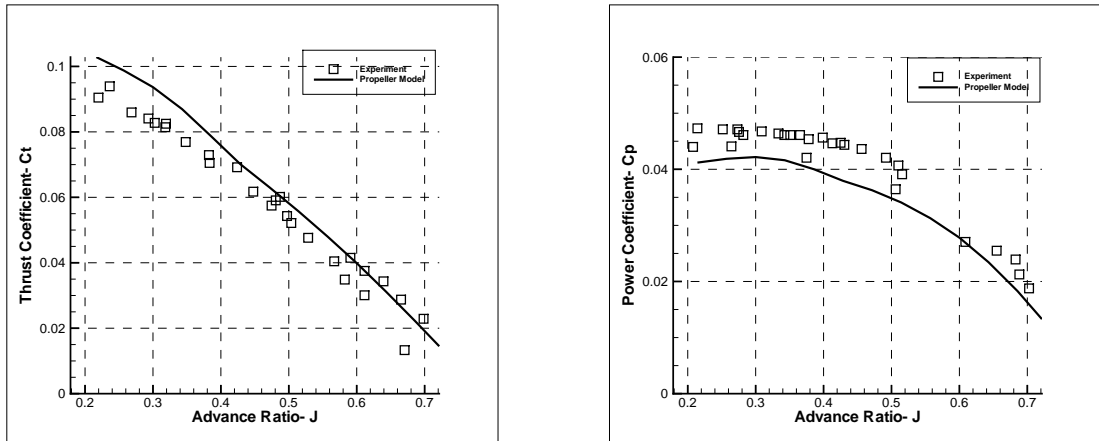


Figure 2.6: Thrust and power coefficients of 11''x7'' propeller .

cation to smoothen the airfoils [14]. Geometric properties of the propeller sections are given in Table 2.4. Approximating propeller sections by 4 digit series NACA airfoils is a reasonable assumption as shown in Figure 2.7. The X-foil analysis tool is used to obtain variation of lift and drag with angle of attack [10]. Thrust and power coefficients are found using BET as shown in Figure 2.8.

Table 2.4: Geometric properties of the METU TUAV propeller sections

Section No	Radial Distance (cm)	Pitch angle (deg)	Chord (cm)	Approximated NACA
1	9.9	30	6.6	1344
2	14.9	25	7	5421
3	19.8	21	6.6	5416
4	24.8	18	5.6	4413
5	29.7	15	3.8	3411
6	33	14	2.4	3410

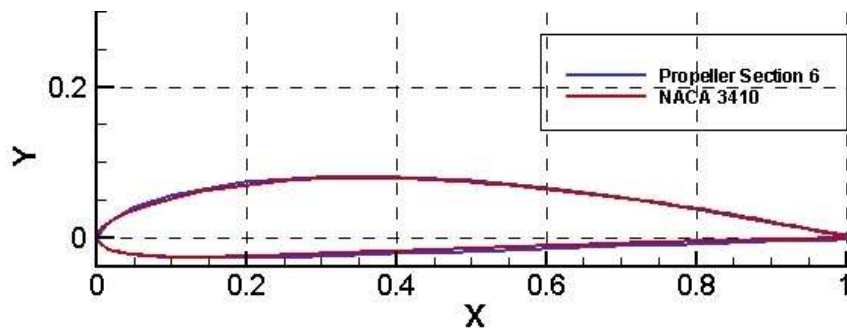


Figure 2.7: Comparison of propeller section 6 with NACA 3410 airfoil

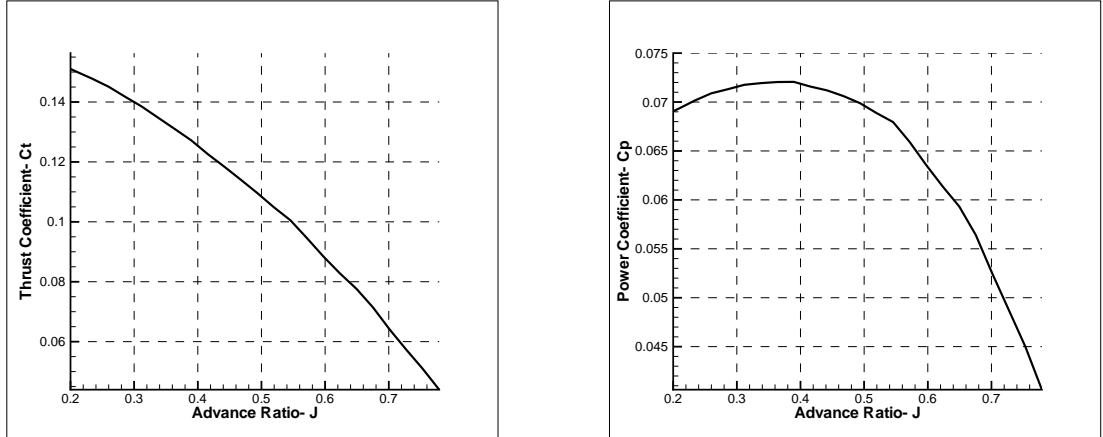


Figure 2.8: Thrust and power coefficients of METU TUAV propeller .

2.4 Mass-Inertia Model

The mass of the aircraft and the cg positions are updated in every iteration using the information send from the engine model. The variation in the pitching moment coefficient due to the cg shift is significant for long simulations. Inertias are taken constant throughout the flight. The UAV's maximum take-off gross weight, fuel weight and inertia properties are given in Table 2.5. The change in gross weight and cg location with time at a velocity of 40 m/s and altitude of 3000 m is shown in Figure 2.9. After 1000 seconds of flight UAV has consumes 1.5 kg of fuel. The effect of this loss to cg location is very small. The center of gravity moves forward in time which increases longitudinal stability.

Table 2.5: Mass and inertias of the A/C

$m_{MTOW}(kg)$	$m_{fuel}(kg)$	$I_{xx}(kgm^2)$	$I_{yy}(kgm^2)$	$I_{zz}(kgm^2)$	$I_{xz}(kgm^2)$
105	15	37.58	34.12	67.04	-6.91

2.5 Atmospheric Model

The performance of aircraft vary with changes with the atmospheric properties. The primary parameter effecting the aircraft performance is the density of the air. The aerodynamic and thrust forces are linearly proportional with density. The influence of air temperature, pressure, viscosity are small in low speed aerodynamics. The properties of the atmosphere can be expressed in terms of the altitude in a standard atmosphere model [33]. It is assumed that

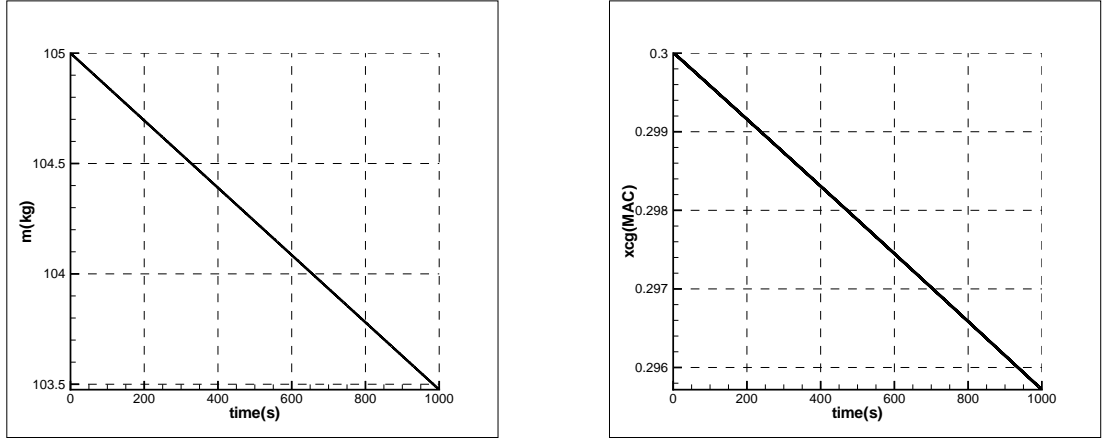


Figure 2.9: Variation of A/C mass and cg location with time.

the temperature changes linearly with altitude in the first 10 km of the atmosphere which includes flight range of METU TUAV. The temperature at any altitude can be determined if two reference values are known. The air pressure is determined from the following formula[33]:

$$P_h = P_{SSL} \frac{T_h}{T_{SSL}}^{(-g/(R\lambda))} \quad (2.10)$$

where $\lambda = \frac{T_h - T_{SSL}}{h}$, R is the universal gas constant, T is the temperature, P is the pressure.

Density is found from 2.11 using ideal gas assumption.

$$\rho = \frac{P}{RT} \quad (2.11)$$

2.6 Wind-Turbulence Model

The wind speed and direction is an input to the model.

The turbulence is created by passing white noise signal through properly designed shaping filters. Dryden turbulence model is implemented from MIL-F-8785C [26]. Velocity components are calculated in wind axis and then transformed into body axis.

White noise is generated by transforming uniformly distributed random numbers into normally distributed random numbers by Box-Muller transformation.[6]

$$v_{wind} = \mu + \sigma \sqrt{-2 \ln x_1} \cos 2\pi x_2 \quad (2.12)$$

μ =mean wind speed

σ =standard deviation in wind speed

x_1 and x_2 are randomly generated numbers between 1 and 0.

v_{wind} =actual wind speed

For Dryden turbulence model, the shaping filters for velocity components are given in the equations below[26]:

$$H_u = \sigma_u \sqrt{\frac{2L_u}{\pi V}} \frac{1}{1 + \frac{L_u}{V} s} \quad (2.13)$$

$$H_v = \sigma_v \sqrt{\frac{L_v}{\pi V}} \frac{1 + \frac{\sqrt{3}L_v}{V} s}{(1 + \frac{L_v}{V} s)^2} \quad (2.14)$$

$$H_w = \sigma_w \sqrt{\frac{L_w}{\pi V}} \frac{1 + \frac{\sqrt{3}L_w}{V} s}{(1 + \frac{L_w}{V} s)^2} \quad (2.15)$$

L_u, L_v, L_w = turbulence scale length

V = Airspeed of the A/C in ft/s

$\sigma_u, \sigma_v, \sigma_w$ = turbulence intensities

Turbulence scale lengths and turbulence intensities are given as function of wind speed at 20ft (6m) and altitude. Below 1000ft (300m), scale lengths and intensities below are defined by empirical formulae given below.

$$L_u = \frac{h}{(0.177 + 0.000823h)^{1.2}} \quad (2.16)$$

$$L_v = \frac{h}{(0.177 + 0.000823h)^{1.2}} \quad (2.17)$$

$$L_w = h \quad (2.18)$$

$$\sigma_u = \frac{\sigma_w}{(0.177 + 0.000823h)^{0.4}} \quad (2.19)$$

$$\sigma_v = \frac{\sigma_w}{(0.177 + 0.000823h)^{0.4}} \quad (2.20)$$

$$\sigma_w = 0.1v_{20} \quad (2.21)$$

v_{20} =wind speed in ft/s at 20ft AGL

h =altitude AGL in ft

Characteristics of the filters are investigated in detail by looking at the Bode plots at an airspeed of 90 ft/s, a wind speed of 30 ft/s and an altitude of 600 ft. As shown in Figure 2.10, the filters are low pass filters. H_u has a cut-off frequency of 2 rad/s, H_v and H_w have cut-off frequencies of 2.5 rad/s.

Wind shear model is added to the code from [26]. In wind shear model, wind speed is assumed to

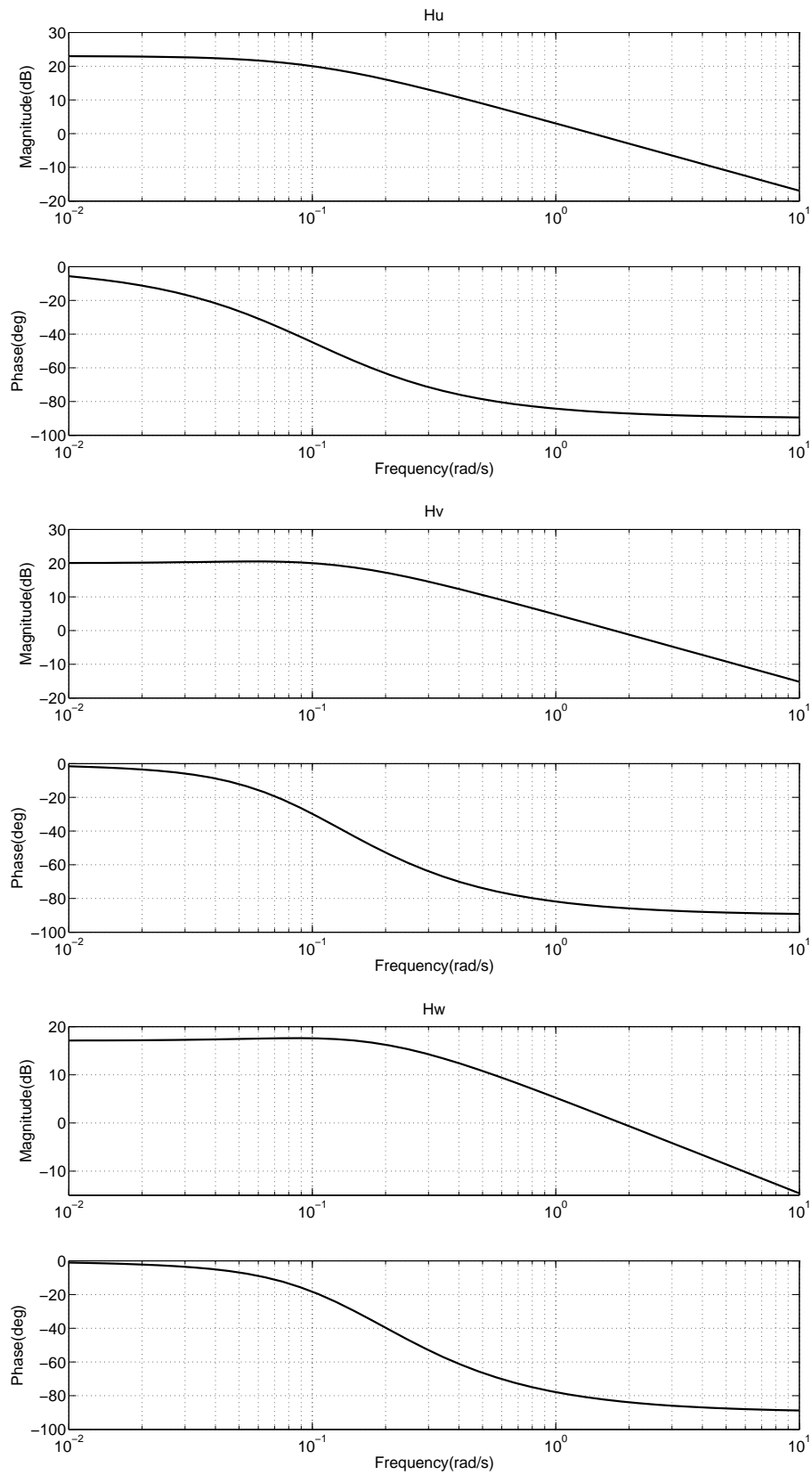


Figure 2.10: Bode plots of velocity shaping filters of Dryden turbulence model

be changing with altitude and calculated w.r.t the wind speed at 20ft above ground level(AGL) from equation 2.22. The equation holds for altitudes less than 1000ft and greater than 3ft.

$$v_{wind} = v_{20} \frac{\ln \frac{h}{0.15}}{\ln \frac{20}{0.15}} \quad (2.22)$$

Variation of wind with altitude under wind shear for $v_{20} = 15$ ft/s is given in Figure 2.11. The wind speed starts decreasing at 300 m, reaches 7 m/s at 50 m and decays to zero at ground level.

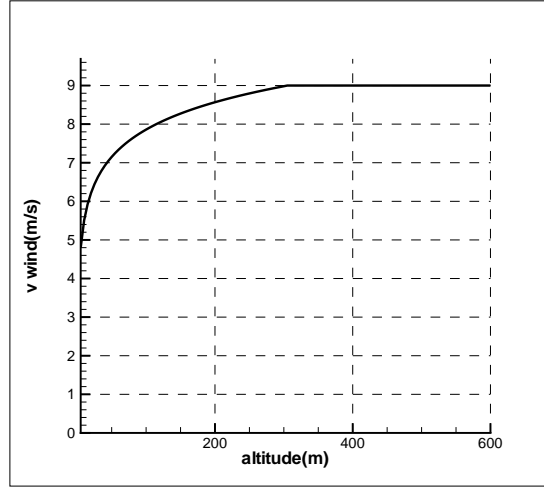


Figure 2.11: The variation of the wind speed with altitude in the wind shear model

2.7 Actuator Model

The control surfaces and the throttle setting of the engine of the METU TUAV are actuated by radio controlled (RC) servos. The rate at which the servos change position and their maximum deflections are limited. Servos are modeled as a first order type system:

$$G_{act} = \frac{T}{s + T} \quad (2.23)$$

T is selected as 15 rad/s for the elevator, ailerons, rudders and the flaps. The dynamics of the engine is added into the engine servo model. Therefore, although servos used for the throttle and other control surfaces are the same, T is selected as 0.5 rad/s for the engine servo. In addition, the elevator deflection is limited to ± 30 deg, flap deflection is limited to 0-45 deg, the engine rpm is limited to 0-7000 rpm, rudder and aileron deflections are limited to ± 25 deg.

2.8 Landing Gear Model

Main and nose landing gears are modeled as spring- damper systems. Force acting on the landing gears are

$$F_{gear} = -c\dot{x}_c - kx_c \quad (2.24)$$

where c is the damping coefficient and k is the spring coefficient of the landing gears. c and k are initially approximated based on similar landing gears. x_c is the compression length and \dot{x}_c is the compression rate of the landing gears.

Detailed experimental tests are required to determine the actual values of c and k for each landing gear. c and k are fine tuned by trial and error observing the reactions of the landing gear in simulations. Damping and spring coefficients of main and nose landing gears are shown in Table 2.6.

x_c is obtained by calculating the distance between the ground and the tires in the z-body frame. \dot{x}_c is the velocity of the tires in the z-body axis direction. The velocities of the landing gears in the body frame are found from;

$$\vec{V}_{gear} = \vec{V}_{aircraft} + \vec{\omega} \times \vec{r}_{gear} \quad (2.25)$$

\vec{r}_{gear} is the position vector of the gears w.r.t the cg in the body axis(equation 2.26) and $\vec{\omega}$ contains the body angular rates. \vec{r}_{gear} is updated throughout the flight. The values of \vec{r}_{gear} at $x_{cg} = 0.3MAC$ are given in Table 2.7.

$$\vec{r}_{gear} = x_{gear}\vec{i} + y_{gear}\vec{j} + z_{gear}\vec{k} \quad (2.26)$$

$$\vec{\omega} = P\vec{i} + Q\vec{j} + R\vec{k} \quad (2.27)$$

Combining equation 2.25 with 2.26 and 2.27;

$$U_{gear} = U + qz_{gear} - ry_{gear} \quad (2.28)$$

$$V_{gear} = V - pz_{gear} + rx_{gear} \quad (2.29)$$

$$W_{gear} = W + py_{gear} - qx_{gear} \quad (2.30)$$

Table 2.6: Damping and spring coefficients of the landing gears

	Damping coefficient (kg/s ²)	Spring coefficient (kg/ms ²)
Main gears	3640	7300
Nose gear	2700	5450

Table 2.7: Position of the wheels w.r.t the cg in the body axis($x_{cg} = 0.3MAC$)

	x_{gear} (m)	y_{gear} (m)	z_{gear} (m)
Left wheel	-0.168	-0.425	0.5
Right wheel	-0.168	0.425	0.5
Nose wheel	0.99	0	0.5

2.9 Ground Reaction Modeling

Interaction between the runway and the UAV is modeled for the touchdown and taxi phases of the A/C. Besides the aerodynamic and propulsive forces and moments the ground reactions heavily influence the landing dynamics of the A/C. The tire fixed axis system is introduced to calculate the ground reactions. This is a coordinate frame attached at the furthest location from the airframe on each landing wheel, called tire axis system. The XY plane of the tire axis is parallel to the ground, with x-axis parallel to the rolling direction of tire, y-axis normal to the rolling direction and the z- axis pointing downwards. The coordinate system is shown in Figure 2.12. The methodology followed to calculate the ground forces and moments is;

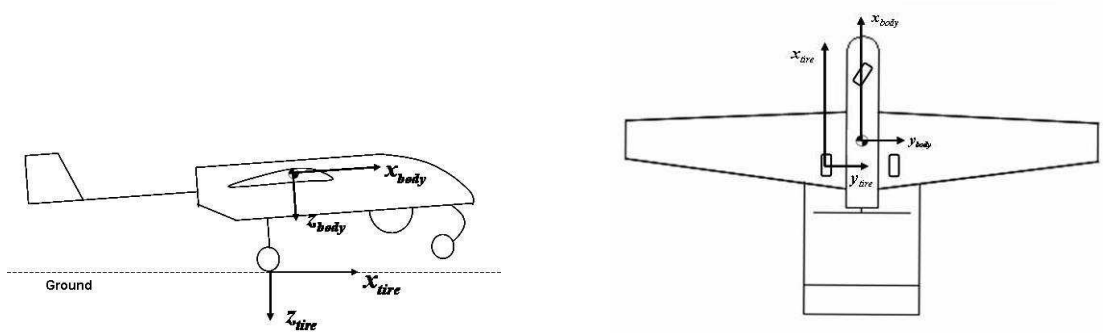


Figure 2.12: Orientation of tire frame

1. The height between ground and each landing gear is calculated in every time step.
2. When the height is less than zero, the force acting on landing gear is calculated from equation 2.24.
3. Then the ground reactions are found. The ground reactions consist of normal, traction

and side forces. The normal forces are found from the landing gear model as follows:

$$N = \frac{-kx_c - c\dot{x}_c}{\cos \theta \cos \phi} \quad (2.31)$$

The traction and side forces are written as a function of friction coefficients and normal forces and they are always opposite to the direction of movement.

$$F_{fx} = \mu_x |N| \frac{U_{gear}}{|U_{gear}|} \quad (2.32)$$

$$F_{fy} = \mu_y |N| \frac{V_{gear}}{|V_{gear}|} \quad (2.33)$$

The value of μ_x depends on the brake input and runway surface. μ_y is dependent to the skid angle. μ_y changes proportionally with skid angle for values less than 10 degrees and remains constant for larger values.(Figure 2.13)[11]

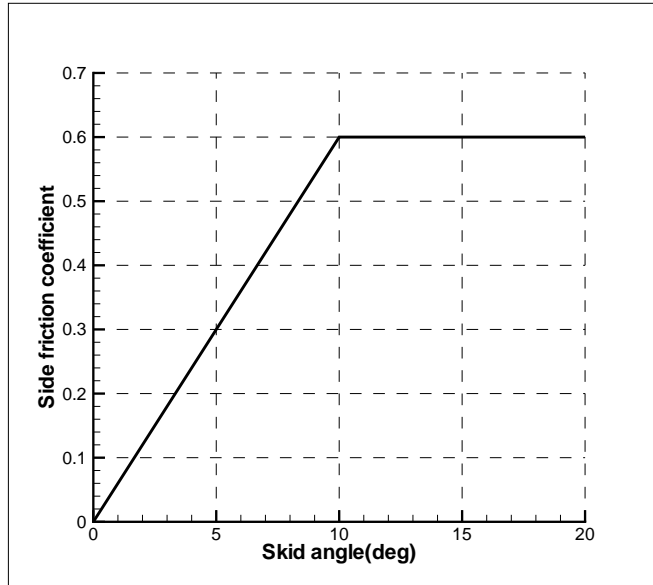


Figure 2.13: Variation of μ_y with η

The direction of the friction forces are shown in Figure 2.14

The friction forces are aligned w.r.t the tire axis. So, the direction of the forces acting on the nose wheel change as it rotates. Friction forces on nose wheel are transformed by rotating the z-tire axis by the steering angle, γ_{nose} . The transformation is shown below;

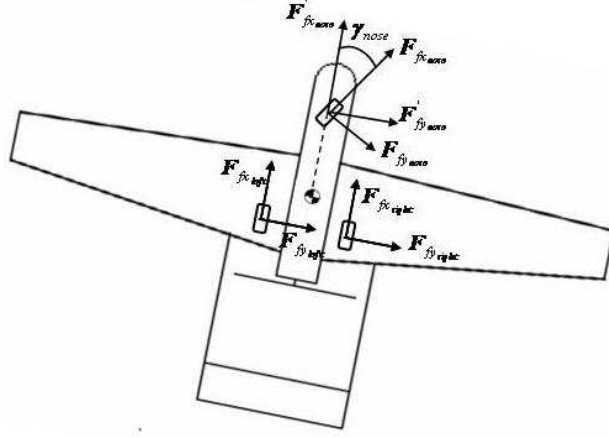


Figure 2.14: Friction forces acting on the UAV

$$\begin{Bmatrix} F'_{fx} \\ F'_{fy} \end{Bmatrix} = \begin{bmatrix} \cos \gamma_{nose} & -\sin \gamma_{nose} \\ \sin \gamma_{nose} & \cos \gamma_{nose} \end{bmatrix} \begin{Bmatrix} F_{fx} \\ F_{fy} \end{Bmatrix}$$

4. The ground reactions are transformed from the tire axis to the body axis. The transformation matrix is found by rotations around the y-axis by pitch angle, θ , and the x-axis by roll angle, ϕ , respectively. The final system of equations are;

$$\begin{Bmatrix} F_{Gx} \\ F_{Gy} \\ F_{Gz} \end{Bmatrix} = \begin{bmatrix} \cos \theta & 0 & -\sin \theta \\ \sin \theta \sin \phi & \cos \phi & \cos \theta \sin \phi \\ \sin \theta \cos \phi & -\sin \phi & \cos \theta \cos \phi \end{bmatrix} \begin{Bmatrix} F_{fx} \\ F_{fy} \\ N \end{Bmatrix}$$

5. Forces are carried to the cg. Moments created around the cg are found.

2.10 Reference Frames, Coordinate Systems and Transformations

Four axis systems are used in the model.

The inertial reference frame is the non-accelerating, non-rotating frame. As the earth is assumed to be flat and non-rotating the inertial frame is usually assumed to be fixed to the ground. It is used for the calculation of the position (X,Y,Z).

The navigation frame also known as north-east-down frame is a non-rotating frame attached to the aircraft with x-axis directed north, y-axis directed east and z-axis directed downwards.

The direction of the gravity vector coincides with the z-axis of this frame.

The equations of motion are written in the frame attached to the aircraft and rotating with the aircraft, the so-called body frame. The aircraft velocities(U,V,W) and the angular rates(p,q,r) are defined in this axis.

The orientation of the aircraft is described by three consecutive rotations from the navigation frame to the body frame. The angular rotations are called Euler angles(ϕ,θ,ψ). The transformation matrix between the navigation axis and the body axis is found by rotating the system first around the z-axis by ψ , then a rotation around the y-axis by θ and finally around x-axis by ϕ , respectively[12]. The resultant matrix is:

$$\begin{pmatrix} x_b \\ y_b \\ z_b \end{pmatrix} = \begin{bmatrix} \cos\theta\cos\psi & \cos\theta\sin\psi & -\sin\theta \\ -\cos\phi\sin\psi + \sin\phi\sin\theta\cos\psi & \cos\phi\cos\psi + \sin\phi\sin\theta\sin\psi & \sin\phi\cos\theta \\ \sin\phi\sin\psi + \cos\phi\sin\theta\cos\psi & -\sin\phi\cos\psi + \cos\phi\sin\theta\sin\psi & \cos\phi\cos\theta \end{bmatrix} \begin{pmatrix} x_n \\ y_n \\ z_n \end{pmatrix}$$

Finally, the aerodynamic forces are defined w.r.t the wind axis system. The wind x-axis is always parallel to the freestream velocity. The wind axis is rotated around the z-axis by $-\beta$, then around the y-axis by α to coincide with the body axis. The resultant transformation matrix is:

$$\begin{pmatrix} x_b \\ y_b \\ z_b \end{pmatrix} = \begin{bmatrix} \cos\alpha\cos\beta & -\cos\alpha\sin\beta & -\sin\alpha \\ \sin\beta & \cos\beta & 0 \\ \sin\alpha\sin\beta & -\sin\alpha\cos\beta & \cos\alpha \end{bmatrix} \begin{pmatrix} x_w \\ y_w \\ z_w \end{pmatrix}$$

The mathematical representation of the angle of attack and the sideslip angles are:

$$\alpha = \tan^{-1} \frac{W}{U} \quad (2.34)$$

$$\beta = \sin^{-1} \frac{V}{\sqrt{U^2 + V^2 + W^2}} \quad (2.35)$$

2.11 6-DOF Equations of Motion

The non-linear equations of motion are written for the 6-DOF simulation. Equations are written in the A/C body axis. The A/C is assumed to be rigid. The XZ plane is the plane of symmetry, so $I_{xy} = I_{yz} = 0$. Using the assumptions above, the equations of motion for the fixed wing aircraft is [12]:

$$\dot{U} = \frac{-mg \sin\theta + F_{Ax} + F_{Tx} + F_{Gx} - m(-Vr + Wq)}{m} \quad (2.36)$$

$$\dot{V} = \frac{mg \sin \phi \cos \theta + F_{Ay} + F_{Ty} + F_{Gy} - m(Ur - Wp)}{m} \quad (2.37)$$

$$\dot{W} = \frac{mg \cos \phi \cos \theta + F_{Az} + F_{Tz} + F_{Gz} - m(-Uq + Vp)}{m} \quad (2.38)$$

$$\begin{aligned} \dot{p} = & [L_A + L_T + L_G + I_{xz}pq - (I_{zz} - I_{yy})rq] \left[\frac{I_{zz}}{I_{xx}I_{zz} - I_{xz}^2} \right] \\ & + [N_A + N_T + N_G - (I_{yy} - I_{xx})pq - I_{xz}qr] \left[\frac{I_{xz}}{I_{xx}I_{zz} - I_{xz}^2} \right] \end{aligned} \quad (2.39)$$

$$\dot{q} = \frac{M_A + M_T + M_G - (I_{xx} - I_{zz})pr - I_{xz}(p^2 - r^2)}{I_{yy}} \quad (2.40)$$

$$\begin{aligned} \dot{r} = & [L_A + L_T + L_G + I_{xz}pq - (I_{zz} - I_{yy})rq] \left[\frac{I_{xz}}{I_{xx}I_{zz} - I_{xz}^2} \right] \\ & + [N_A + N_T + N_G - (I_{yy} - I_{xx})pq - I_{xz}qr] \left[\frac{I_{xx}}{I_{xx}I_{zz} - I_{xz}^2} \right] \end{aligned} \quad (2.41)$$

The Euler angles are found using the following equations:

$$\dot{\phi} = p + q \sin \phi \tan \theta + r \cos \phi \tan \theta \quad (2.42)$$

$$\dot{\theta} = q \cos \phi - r \sin \phi \quad (2.43)$$

$$\dot{\psi} = (q \sin \phi + r \cos \phi) \sec \theta \quad (2.44)$$

2.12 Linear Equations of Motion and Analysis

The equations of motion are linearized around the trim values to investigate the stability characteristics of the A/C. This information is also used in the controller design. Detailed information about the calculation of the dimensional aerodynamic derivatives and the linearization procedure is given in [12].

Trim values of the UAV is found as $U_{cr} = 39m/s$, $W_{cr} = 1.64m/s$, $\theta_{cr} = 2.45deg$ and $n_{cr} = 4880rpm$ at $x_{cg} = 0.3MAC$ and $Z=3000m$ above sea level. Longitudinal and lateral dynamics have small effect on each other, so, they are decoupled.

2.12.1 Longitudinal Dynamics

The state space representation of the longitudinal EOM is:

$$\begin{aligned}
\begin{pmatrix} \dot{u} \\ \dot{\alpha} \\ \dot{q} \\ \dot{\Delta\theta} \end{pmatrix} &= \begin{bmatrix} X_u + X_{Tu} & X_\alpha & 0 & -g \cos \theta_{cr} \\ \frac{Z_u}{U_{cr} - Z_{\dot{\alpha}}} & \frac{Z_\alpha}{U_{cr} - Z_{\dot{\alpha}}} & \frac{Z_q + U_1}{U_{cr} - Z_{\dot{\alpha}}} & \frac{-g \sin \theta_{cr}}{U_{cr} - Z_{\dot{\alpha}}} \\ M_u + \frac{M_{\dot{\alpha}} Z_u}{U_{cr} - Z_{\dot{\alpha}}} & M_\alpha + \frac{M_{\dot{\alpha}} Z_\alpha}{U_{cr} - Z_{\dot{\alpha}}} & M_q + \frac{M_{\dot{\alpha}} (Z_q + U_{cr})}{U_{cr} - Z_{\dot{\alpha}}} & -\frac{M_{\dot{\alpha}} g \sin \theta_{cr}}{U_{cr} - Z_{\dot{\alpha}}} \\ 0 & 0 & 1 & 0 \end{bmatrix} \begin{pmatrix} u \\ \alpha \\ q \\ \Delta\theta \end{pmatrix} \\
+ \begin{bmatrix} X_{\delta_e} & X_{Tn} \\ \frac{Z_{\delta_e}}{U_{cr} - Z_{\dot{\alpha}}} & 0 \\ M_{\delta_e} + \frac{M_{\dot{\alpha}} Z_{\delta_e}}{U_{cr} - Z_{\dot{\alpha}}} & 0 \\ 0 & 0 \end{bmatrix} & \begin{pmatrix} \delta_e \\ \Delta n \end{pmatrix}
\end{aligned}$$

The dimensional thrust derivatives, X_{Tn} and X_{Tu} are found by taking derivatives of the equation 2.7 w.r.t n and u :

$$X_{Tu} = \frac{\partial C_t}{\partial u} \rho n^2 D^4 \quad (2.45)$$

$$X_{Tn} = \left(\frac{\partial C_t}{\partial n} n + 2C_t \right) \rho n D^4 \quad (2.46)$$

The longitudinal system matrix (A_{long}) and input matrix (B_{long}) at the trim condition is:

$$A_{long} = \begin{bmatrix} -0.085 & 4.603 & 0 & -9.798 \\ -0.012 & -2.131 & 0.98 & -0.011 \\ 0.009 & -26.397 & -2.955 & 0.008 \\ 0 & 0 & 1 & 0 \end{bmatrix}$$

$$B_{long} = \begin{bmatrix} 0 & 0.038 \\ -0.144 & 0 \\ -28.126 & 0 \\ 0 & 0 \end{bmatrix}$$

The longitudinal motion is described by two different oscillatory modes, namely the short period mode and the phugoid mode.

The short period mode involves the variation of the angle of attack and the pitch angle at constant speed. This mode is heavily damped. Oscillations die out quickly.

The second mode is the phugoid mode, where most of the variation is in the A/C speed mostly at constant angle of attack. This mode is lightly damped and can be observed easily.

Eigenvalues of the A_{long} matrix contain information about the longitudinal modes of the system. Longitudinal mode characteristics for this aircraft are given in Table 2.8. Both modes are stable since the real parts of their roots are negative. The short period mode has a higher damping ratio. As a result, it has a shorter time to half and period which are 0.27s and 1.24s, respectively. Roots of the phugoid mode are closer to the origin. It has a time to half value of 21s and period of 20.4s.

Table 2.8: Longitudinal mode characteristics

	Root Location	Natural Frequency ω_n (rad/s)	Damping Ratio ξ	Time to Half Amplitude(s)	Period (s)
Short Period	$-2.552 \pm 5.069i$	5.68	0.45	0.272	1.239
Phugoid	$-0.033 \pm 0.312i$	0.31	0.11	21	20.39

2.12.2 Lateral Dynamics

The state space representation of the lateral dynamics is;

$$\begin{pmatrix} \dot{\beta} \\ \dot{p} \\ \dot{r} \\ \dot{\phi} \\ \dot{\psi} \end{pmatrix} = \begin{bmatrix} \frac{Y_{\beta}}{U_{cr}} & \frac{Y_p}{U_{cr}} & \frac{Y_r}{U_{cr}} - 1 & \frac{g \cos \theta_{cr}}{U_{cr}} & 0 \\ \frac{L_{\beta} + A_1 N_{\beta}}{1 - A_1 B_1} & \frac{L_p + A_1 N_p}{1 - A_1 B_1} & \frac{L_r + A_1 N_r}{1 - A_1 B_1} & 0 & 0 \\ \frac{N_{\beta} + B_1 L_{\beta}}{1 - A_1 B_1} & \frac{N_p + B_1 L_p}{1 - A_1 B_1} & \frac{N_r + B_1 L_r}{1 - A_1 B_1} & 0 & 0 \\ 0 & 1 & 0 & 0 & 0 \\ 0 & 0 & 1 & 0 & 0 \end{bmatrix} \begin{pmatrix} \beta \\ p \\ r \\ \phi \\ \psi \end{pmatrix} + \begin{bmatrix} \frac{Y_{\delta_a}}{U_{cr}} & \frac{Y_{\delta_r}}{U_{cr}} \\ \frac{L_{\delta_a} + A_1 N_{\delta_a}}{1 - A_1 B_1} & \frac{L_{\delta_r} + A_1 N_{\delta_r}}{1 - A_1 B_1} \\ \frac{N_{\delta_a} + B_1 L_{\delta_a}}{1 - A_1 B_1} & \frac{N_{\delta_r} + B_1 L_{\delta_r}}{1 - A_1 B_1} \\ 0 & 0 \\ 0 & 0 \end{bmatrix} \begin{pmatrix} \delta_a \\ \delta_r \end{pmatrix}$$

where $A_1 = I_{xz}/I_{xx}$ and $B_1 = I_{xz}/I_{zz}$.

Lateral system matrix(A_{lat}) and input matrix(B_{lat}) at the trim condition is;

$$A_{lat} = \begin{bmatrix} -0.105 & 0. & -0.997 & -0.251 & 0 \\ -5.995 & -8.447 & 1.606 & 0 & 0 \\ 5.378 & 0.518 & -0.515 & 0.008 & 0 \\ 0 & 1 & 0 & 0 & 0 \\ 0 & 0 & 1 & 0 & 0 \end{bmatrix}$$

$$B_{lat} = \begin{bmatrix} 0 & 0.115 \\ 140.113 & 8.076 \\ -16.739 & -11.967 \\ 0 & 0 \\ 0 & 0 \end{bmatrix}$$

The lateral modes are the roll mode, spiral mode and the Dutch-roll mode.

The roll mode is dominant over the roll angle.

The spiral mode consists mainly of yawing at almost zero sideslip with some rolling. During the analysis of the METU TUAV, it was found that the dihedral angle is quite influential for the stability of this mode. However, this mode turns out to be slow and therefore a control law can easily be employed to assure closed loop stability.

The Dutch-roll mode is the oscillatory mode of the lateral dynamics. This mode is a combination of roll, yaw and sideslip.

Eigenvalues of the A_{lat} matrix contain the necessary information about the lateral modes of the system. The lateral mode characteristics are shown in Tables 2.9 and 2.10. The roll and Dutch-roll modes are stable. The spiral mode is unstable, but its time to double amplitude is more than 22 seconds which is rather slow as mentioned before.

Table 2.9: Dutch roll mode characteristics

	Root Location	Natural Frequency ω_n (rad/s)	Damping Ratio ξ	Time to Half Amplitude(s)	Period (s)
Dutch Roll	$-0.287 \pm 2.264i$	2.282	0.126	2.415	2.776

Table 2.10: Roll and spiral mode characteristics

	Root Location	Time Constant (s)	Time to Half Amplitude(s)
Roll	-8.524	0.117	0.081
Spiral	0.031	32.2	22.355

2.13 Open Loop Simulation

The response of the body x and z-velocities, body pitch rate and pitch angle to a 5 degree elevator step input for five seconds from t=10 to t=15 are given in Figure 2.15. The system reaches a longitudinal trim condition in about 150 s.

The response of the body y-velocity, body roll rate, body yaw rate, roll angle and yaw angle to a 1 degree aileron step input for five seconds from t=10 to t=15 are given Figure 2.16. Due to the unstable spiral mode the yaw angle keeps increasing, which results in a circular motion with a nearly constant roll angle and zero side velocity.

To take a closer look at the unstable mode a smaller disturbance is given to the system. This time the response of the system to a 2 m/s initial side velocity is investigated. The 3-D position plot of the aircraft caused by this disturbance is given in Figure 2.17. The instability in the spiral mode effects the system slowly and does not constitute a critical controllability problem for the UAV. The pilot or the autopilot can easily make necessary adjustments before the UAV begins its circular motion.

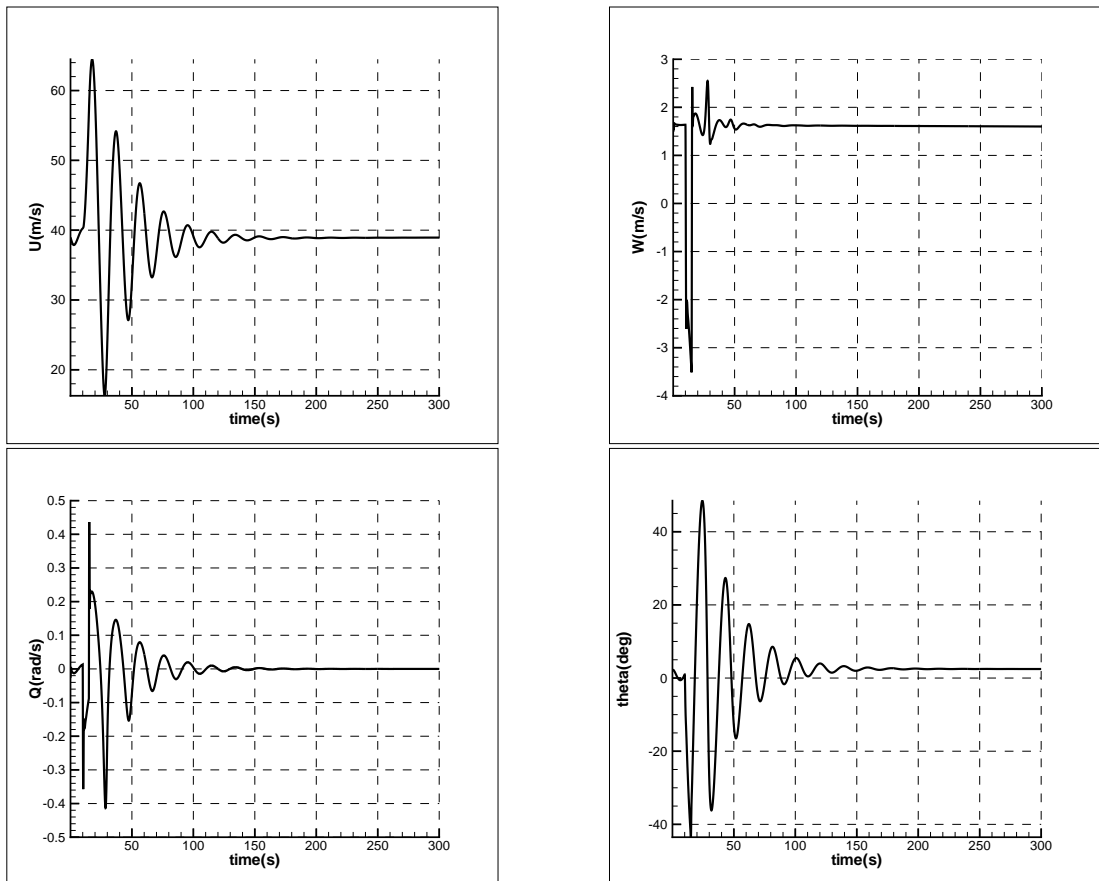


Figure 2.15: Response of the system to elevator input

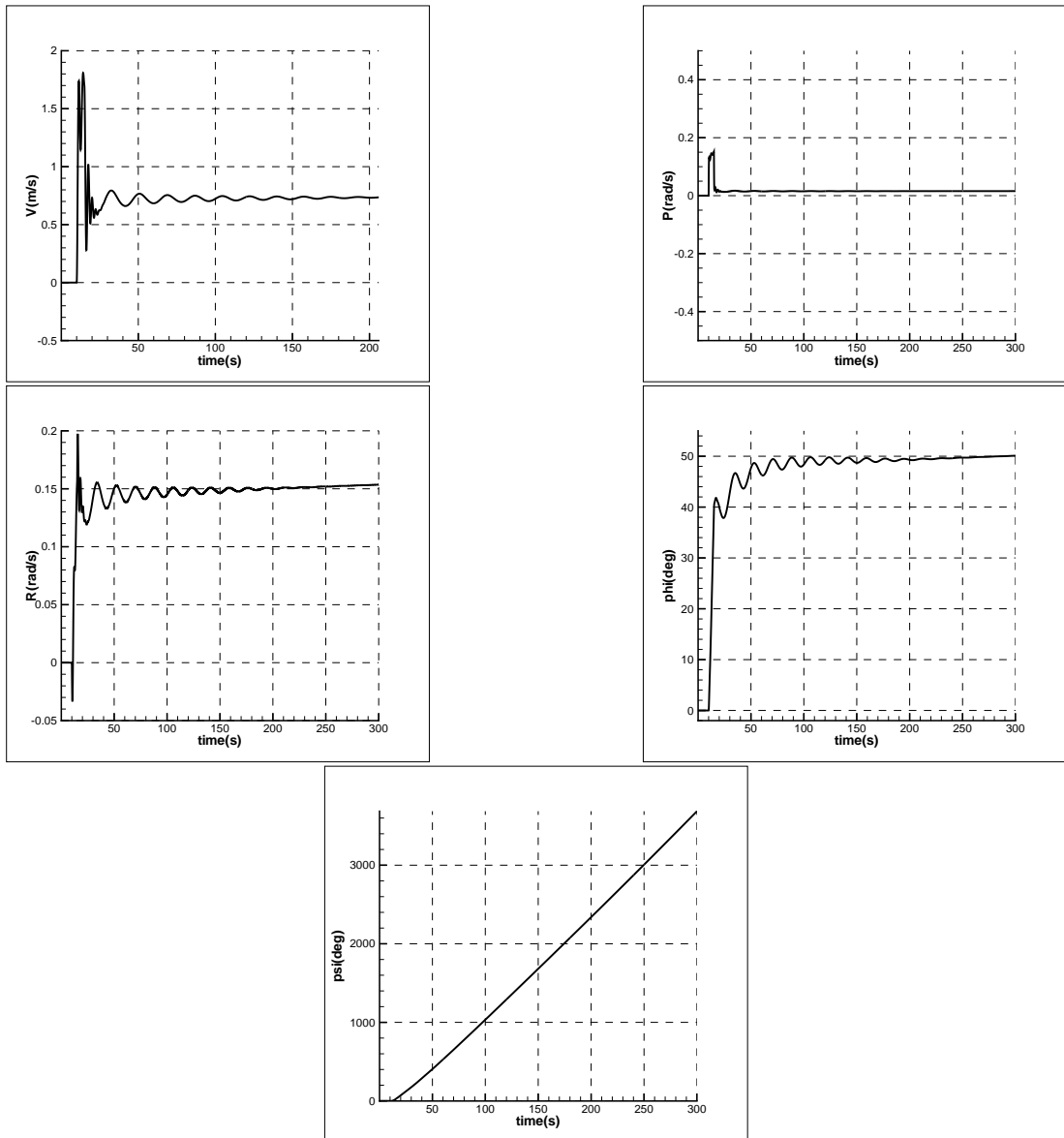


Figure 2.16: Response of the system to aileron input

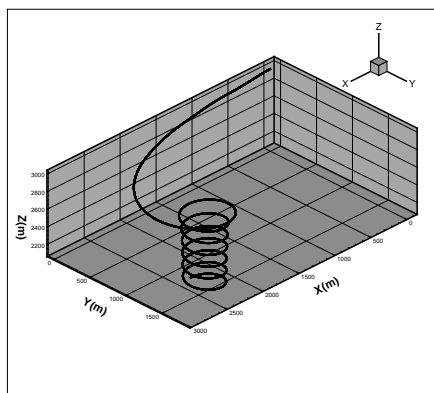


Figure 2.17: Position change of the UAV in time due to 2m/s initial side velocity disturbance

CHAPTER 3

LANDING TRAJECTORY GENERATION

This chapter describes the generation of the landing trajectory and the required maneuvers of the UAV for a safe landing.

3.1 Commanded Trajectory Generation

A conceptual plot of the landing trajectory for the METU TUAV is shown in Figure 3.1. It is assumed that the aircraft first descends to an altitude of 100m with a circuit maneuver (descending with a circular trajectory). Aircraft flies at this altitude for a while, it aligns its heading with the runway centerline and decreases its velocity. Then, A/C begins its landing maneuvers and descends towards the runway with a constant flight path angle. It enters a flare phase very close to touchdown in order to reduce the impact on the landing gears. After touchdown the A/C follows the runway centerline until it stops.

3.1.1 Landing Phases

3.1.1.1 Descent Phase

Descent phase comprise the interval which A/C descends from 100m to flare altitude. The glide slope and airspeed is constant during this phase. The aircraft speed and the flight path

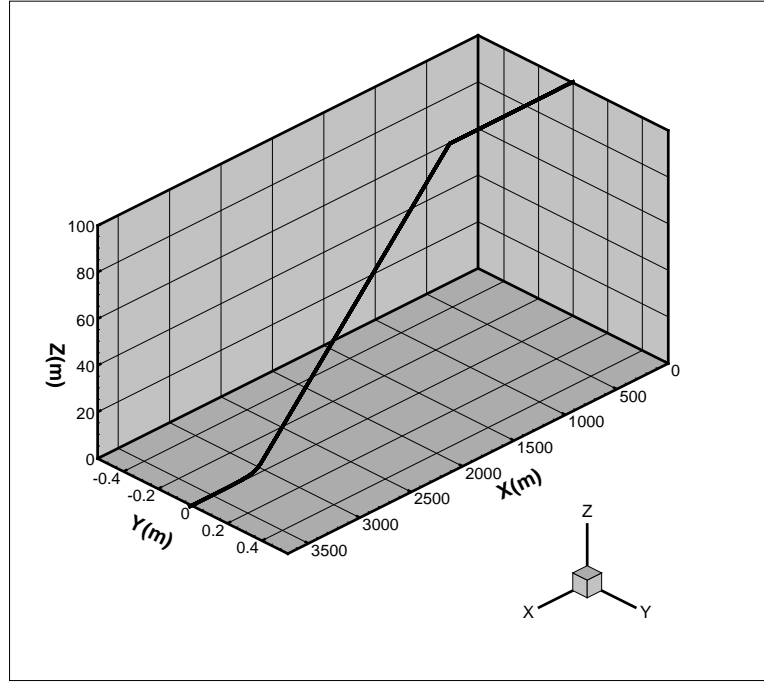


Figure 3.1: Conceptual landing trajectory

angle, γ , are two important parameters in determining the trajectory for the descent phase. A low velocity is preferred for a short landing distance. In addition, a high flight path angle is desired in order to decrease the approach and the landing time. However, unlike cruise and climb, it is not always possible to control the velocity using only the throttle setting, since the aircraft velocity is more sensitive to changes in pitch angle at descent. Lower trim velocities can be obtained for high γ values if forward velocity is controlled by the elevator. However the longitudinal trajectory control is the first priority during landing and can not be controlled precisely by using the throttle only due to the slow dynamics of the propulsion system.

Several simulations were performed for different γ and forward velocities to find a suitable landing trajectory for the UAV. The results are shown in Figure 3.2.

Note that, the minimum forward velocity for $\gamma = 3.5$ degrees and less is 25m/s. However, the minimum forward velocity increases drastically at 4 degrees and keeps increasing afterwards. This can be explained by the lack of control authority of the propulsion system during descent with high angles. Considering the stall speed of 23 m/s, the landing velocity is chosen as 28 m/s. The highest possible flight path angle is 3.5 degrees for that selected velocity.

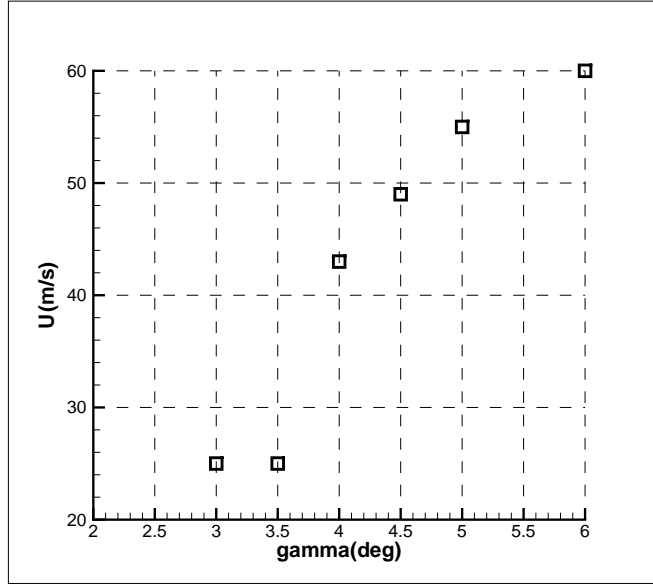


Figure 3.2: Minimum landing velocities for different γ

3.1.1.2 Flare Phase

The structural loading on the landing gears should be tolerably small at touchdown. This is achieved by reducing the descent rate at the flare phase. In [17], the flare trajectory is determined based on forward velocity, flight path angle, flare initiation altitude and flare time. Here, the velocity is constant throughout the landing phase. The flare initiation altitude is assumed to be not more than 10m and the flare time is not to be more than 15s. The trajectory parameters are selected by taking these limitations into account. The flare trajectory is modeled using the following exponential equation:

$$h_{des} = 4.58e^{-t/2.67} \quad (3.1)$$

The flare maneuver is programmed to start at 4.6 m and is designed to last for nearly 10 seconds. The flare maneuver is shown in Figure 3.3. The desired descent rate is given by equation 3.2. The descent rate is proportional to the altitude in this equation. It goes to zero as the altitude goes to zero.

$$\dot{h}_{des} = -\frac{1}{2.67}h_{des} \quad (3.2)$$

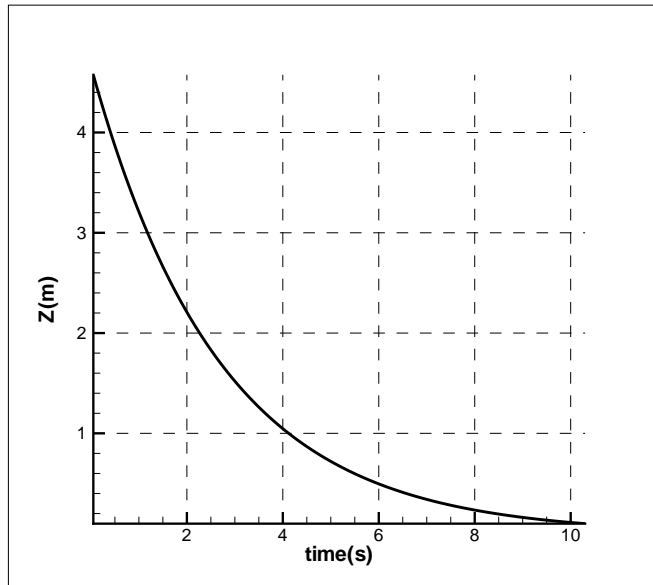


Figure 3.3: Flare maneuver

3.1.1.3 Taxi Phase

The taxi phase is the period after touchdown. Aerodynamic control surfaces, in particular the rudder, and the nose landing gear is used to control the heading in this phase. The throttle should be in its idle position to further slow down. The control of the taxi phase is considered to be out of the scope of this thesis.

3.2 Landing Maneuvers

Although the trajectory and velocity control is sufficient in most of the landing phase, there are some additional considerations:

In the flare phase the autopilot commands a fast pitch up maneuver to minimize altitude error which results in descent rate reduction. Additional lift created by flap deflection will help the A/C at this point. The effect of the flaps on the longitudinal trajectory control is discussed in more detailed in section 4.3.2.

Another problem is the crab angle(the angle between an aircraft's course and its heading required to maintain that course against the wind [25]) reduction before touchdown. The aircraft has to approach to the runway with large crab angles under strong side winds. These angles will be larger than the angles usually encountered during cruise because of the low approach

velocity. If the crab angle is not corrected before touchdown, the A/C will have a large lateral deviation and probably will excur the runway. If it is reduced too early then the A/C can not keep its lateral track and pass the runway. In addition, the roll angle is also limited at touch-down to protect the wings and prevent unbalanced load distribution on landing gears. After some simulations it is decided that both decrab and deroll maneuvers should be commanded at 0.5m prior to touchdown.

The automatic landing procedure is determined as shown in Figure 3.4. The steps are as follows:

- Approach the runway with a constant flight path angle and velocity.
- Keep lateral position error at minimum.
- Deflect flaps when flare initiates.
- Pitch up moment is created increasing pitch angle and reducing descent rate.
- Reduce the crab angle and level the wings when the UAV is close to the runway.

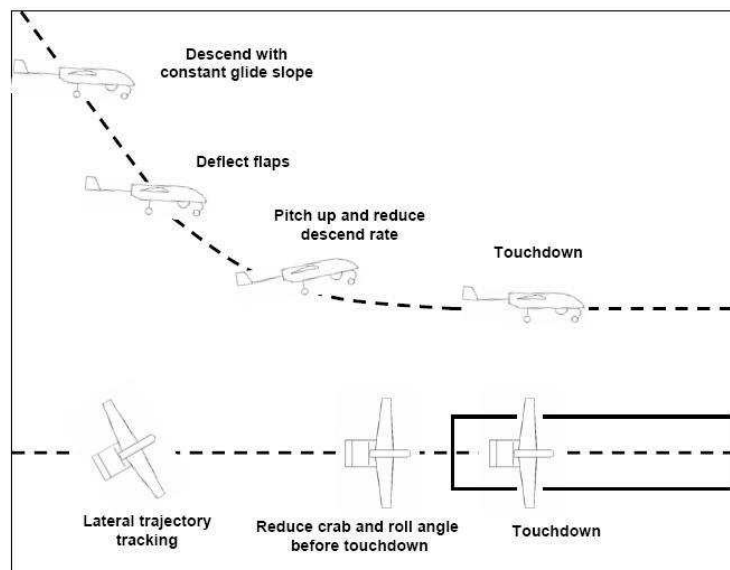


Figure 3.4: Landing Procedure

CHAPTER 4

CONTROLLER DESIGN

In this chapter, the controller development for the landing phase of the METU TUAV is described.

The controller development is completed in two steps: Firstly, an inner loop controller is designed to control the fast angular dynamics of the aircraft. Therefore, the Euler angles and the angular rates are controlled in this part. The control surface deflections are obtained by inverting the moment equations. The outer loop is written to control the aircraft velocity and positions. Different trajectory following algorithms are investigated for a tight path tracking.

4.1 Onboard Sensors

The following onboard sensors are assumed to be present when designing the control system:

- One Inertial Navigation System (INS) with accelerometers providing body accelerations in 3 axis and rate gyros providing body angular rates in 3 axis.
- One Global Positioning Sensor (GPS)(preferably a DGPS) which provides position of the aircraft.
- One differential pressure sensor providing differential for airspeed measurement.
- One static pressure sensor providing barometric pressure for barometric altitude measure-

ment.

- One ultrasonic or laser altimeter providing accurate altitude information close to the ground.
- Three Weight on Wheel (WOW) sensors showing if right, left and nose landing gears have touched the ground or not.

Roll, pitch and yaw attitudes are calculated by integrating body angular rates. However, error grows in integration process and diverges after a while. The navigation system fuses INS and GPS data to correct attitude measurements. A magnetometer can be added to the system to increase accuracy in heading measurement. Ground velocities are obtained differentiating position data.

4.2 Inner Loop Controller Design

4.2.1 Model Inversion Control

In the inner loop, an approximate linear model containing the rotational dynamics at a trim condition of the UAV is inverted based on [27].

$$\delta_c = B^{-1}[\dot{\omega} - A_t \nu - A_r \omega] \quad (4.1)$$

In equation 4.1, $\delta_c = [\delta_e \delta_a \delta_r]^T$ are the control surface deflections, $\omega = [q \ p \ r]^T$, are the body angular rates and $\nu = [u \ v \ w]^T$ the body velocities. A_t and A_r define the translational and rotational dynamics. B is the invertible input matrix. Taking the inverse of the linear model derived in chapter 2 the following equations are obtained:

$$\delta_e = \frac{1}{M_{\delta_e} + Z_{\delta_e} H_1} \left[\dot{q}_{des} - [(M_u + Z_u H_1)u + \frac{M_\alpha + Z_\alpha H_1}{U_{cr}} w] - [(M_q + (Z_q + U_{cr}) H_1)q] \right]$$

$$\begin{Bmatrix} \delta_a \\ \delta_r \end{Bmatrix} = \begin{bmatrix} -\frac{(N_r + L_r B_1)(1 - A_1 B_1)}{G_1} & \frac{(L_r + N_r A_1)((1 - A_1 B_1))}{G_1} \\ \frac{(N_a + L_a B_1)(1 - A_1 B_1)}{G_1} & -\frac{(L_a + N_a A_1)((1 - A_1 B_1))}{G_1} \end{bmatrix} \begin{bmatrix} \dot{p}_{des} \\ \dot{r}_{des} \end{bmatrix}$$

$$- \begin{bmatrix} \frac{L_\beta + A_1 N_\beta}{(1 - A_1 B_1) U_{cr}} \\ \frac{N_\beta + B_1 L_\beta}{(1 - A_1 B_1) U_{cr}} \end{bmatrix} \begin{Bmatrix} v \end{Bmatrix} - \begin{bmatrix} \frac{L_p + A_1 N_p}{1 - A_1 B_1} & \frac{L_r + A_1 N_r}{(1 - A_1 B_1)} \\ \frac{N_p + B_1 L_p}{1 - A_1 B_1} & \frac{L_r + A_1 N_r}{1 - A_1 B_1} \end{bmatrix} \begin{Bmatrix} p \\ r \end{Bmatrix}$$

where,

$$H_1 = \frac{M_{\dot{\alpha}}}{U_{cr} - Z_{\dot{\alpha}}} \quad (4.2)$$

$$G_1 = -L_a N_r - N_a A_1 L_r B_1 + N_a L_r + L_a B_1 N_r A_1 \quad (4.3)$$

If desired the angular accelerations can also be commanded to the system. The required control surface deflections can then be found by solving the inverted equations.

4.2.2 Command Filter

Commands filters are low pass filters which shape the command inputs to match the aircraft dynamics. The architecture of the command filter used for the theta command is shown in Figure 4.1. $\ddot{\theta}_c, \dot{\theta}_c, \theta_c$ and $\int \theta_c$ are outputs of the command filter which will be used in the desired angular acceleration, $\ddot{\theta}_{des}$ calculations. The same command filter architecture is used

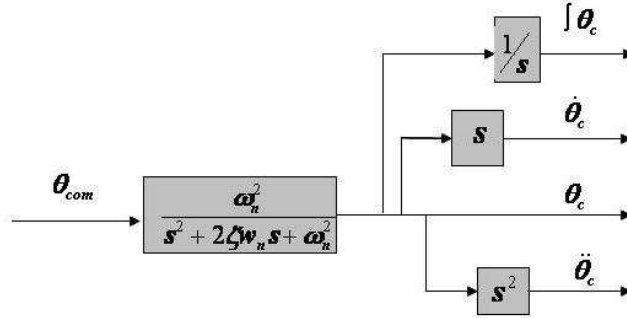


Figure 4.1: Pitch channel command filter

for the ψ and ϕ channels. The values of natural frequency and damping ratio of the command filters are selected such that it matches the aircraft dynamics without slowing down the system or asking for more performance than the aircraft can deliver.(Table 4.1)

Table 4.1: Command filter characteristics

Command Filter	Natural Frequency ω_n (rad/s)	Damping Ratio ξ
θ	9	1
ϕ	12	1
ψ	6	1

4.2.3 Attitude Controller

In terms of individual components the desired angular accelerations are found by the following formulae:

$$\ddot{\theta}_{des} = \ddot{\theta}_c + K_{p\theta}(\theta_c - \theta) + K_{d\theta}(\dot{\theta}_c - \dot{\theta}) + K_{i\theta} \int (\theta_c - \theta) \quad (4.4)$$

$$\ddot{\psi}_{des} = \ddot{\psi}_c + K_{p\psi}(\psi_c - \psi) + K_{d\psi}(\dot{\psi}_c - \dot{\psi}) + K_{i\psi} \int (\psi_c - \psi) \quad (4.5)$$

$$\ddot{\phi}_{des} = \ddot{\phi}_c + K_{p\phi}(\phi_c - \phi) + K_{d\phi}(\dot{\phi}_c - \dot{\phi}) + K_{i\phi} \int (\phi_c - \phi) \quad (4.6)$$

A PID controller is used to obtain desired angular accelerations. A derivative controller is necessary to stabilize the system by eliminating the angular rate errors. The integral term eliminates steady state errors in the autopilot. In addition, the angular acceleration command is fed forward to the system to achieve faster response. The methodology of the $\ddot{\theta}_{des}$ calculations are shown in fig 4.2. The block diagrams for $\ddot{\phi}_{des}$ and $\ddot{\psi}_{des}$ are similar. The gains of the attitude autopilot are given in Table 4.2. Step inputs of $\theta = 10deg$, $\phi = 15deg$ and $\psi = 30deg$ are given

Table 4.2: Inner loop gains

	K_p	K_d	K_i
θ	250	50	10
ϕ	400	150	50
ψ	100	20	10

to observe the response of the system (Figure 4.3). The A/C is able to follow the commanded Euler angles. The transient response analysis of the A/C is shown in Table 4.3.

Table 4.3: Transient characteristics of the inner loop controller

	Maximum overshoot (%)	Settling time (s)
θ	0.5	1.1
ϕ	0.3	0.7
ψ	0.15	1.1

To use the inverted EOM, the angular accelerations have to be transformed from the Euler frame to the body frame. The desired body angular accelerations are calculated from equations

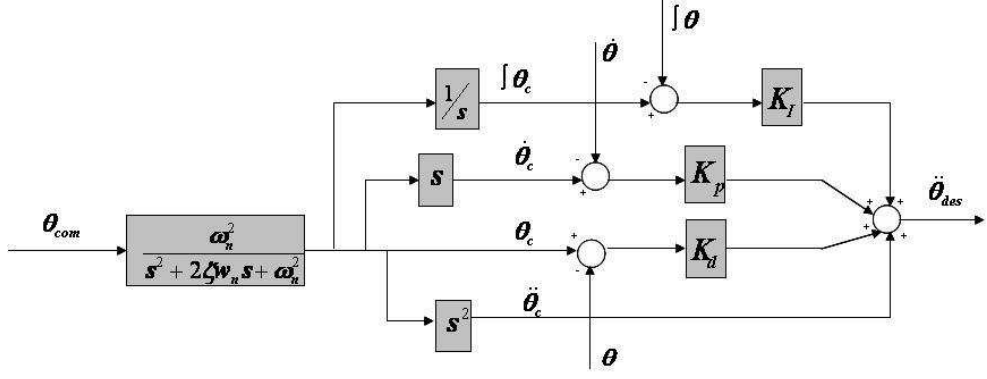


Figure 4.2: Pitch channel autopilot

4.7, 4.8 and 4.9.[27]

$$\dot{p}_{des} = \ddot{\phi}_{des} - \ddot{\psi}_{des} \sin \theta - \dot{\psi} \dot{\theta} \cos \theta \quad (4.7)$$

$$\dot{q}_{des} = \ddot{\theta}_{des} \cos \phi - \dot{\theta} \dot{\phi} \sin \phi + \ddot{\psi}_{des} \sin \phi \cos \theta + \dot{\psi} \dot{\phi} \cos \phi \cos \theta - \dot{\psi} \dot{\theta} \sin \phi \sin \theta \quad (4.8)$$

$$\dot{r}_{des} = -\ddot{\theta}_{des} \sin \phi - \dot{\theta} \dot{\phi} \cos \phi + \ddot{\theta}_{des} \cos \phi \cos \theta - \dot{\psi} \dot{\theta} \cos \phi \sin \theta \quad (4.9)$$

4.3 Longitudinal Outer Loop Controller

A block diagram for the controller in the longitudinal channel is given in figure 4.4.

The forward velocity is controlled by the throttle setting using model inversion. Here it is desired to keep the freestream velocity constant in order to prevent stall which is a critical parameter during landing. The desired ground speed (U_{des}) is obtained by subtracting the wind from the freestream velocity. The altitude is connected to the pitch angle in the inner loop.

4.3.1 Forward Velocity Controller

The forward velocity is connected to the throttle via inverting the linear force equation in the body x-direction. The inverted force equation is:

$$n = \frac{1}{X_n} \left[\dot{u}_{des} - [(X_u + X_{Tu})u + \frac{X_\alpha}{U_1} w - g \cos \theta_1 \Delta \theta] \right]$$

\dot{u}_{des} is the output of the command filter.

A first order command filter is used in generating the desired velocities. The architecture of the filter is shown in figure 4.5. T is selected 0.15 rad/s considering slow dynamics of the engine.

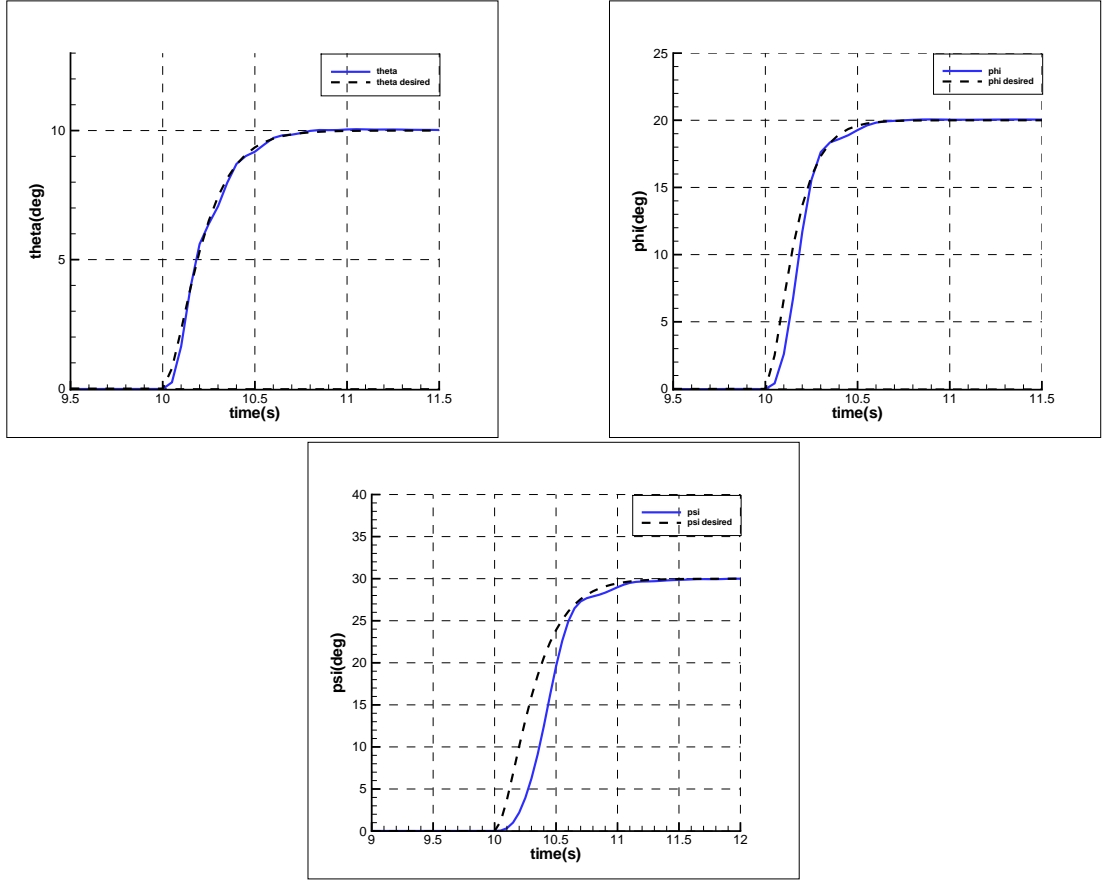


Figure 4.3: Response of the system to step input

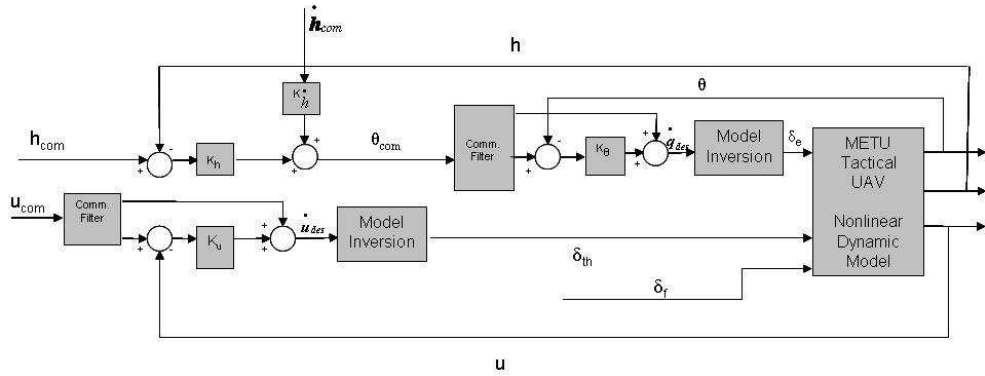


Figure 4.4: Longitudinal autopilot

A PI controller is designed for the velocity control. Similar to the attitude controllers, the commanded forward acceleration is fed forward to the system. The desired acceleration is found from the following equations 4.10

$$\dot{U}_{des} = \dot{U}_c + K_{pu}(U_c - U) + K_{iu} \int (U_c - U) \quad (4.10)$$

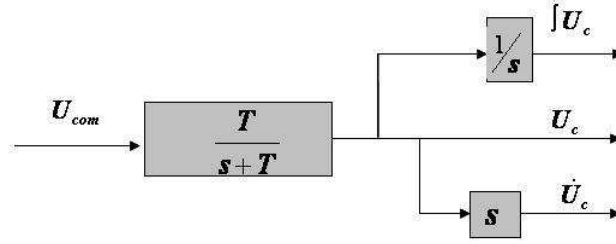


Figure 4.5: Forward velocity command filter

K_{p_u} is 70 and K_{i_u} is 0.5. A 10 m/s velocity increase is commanded to the system to investigate the response of velocity autopilot(Figure 4.6). There is a error between desired and actual velocity which is compensated after 10 seconds. The reason of this error is the saturation of the engine. RPM is limited to a value approximately 6100 which results in loss of control authority on velocity. The error is minimized soon and autopilot is able to increase speed from 40 m/s to 50 m/s in less than 20 seconds.

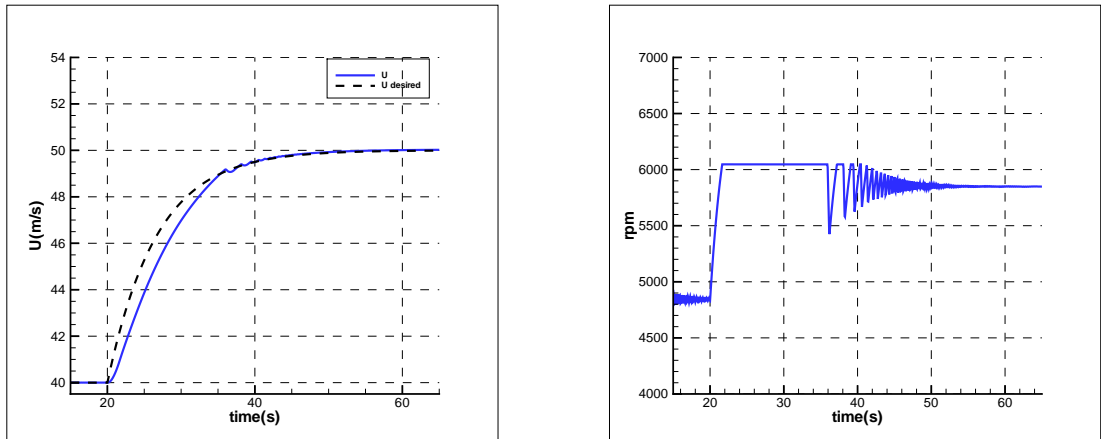


Figure 4.6: Response of the system to velocity input

4.3.2 Altitude Control

The altitude is controlled by issuing the pitch angle command to the inner loops. The PI controller is sufficient for the trajectory following during cruise, descent and climb with constant angle. However, the performance of the controller isn't sufficient for landing. A feed-forward term in the form of a descent rate is used for faster convergence[15]. Desired descent rate is found by:

$$\dot{h}_{com} = U_{des} \sin \gamma_{des} \quad (4.11)$$

U_{des} is the desired forward velocity, which is an input by the pilot and γ_{des} is the desired flight path angle, determined by the properties of the trajectory. Comparisons of controllers with and without the feed forward term are shown in Figures 4.7 and 4.8. The commanded pitch angle is found from equation 4.12.

$$\theta_{com} = K_{ph}(h_{com} - h) + K_{ih} \int (h_{com} - h) + K_h \dot{h}_{com} \quad (4.12)$$

The gain selection for this controller is shown in Table 4.4

Table 4.4: h controller gains

K_{ph}	K_{ih}	K_h
0.1	0.007	0.014

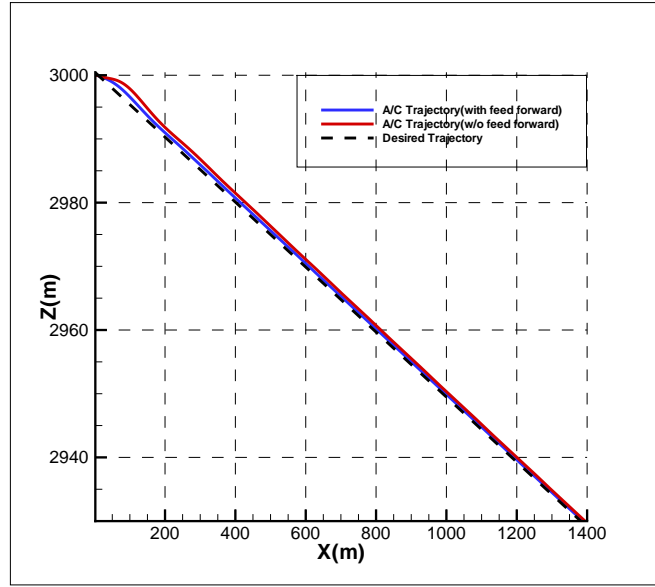


Figure 4.7: Comparison of autopilots with and without feeding \dot{h} forward (trajectory with constant flight angle)

The effect of the flaps on the A/C is a reduction in the descent rate by producing additional lift and drag. Contribution of flaps to the controller is limited in descent phase. Unlike in the descent phase, the descent rate should be minimized in the flare phase just before touchdown. So, flaps are deflected automatically at flare to help the longitudinal controller. The comparison of the flare maneuver with and without flaps deflected are shown in Figure 4.9. The UAV tracks the trajectory more accurately when flaps are deflected by 10 degrees at the beginning of the flare.

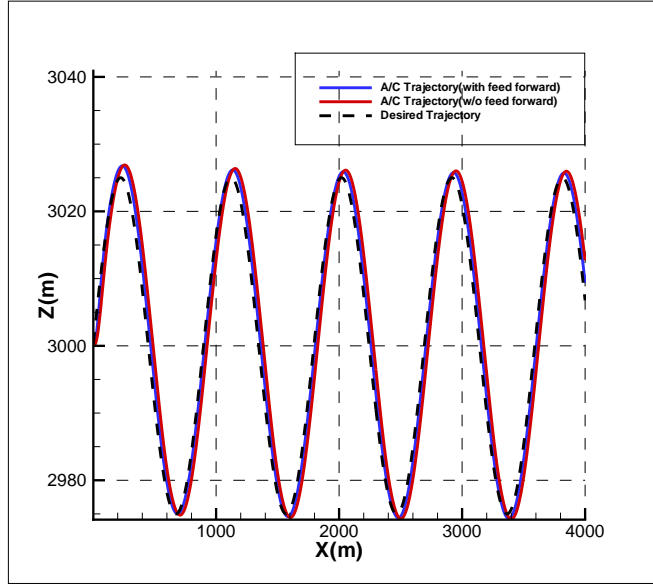


Figure 4.8: Comparison of autopilots with and without feeding \dot{h} forward(sinusoidal trajectory)

4.4 Lateral Outer Loop Controller

4.4.1 Lateral Trajectory Control

The goal of the lateral controller is to minimize the cross track error, which is the lateral error between the commanded trajectory and the aircraft position. Three different algorithms are investigated for the lateral trajectory controller. All of them are described and simulation results are compared in the following sections.

4.4.1.1 Lateral Trajectory Controller A

In the first controller, a desired yaw angle for trajectory following is commanded based on the cross track error. All maneuvers are accomplished by using the rudder control, primary purpose of the ailerons are to keep the wings level. A mixing term is added between rudder and aileron to increase the maneuverability of the UAV. The block diagram of the autopilot is given in Figure 4.10.

A nonlinear track guidance algorithm for straight paths from [16] is implemented into the simulation. This guidance law selects a desired location ahead of the UAV by kx_{error} , where k is a user defined parameter determining where the UAV will start approaching the second waypoint at x_{error} in a straight flight condition (Figure 4.11). If k is selected as 1, the desired

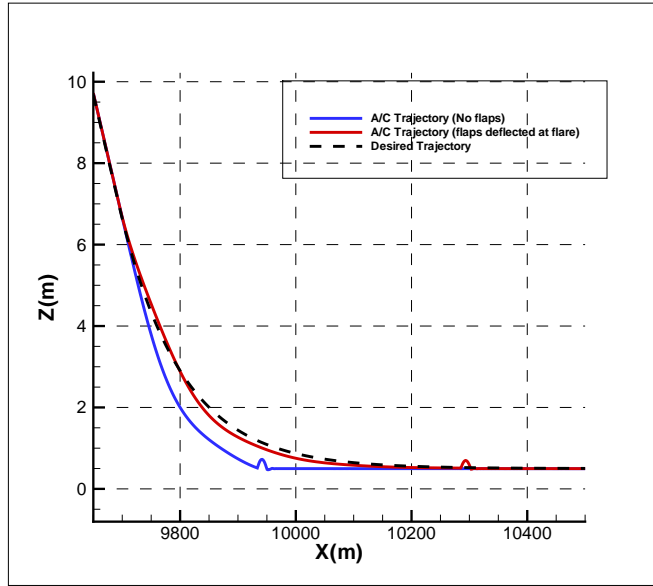


Figure 4.9: Effect of flaps on longitudinal autopilot

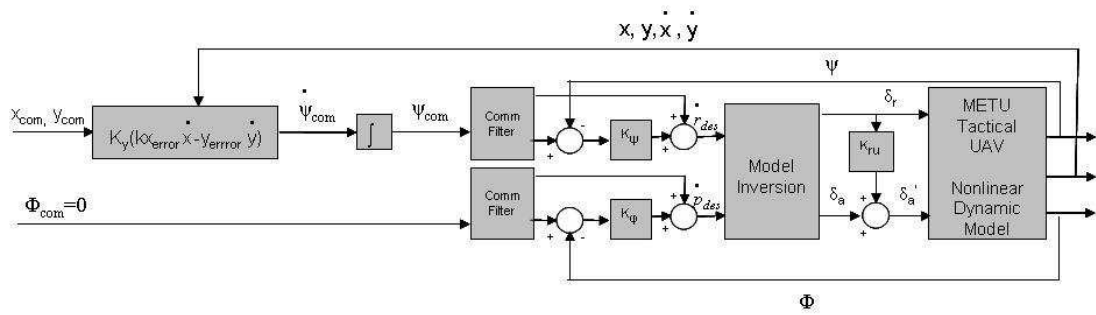


Figure 4.10: Lateral Controller Architecture A

location will be the 2nd waypoint itself, and the A/C will go straight to that waypoint in a straight trajectory, hence in a shorter time. However, it is not always possible to achieve close trajectory following if the second waypoint is not far enough away. In that case, it is more desired to choose $k < 1$ and allow the aircraft to approach that waypoint in a straight conditioned flight. This allows a closer following of the aircraft in presence of controller uncertainty, but will take longer. Note that, no parameter gain scheduling or adaptation is enabled in the controller described above. Therefore $k = 0.2$ is selected in the means below for perfect trajectory tracking. Simulation results between waypoints (0,0) and (10000,0) for different k values are presented in Figures 4.12 and 4.13. In Figure 4.12, the wind speed is zero and an initial lateral position error of 100 m is given to the UAV. In Figure 4.13, the response of the system to 10m/s

crosswind is observed. In both simulations, $k=0.2$ gives consistent results and converges to the second waypoint successfully. In such an approach the guidance law will align the ground

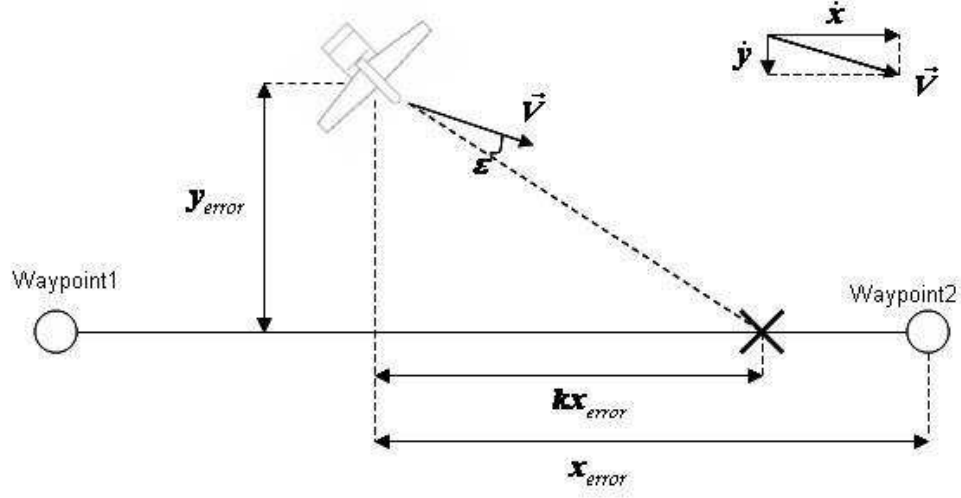


Figure 4.11: Lateral guidance law introduced by [16]

velocity vector of the UAV with the imaginary straight line between the UAV and the selected point (minimize ϵ in fig 4.11). \dot{x} and \dot{y} are ground velocity components parallel and normal to desired path, respectively. y_{error} is the perpendicular distance of the UAV to the desired path. The necessary yaw rate is found to minimize ϵ using equation 4.13[16]:

$$\dot{\psi}_{com} = K_y(kx_{track}\dot{y} - y_{track}\dot{x}) \quad (4.13)$$

K_y is the lateral control gain in the equation and is selected as 0.0001. ψ_{com} is updated after every iteration using $\dot{\psi}_{com}$.

Roll channel is only used to level the wings which reduces the performance of the lateral trajectory controller. Rudder is mixed with the aileron to compensate this. So, the total aileron deflection commanded to the actuators become:

$$\delta'_a = \delta_a + K_{ru}\delta_r \quad (4.14)$$

δ_a term is obtained from the roll channel autopilot and second term comes from mixing. Effect of mixing is investigated in 10 m/s crosswind and moderate turbulence cases. Figure 4.14 shows the response of the autopilots with and without rudder-aileron mixing under crosswind.

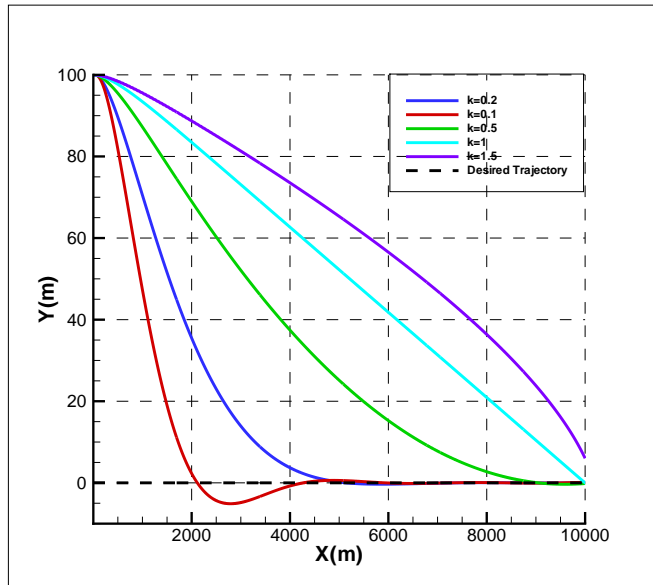


Figure 4.12: Simulation results for different k

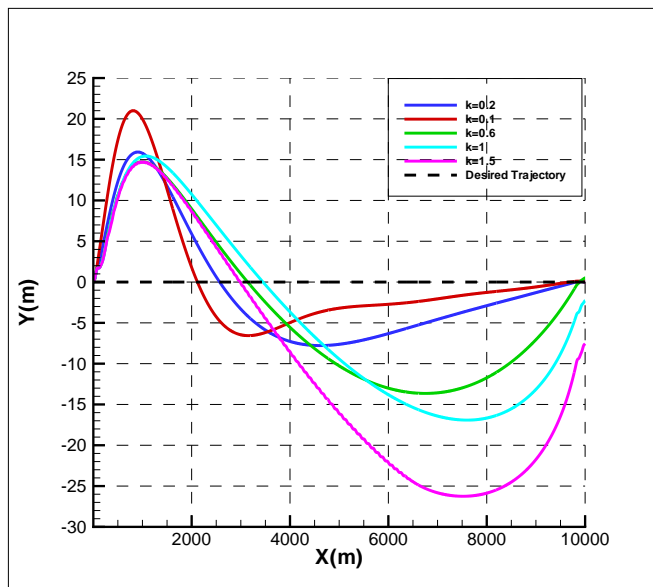


Figure 4.13: Simulation results for different k under crosswind

The initial cross track error is reduced significantly when the mixing term is added. Later on, performance of the autopilots are similar. In turbulent weather case(Figure 4.15) the autopilot with rudder-aileron mixing shows better performance throughout the flight. Hence, mixing term increases the performance of the system under sudden disturbances.

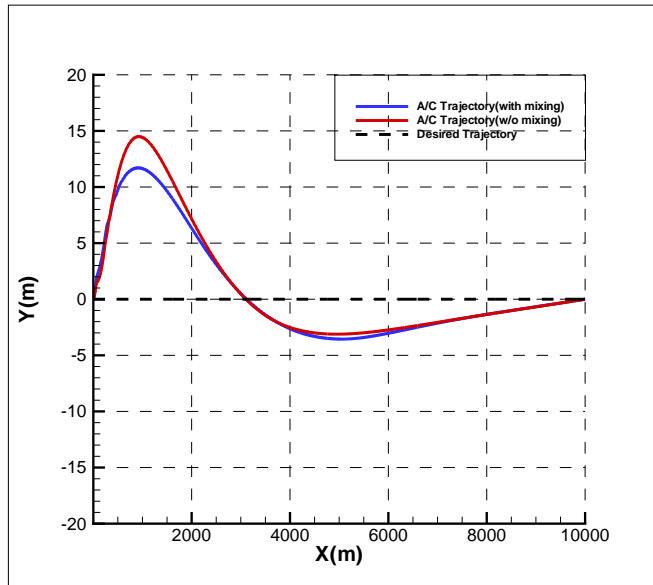


Figure 4.14: Effect of rudder-aileron mixing under crosswind

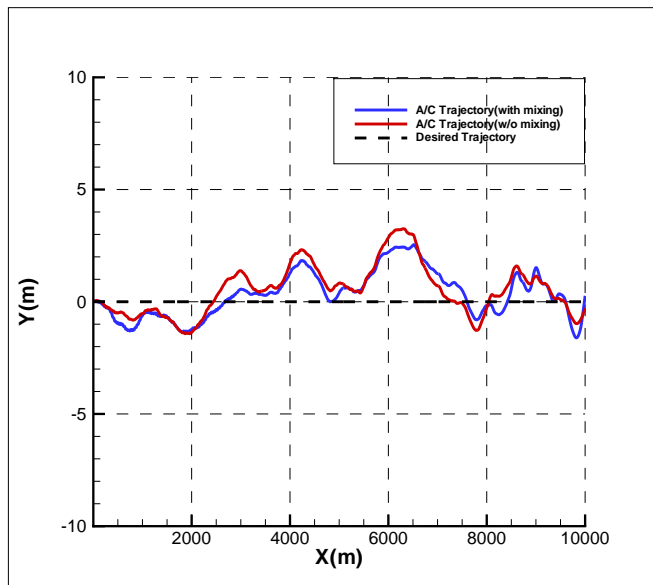


Figure 4.15: Effect of rudder-aileron mixing under turbulence

4.4.1.2 Lateral Trajectory Controller B

In this architecture, the lateral error is minimized using the roll channel and the lateral acceleration minimized by rudder. The block diagram of the system is presented in Figure 4.16. Beside the cross track error, y_{error} , the difference between the A/C's velocity direction and the desired direction is also used to estimate the cross track error ahead of time[20]. This limits the variation in the A/C heading and damps the lateral position signal. The lateral error relation

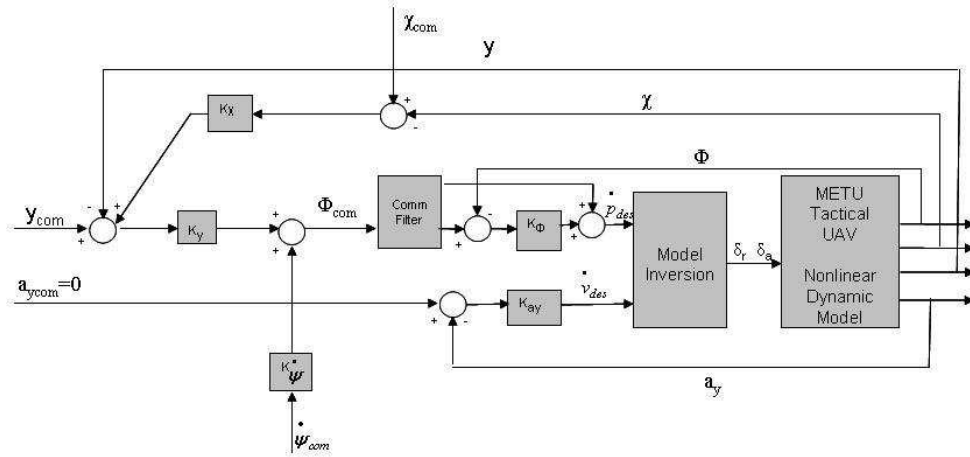


Figure 4.16: Lateral controller architecture B

is:

$$y_{errorah} = y_{error} + U_{des}\Delta t\eta \quad (4.15)$$

U_{des} is assumed to be the same as the total A/C velocity, V_{des} . Δt is the time constant and η is the velocity direction error. The definition of these variables and the application of the law to a circular trajectory is shown in Figure 4.17. Δt is selected as 13s in the controller. In circular

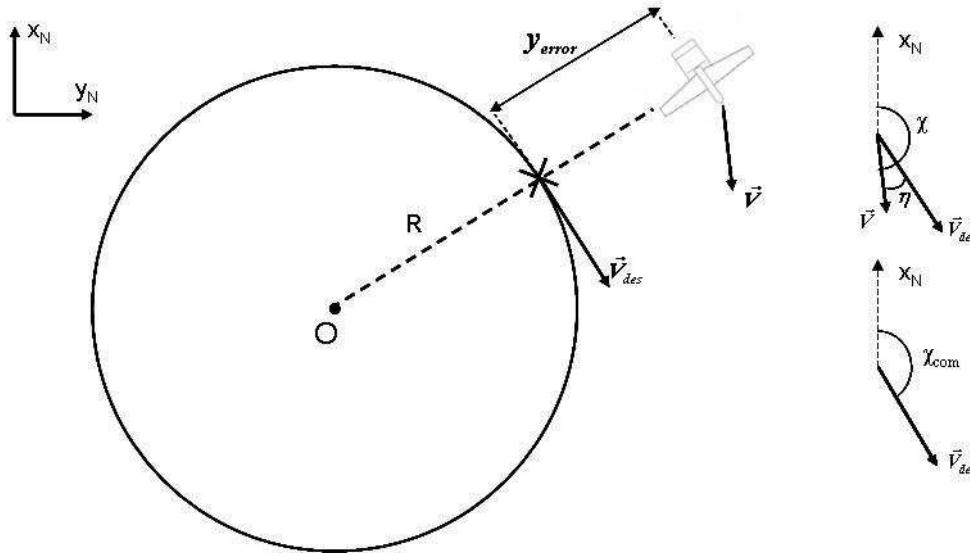


Figure 4.17: Application of control law B to a circular trajectory

trajectories, the reference point is determined by the position of the UAV w.r.t the center of the circle. The PI controller is used to reduce $y_{errorah}$. The yaw rate as a feed forward term is added to the system to achieve better performance in tracking[15]. The desired yaw rate for a

circular trajectory is:

$$\dot{\psi}_{com} = \frac{U_{des}}{R} \quad (4.16)$$

where, R is the radius of the circle. The effect of the yaw rate term on the autopilot is tested on two different trajectories. Firstly, the UAV is expected to follow a simple circular trajectory with a radius of 750m. As observed in Figure 4.18, the feed forward term benefits the response. The second trajectory consists of two consecutive circles and the UAV first circles clockwise and then counterclockwise as seen in Figure 4.19. The effect of the feed forward term is more obvious in the transition from the clockwise to counterclockwise rotation shown in Figure 4.20. The relation between the roll angle command and cross track error in the outer loop is:

$$\phi_{com} = K_{p_y}(y_{errorah}) + K_{i_y} \int y_{errorah} + K_{\dot{\psi}} \dot{\psi}_{com} \quad (4.17)$$

The selected gains are shown in table 4.5.

Table 4.5: y controller gains

	K_p	K_i	$K_{\dot{\psi}}$
y	0.002	0.0001	5

The lateral acceleration is controlled by the rudder to provide yaw stability. Inverted equations for the lateral dynamics are shown in the following equation.

$$\begin{bmatrix} \delta_r \\ \delta_a \end{bmatrix} = \begin{bmatrix} -\frac{L_a + N_a A_1}{G_2} & \frac{Y_a(1 - A_1 B_1)}{G_2} \\ \frac{L_r + N_r A_1}{G_2} & -\frac{Y_r(1 - A_1 B_1)}{G_2} \end{bmatrix} \begin{bmatrix} \dot{v}_{des} \\ \dot{p}_{des} \end{bmatrix} - \begin{bmatrix} \frac{Y_\beta}{U_{cr}} & Y_p \\ \frac{L_\beta + A_1 N_\beta}{(1 - A_1 B_1) U_{cr}} & \frac{L_p + A_1 N_p}{1 - A_1 B_1} \end{bmatrix} \begin{bmatrix} v \\ p \end{bmatrix} - \begin{bmatrix} Y_r - U_{cr} & g \cos \theta_{cr} \\ \frac{L_r + A_1 N_r}{1 - A_1 B_1} & 0 \end{bmatrix} \begin{bmatrix} r \\ \Delta\phi \end{bmatrix}$$

where;

$$G_2 = -Y_r L_a - Y_r N_a A_1 + Y_a L_r + N_r Y_a A_1 \quad (4.18)$$

$\Delta\phi$ is the perturbed roll angle in the equation. No command filter is necessary for the lateral acceleration control as it is always commanded zero. A PI controller is sufficient in this case.

$K_{p_{a_y}}$ and $K_{i_{a_y}}$ are selected as 0.2 and 0.001, respectively.

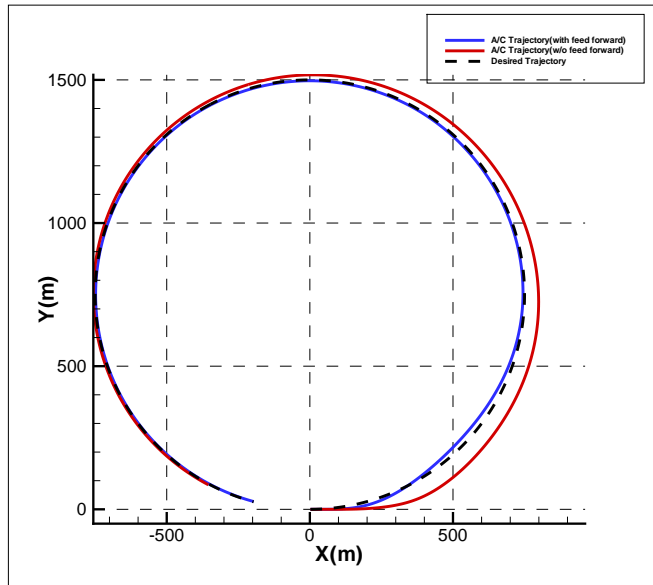


Figure 4.18: Comparison of autopilots with and without feeding $\dot{\psi}$ forward(circular trajectory)

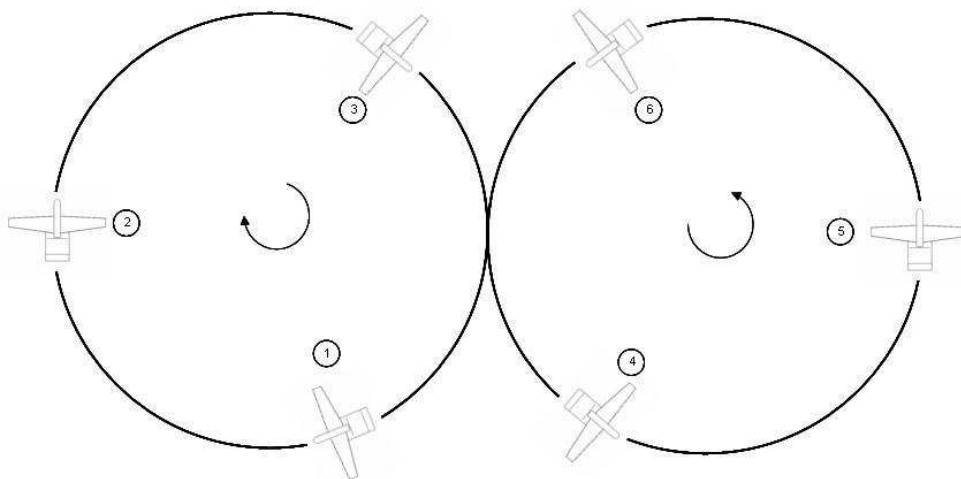


Figure 4.19: Description of the maneuver in figure 4.20

4.4.1.3 Lateral Trajectory Controller C

Third controller is designed based on [29]. Here the cross track error is used to generate a yaw angle command, which is connected to generate another roll angle command. The yaw angle loop provides a smoother convergence and performs better to hold a level flight condition in crosswind. The roll momentum equation is inverted in the inner most loop. The yaw rate is controlled by the rudder to damp the yaw motion. The block diagram is presented in figure 4.21. The desired yaw angle is approximated using the following formula:

g is the gravity. The value of Δt_ψ determines the gain K_ψ . Δt_ψ is selected as 3s.

4.4.1.4 Comparison of Lateral Controllers

Performance of the three lateral autopilots are compared in this section.

A straight trajectory with length 10000m is generated between the waypoints $P_1(0,0)$ and $P_2(0,10000)$. In the first simulation, the UAV is initially assumed to be at $P_{A/C}(0,100)$. Results are shown in figure 4.22.

The autopilot B gives the best results while converging at 4000 m. The performance of the other two autopilots are similar and both systems converge at 6000 m.

Next, the response of the closed loop systems are compared for a crosswind condition of 10 m/s. Results are shown in Figure 4.23. A lateral error was introduced at the beginning of the simulation. The maximum cross track errors were 10m for autopilot A, while for autopilots B and C the maximum error were 40 m and 100 m, respectively. The response of the first autopilot is faster than the other two for windy cases. Attitude of the A/C during second simulation is given in Figure 4.24. First and third autopilots keeps the wings level after they converge to the trajectory and fly with a crab angle. However, in controller B, crab angle increases significantly since wings are not leveled. Cross track error signal is transmitted directly to roll channel and due to integral term in outer loop, autopilot commands a constant roll angle at windy conditions.

Finally, the first autopilot is selected as the lateral controller for landing after comparing the three alternatives. The nonlinear guidance law shows good performance under different conditions without the necessity of gain scheduling.

4.4.2 Decrab Control

As mentioned before, the crab angle is reduced prior to touchdown in order to avoid large lateral movements when the aircraft touches the ground and not damage the landing gears. The heading angle control is necessary at this point. Two alternatives are investigated for the decrab maneuver: First one is when the inner loop of the lateral controller A is used (Figure 4.25). The yaw angle is controlled by the rudder and the roll angle is controlled by the ailerons.

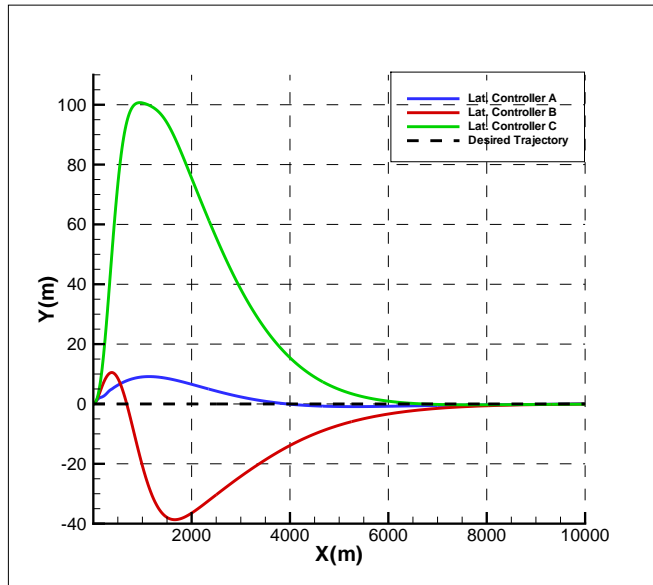


Figure 4.22: Comparison of the lateral controllers following a straight trajectory(no wind)

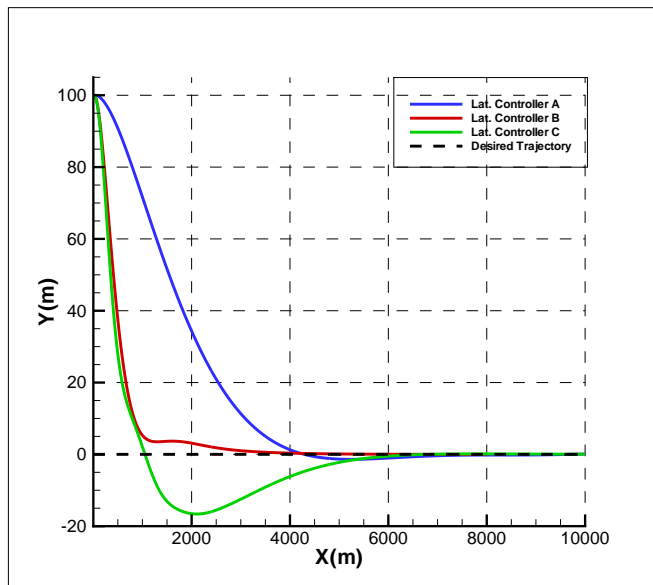


Figure 4.23: Comparison of the lateral controllers following a straight trajectory(10 m/s crosswind)

The second alternative is the use of the inner loop of the controller C (Figure 4.26). The yaw angle is controlled by the aileron and the rudder works similar to a yaw damper. Both autopilots are tested under a 10 m/s crosswind. At $t= 250$ s the autopilot is commanded to reduce the yaw angle to 0 deg and align the heading with the trajectory. A comparison of autopilots are shown in Figures 4.27 and 4.28. Results clearly show that the crab angle must be reduced by the rudder. In the first autopilot, the yaw angle is reduced from 16 deg to 0 in 3

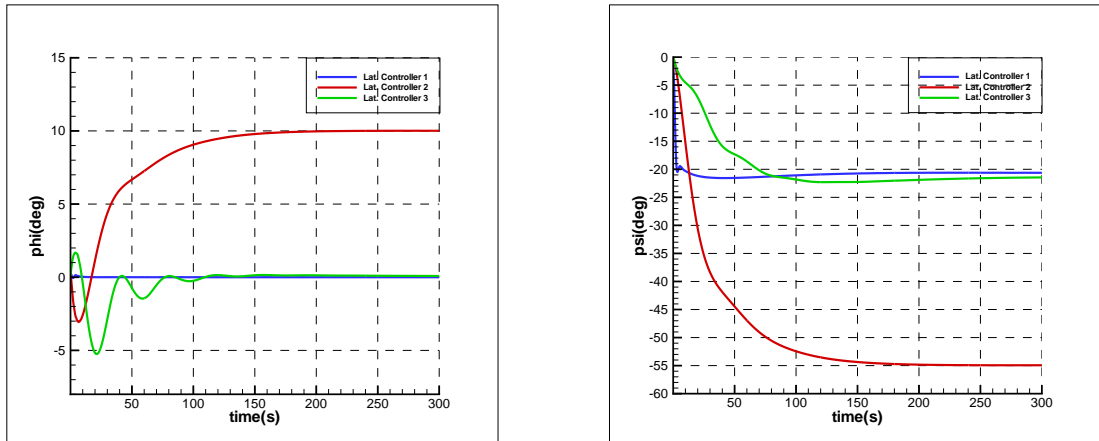


Figure 4.24: Comparison of yaw and roll angle controls of autopilots under 10 m/s crosswind

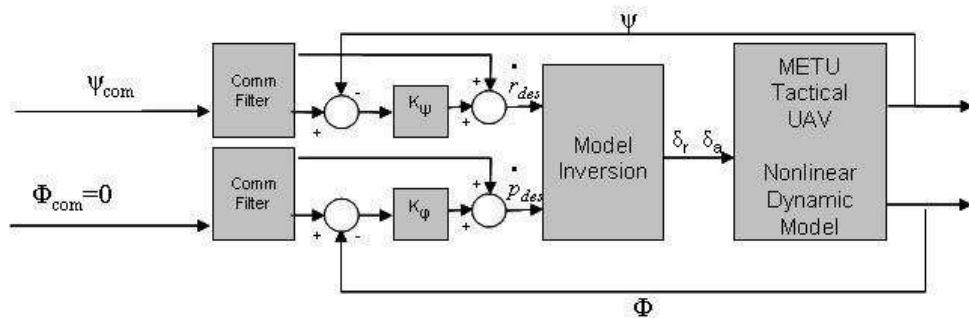


Figure 4.25: Decrab control by rudder

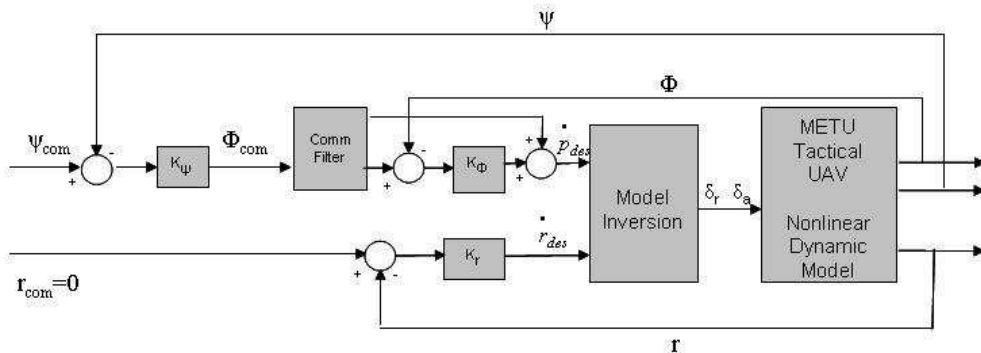


Figure 4.26: Decrab control by aileron

seconds with almost no overshoot. The A/C is able to keep the wings level at the same time. However, the second autopilot converges nearly in 10 seconds after some oscillations. The roll angle reaches 20 deg at the beginning of the maneuver. 13 deg is the limit for the A/C to avoid hitting the wing tips to the ground. So, the roll angle command should be limited by 10 deg at landing, which will reduce the performance of the second controller even more. Furthermore,

the large deviations in roll channel changes the lift vector direction significantly. The UAV might not be able create enough force to compensate its weight which will result in a sudden descent and generate a strong impact on landing gears.

The decrab maneuver should be controlled by the rudder since it is the dominant control surface on the yawing motion and gives better results compared to decrabing by the aileron.

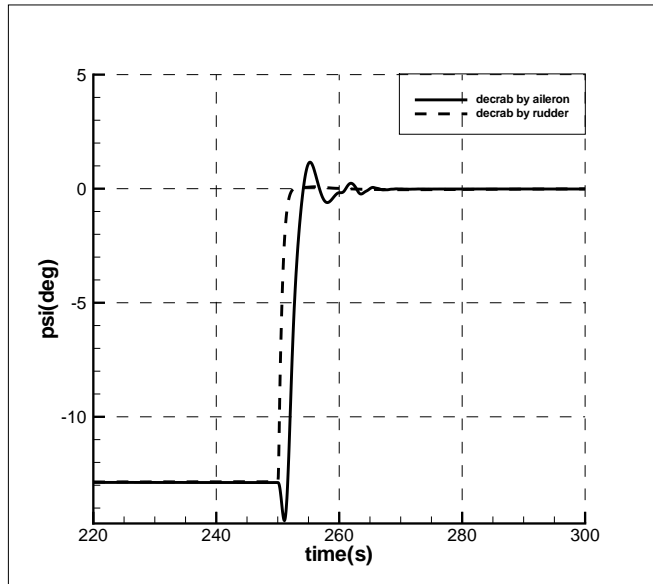


Figure 4.27: Response of yaw angle at decrab maneuver

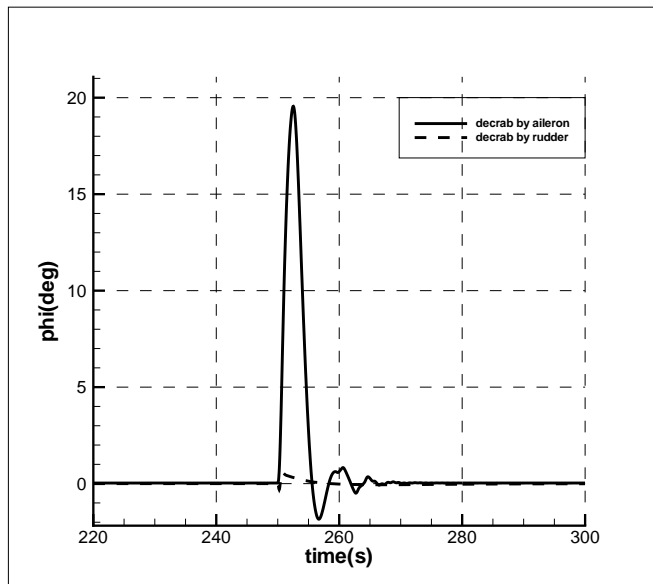


Figure 4.28: Response of roll angle at decrab maneuver

CHAPTER 5

SIMULATION RESULTS

The simulation results of autonomous landing of METU TUAV are presented in this chapter. Simulation cases are selected for different wind conditions. Strength of wind and turbulence is decided investigating wind limits of other UAVs. Wind limits for some UAVs are given in Table 5.1. [18][32][19] Predator and Heron UAVs are from upper classification compared

Table 5.1: Competitor study on wind limits of UAVs

UAV	Head wind (m/s)	Tail wind (m/s)	Side wind (m/s)
Predator	15	N/A	7.5
Heron	10	2.5	7.5
Kingfisher	N/A	N/A	10

to METU TUAV. Only Kingfisher is in the same category. However, their mission profile is similar to METU TUAV so, wind profiles are determined based on these references. Winds limits for landing of METU TUAV is selected as 15 m/s head wind, 2.5 m/s tail wind and 10 m/s crosswind. 5 different simulation cases are investigated:

- No wind- no turbulence
- 15 m/s head wind + turbulence
- 2.5 m/s tail wind + turbulence
- 10 m/s crosswind + turbulence

- windshear + turbulence

Autopilot is active from the beginning of the simulation until touchdown. No attempt was made to control the UAV after touchdown on the ground in these simulation results. Only, elevator deflection is forced to zero and rpm is forced to its idle position after touchdown.

5.1 Case 1: No Wind, No Turbulence

The aircraft follows the desired trajectories very closely. The maximum error in height seen is approximately 1m during transition from level flight to descent(Figure 5.2) and the cross- track error is less than 0.4m (Figure 5.3) at the beginning of the simulation. In Figure 5.5, it can be seen that flare maneuver is successfully completed with maximum error of 0.1m. Descent rate is reduced nearly to zero prior to touchdown. Touchdown occurs at $t=115s$. An error in the lateral deviation is observed due to the unbalance caused by the roll angle, and heading error at touchdown. Overshoot in yaw and roll angles are damped out by ground forces in 4 seconds. Inner loops of the autopilot works very good; the input is followed during the flight(Figure 5.6). Reduction in speed due to friction forces can be observed in Figure 5.4.

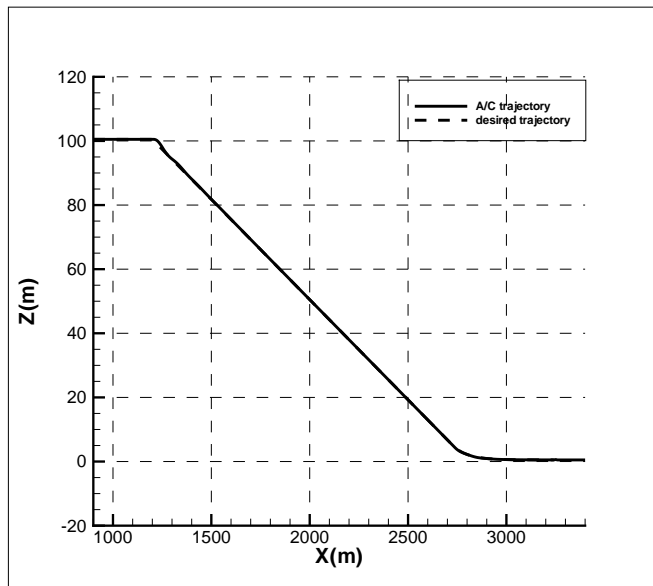


Figure 5.1: Longitudinal trajectory

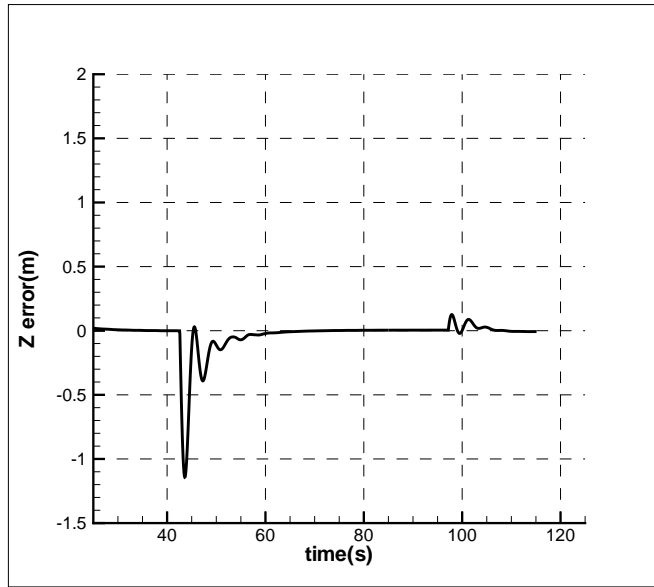


Figure 5.2: Altitude error

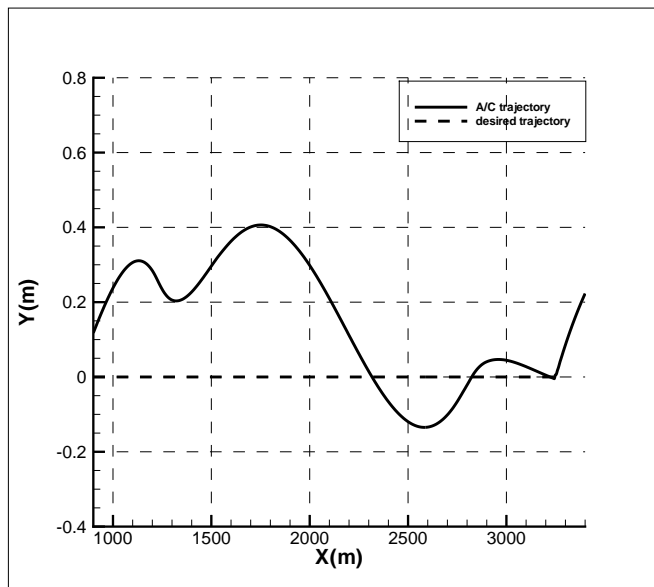


Figure 5.3: Lateral trajectory

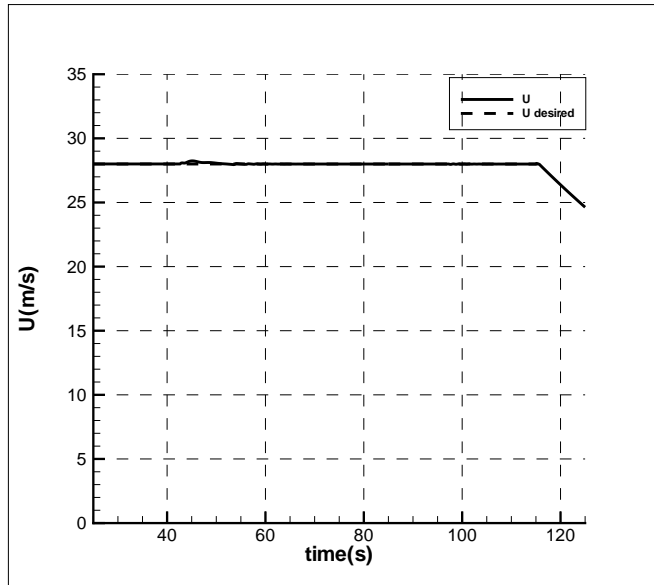


Figure 5.4: Forward velocity

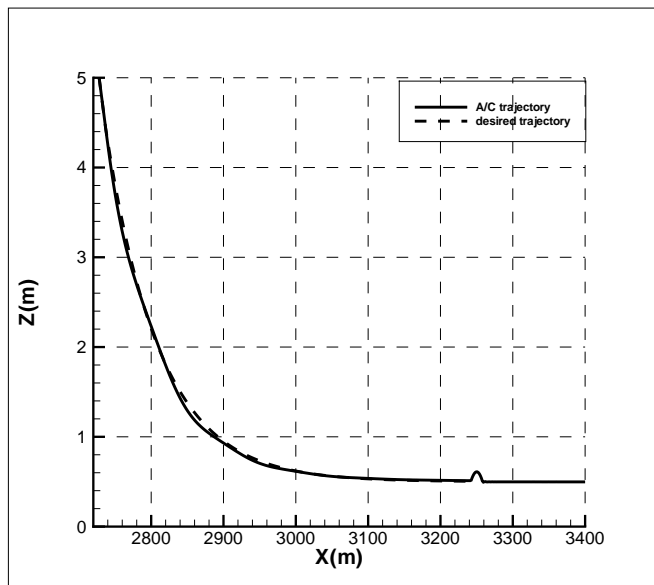


Figure 5.5: Flare maneuver

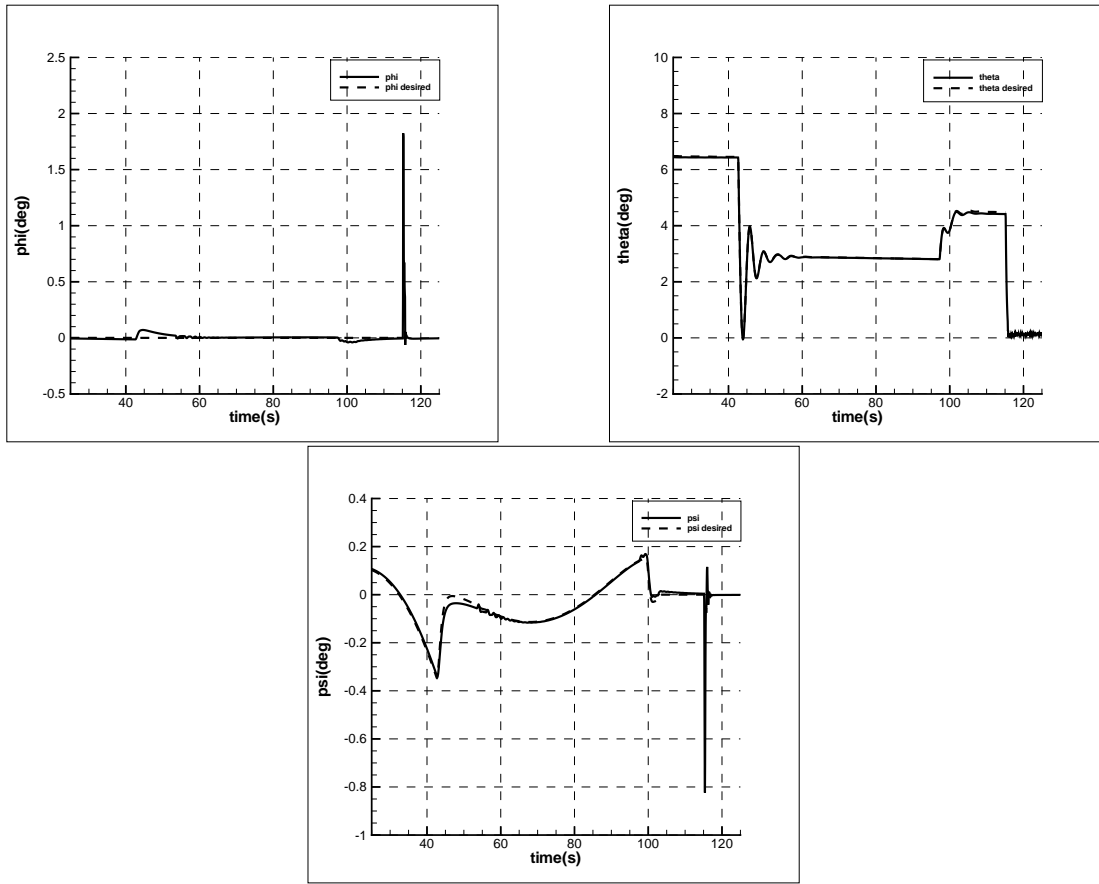


Figure 5.6: Euler angles

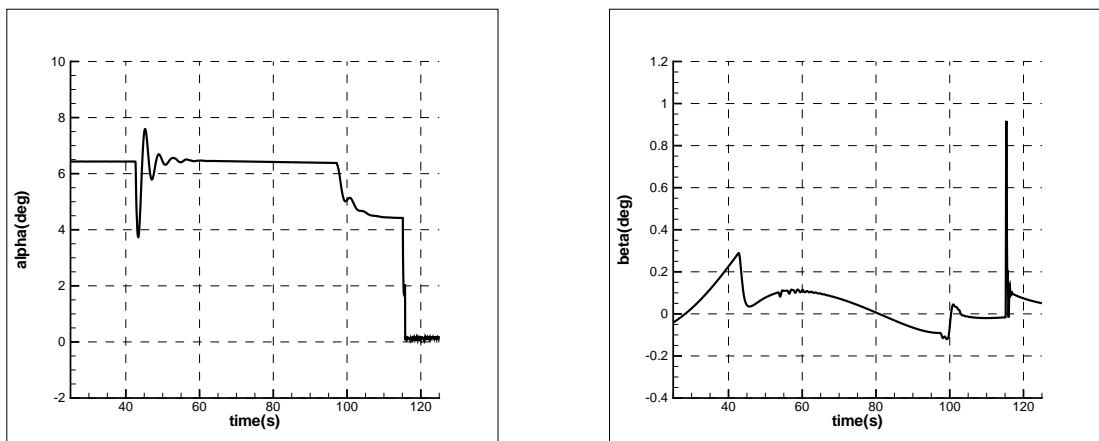


Figure 5.7: Angle of attack and sideslip angle

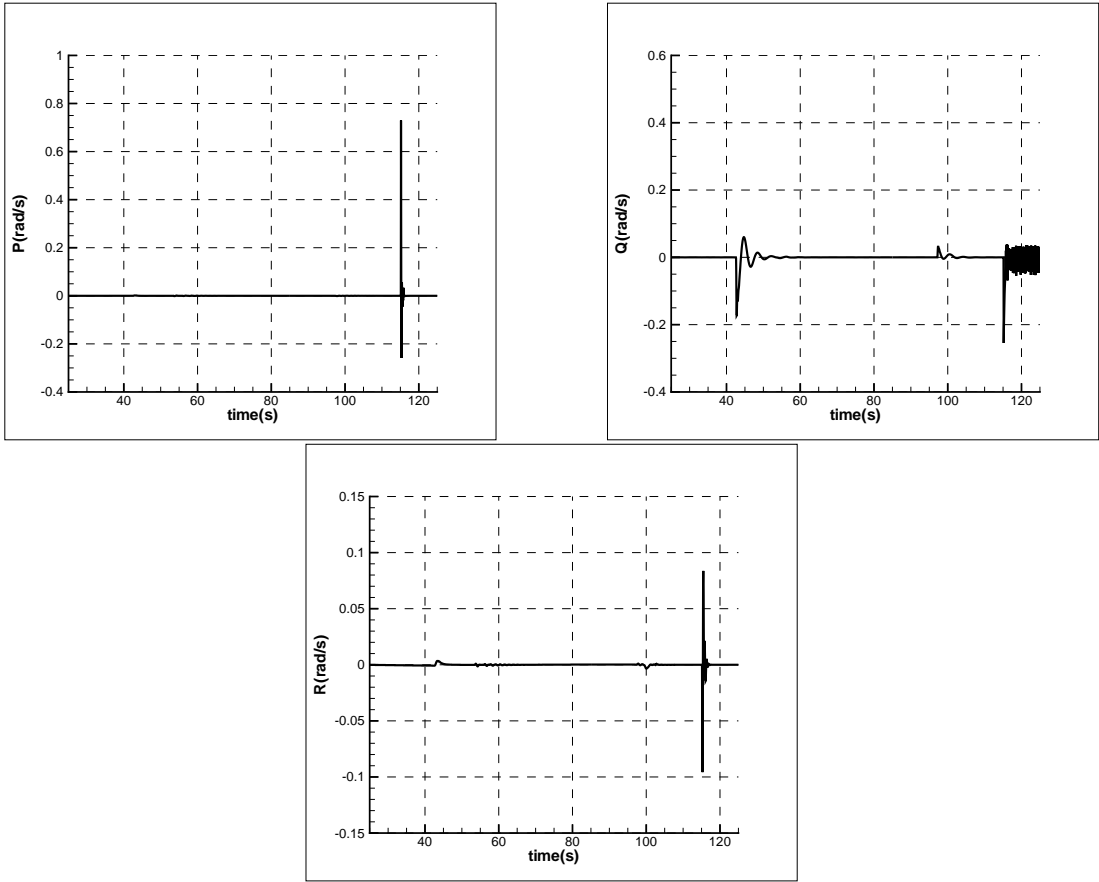


Figure 5.8: Body angular rates

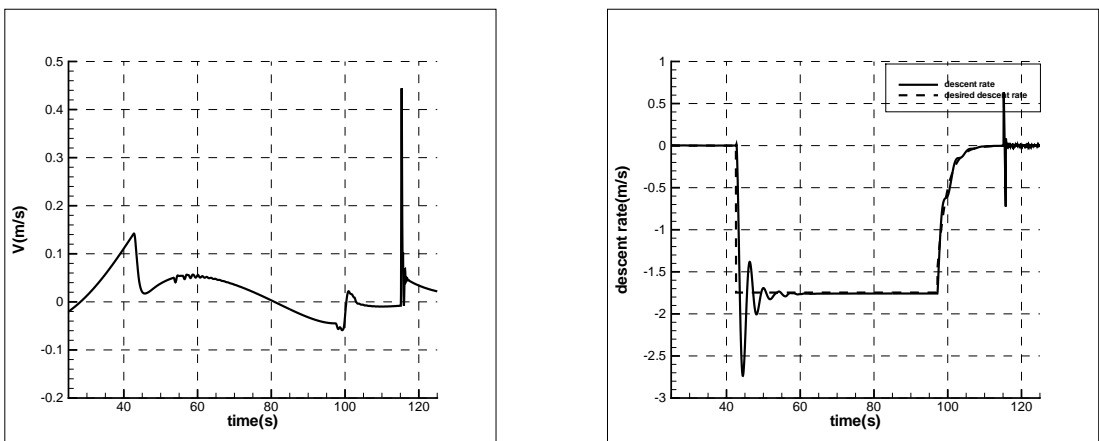


Figure 5.9: Side velocity and descent rate

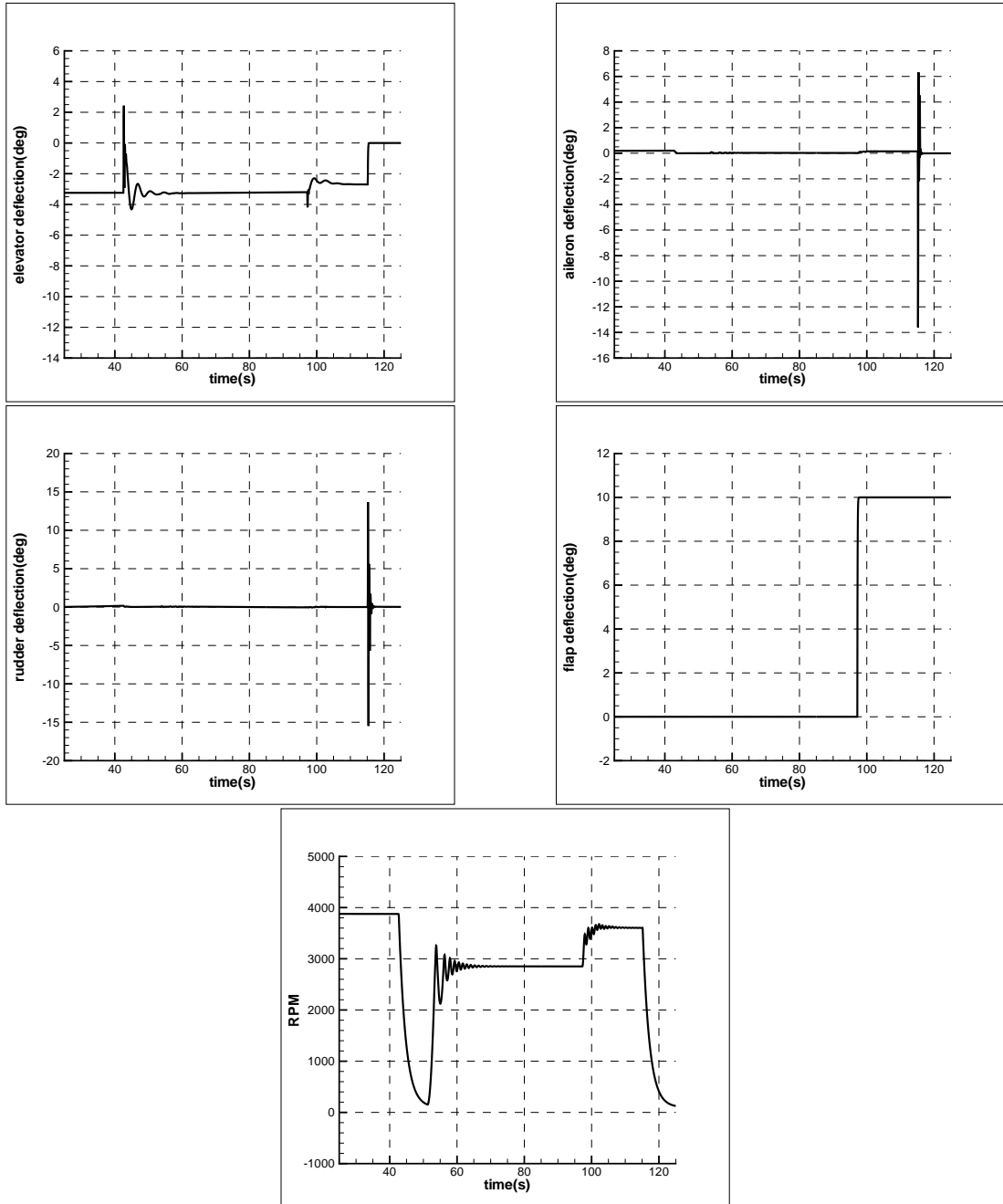


Figure 5.10: Control surface deflections

5.2 Case 2: 15 m/s Head Wind + Turbulence

Wind and turbulence profile of case 2 is shown in Figure 5.11. First action autopilot commands

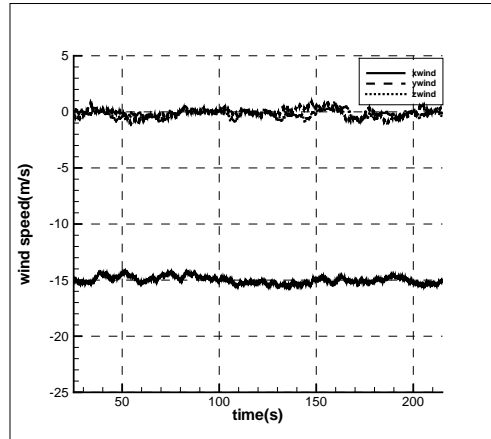


Figure 5.11: Wind profiles

under head wind is to reduce ground speed. Desired ground speed becomes 13m/s. Landing time increases significantly and landing phase is completed after 210s. UAV follows the trajectory with acceptable errors. Flare phase is initiated at $t=200s$. Flaps are not used in this case since maneuver is not very aggressive due to reduced ground speed. Oscillations are observed in longitudinal trajectory at flare(Figure 5.16). This is the result of the turbulence since order of magnitude of the altitude error is same as the rest of the simulation(Figure 5.13). Altitude error is nearly 0.15m at touchdown. Touchdown occurs at $t=210s$, 20 seconds after initiation of flare. Descent rate is far away from critical region although oscillations are observed.(Figure 5.20)

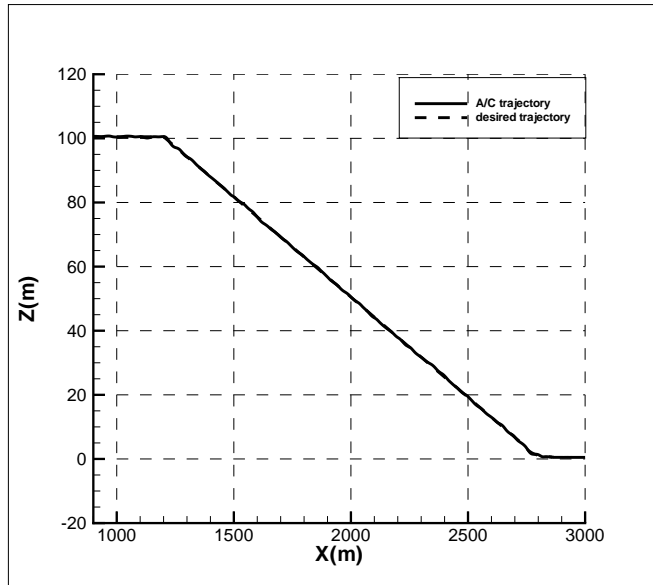


Figure 5.12: Longitudinal trajectory

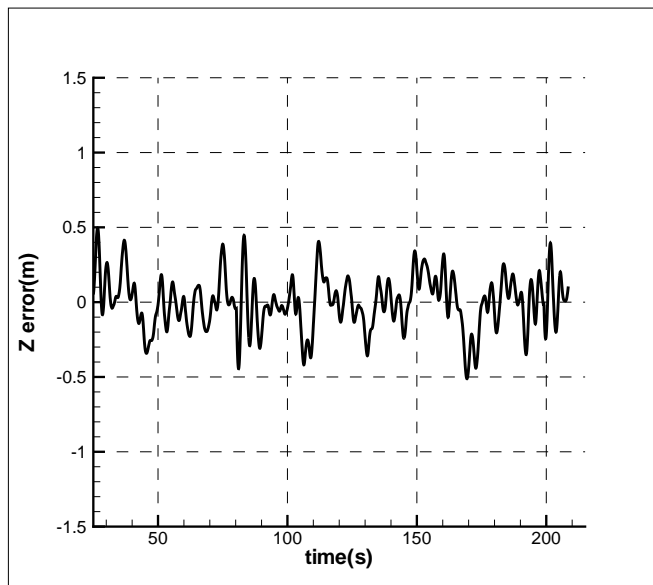


Figure 5.13: Altitude error

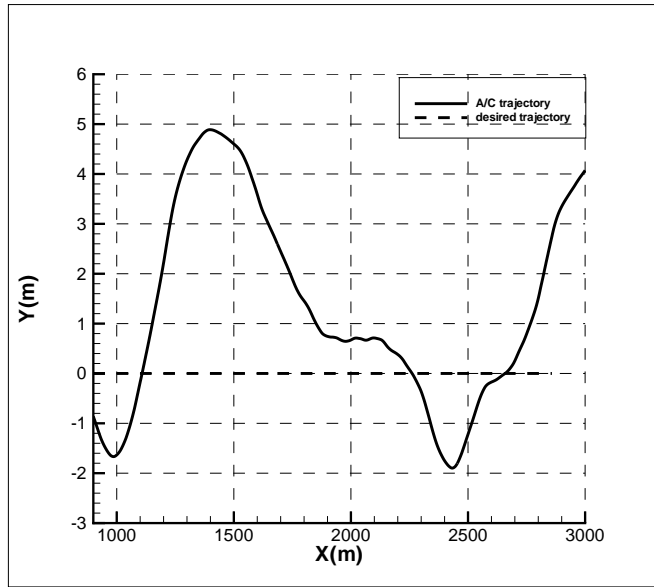


Figure 5.14: Lateral trajectory

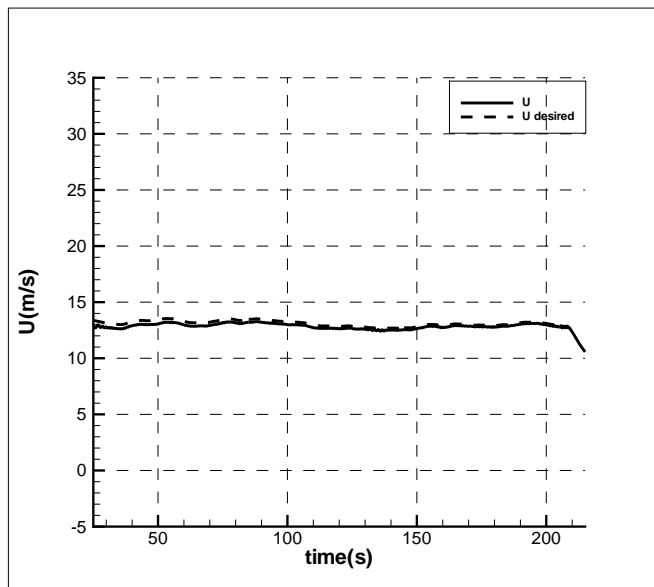


Figure 5.15: Forward velocity

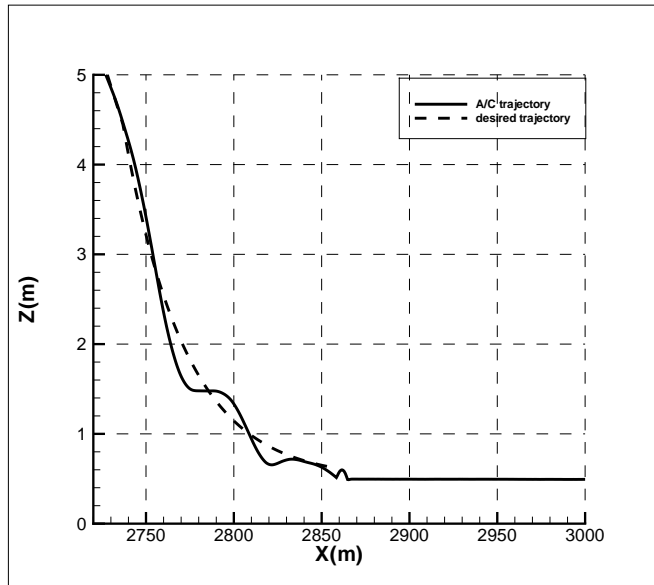


Figure 5.16: Flare maneuver

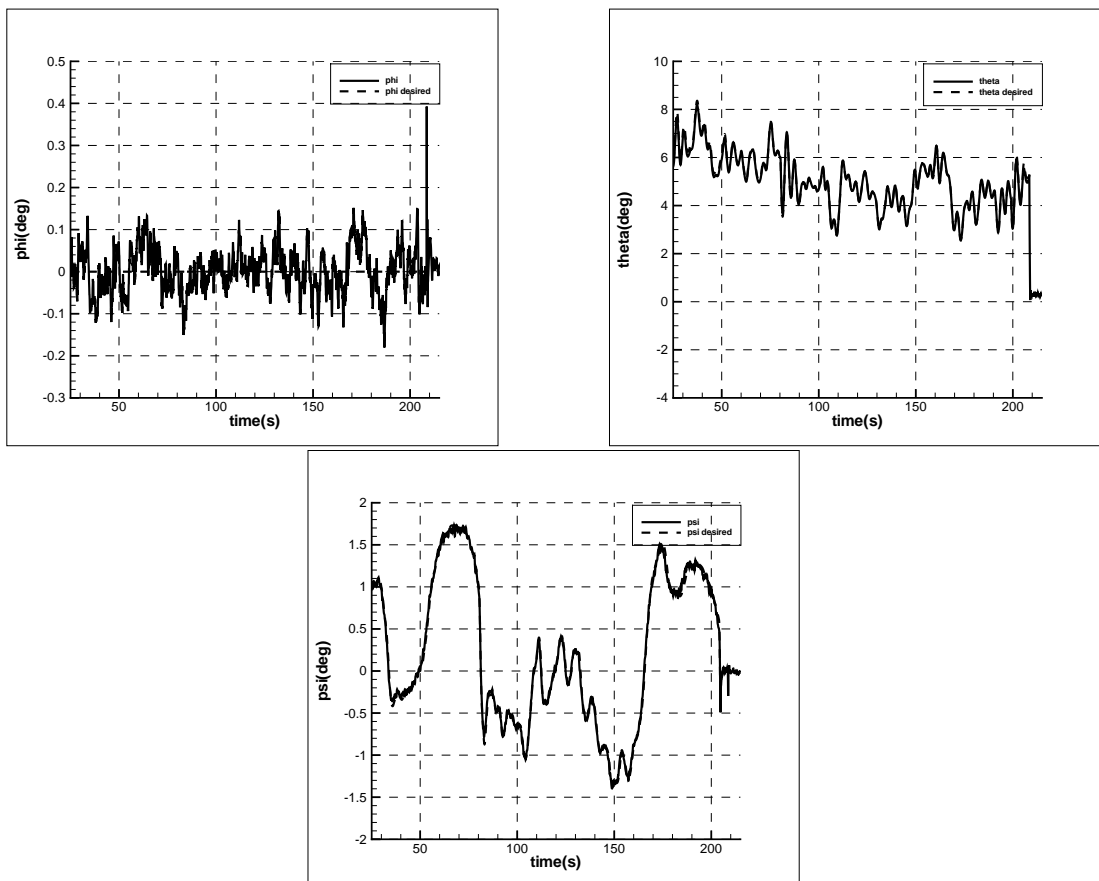


Figure 5.17: Euler angles

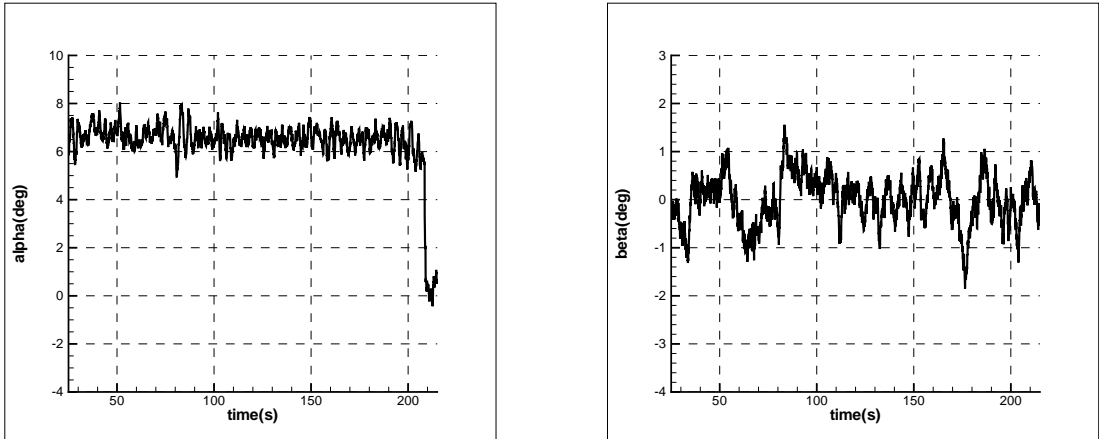


Figure 5.18: Angle of attack and sideslip angle

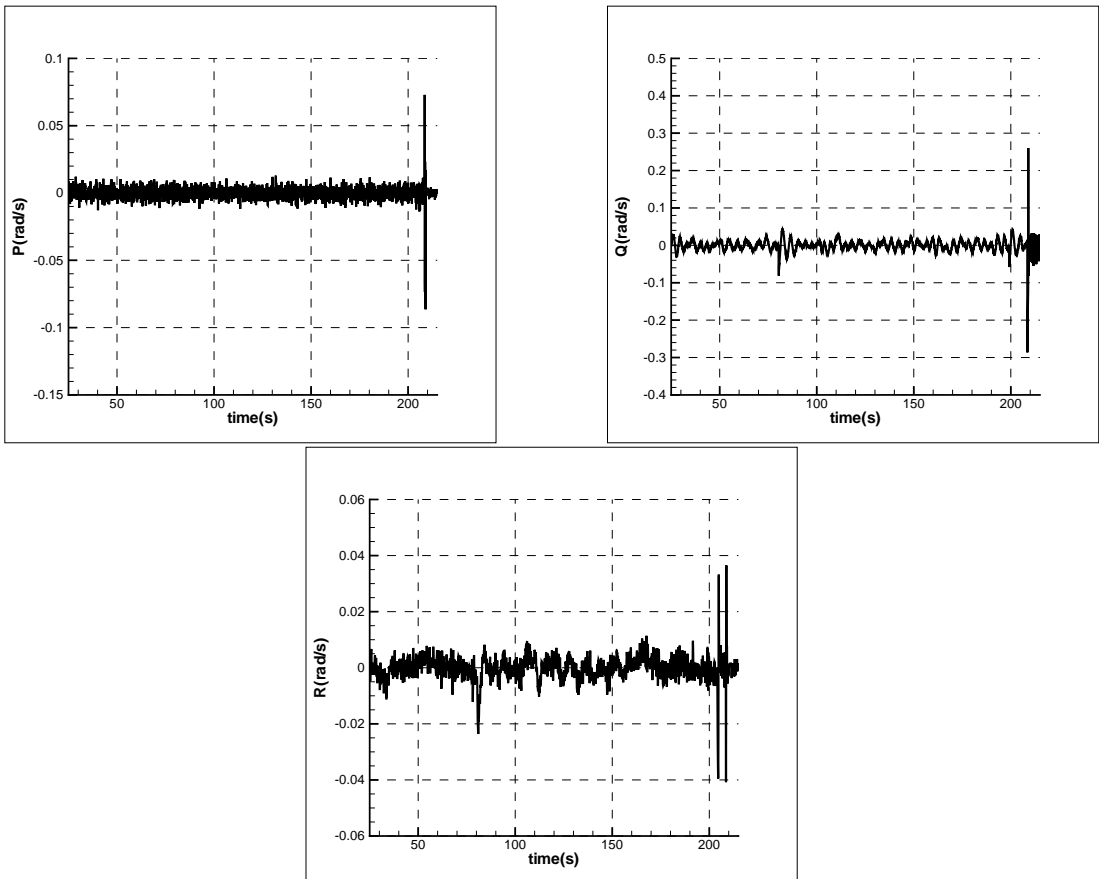


Figure 5.19: Body angular rates

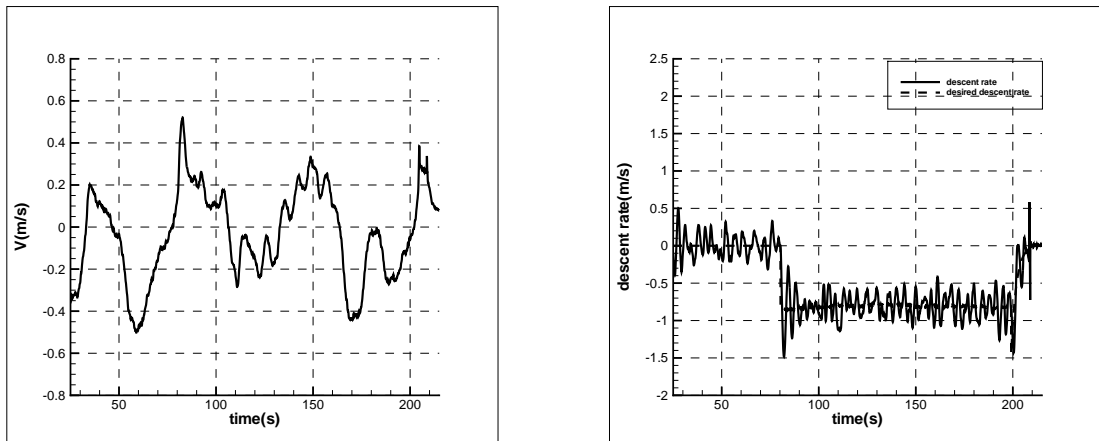


Figure 5.20: Side velocity and descent rate

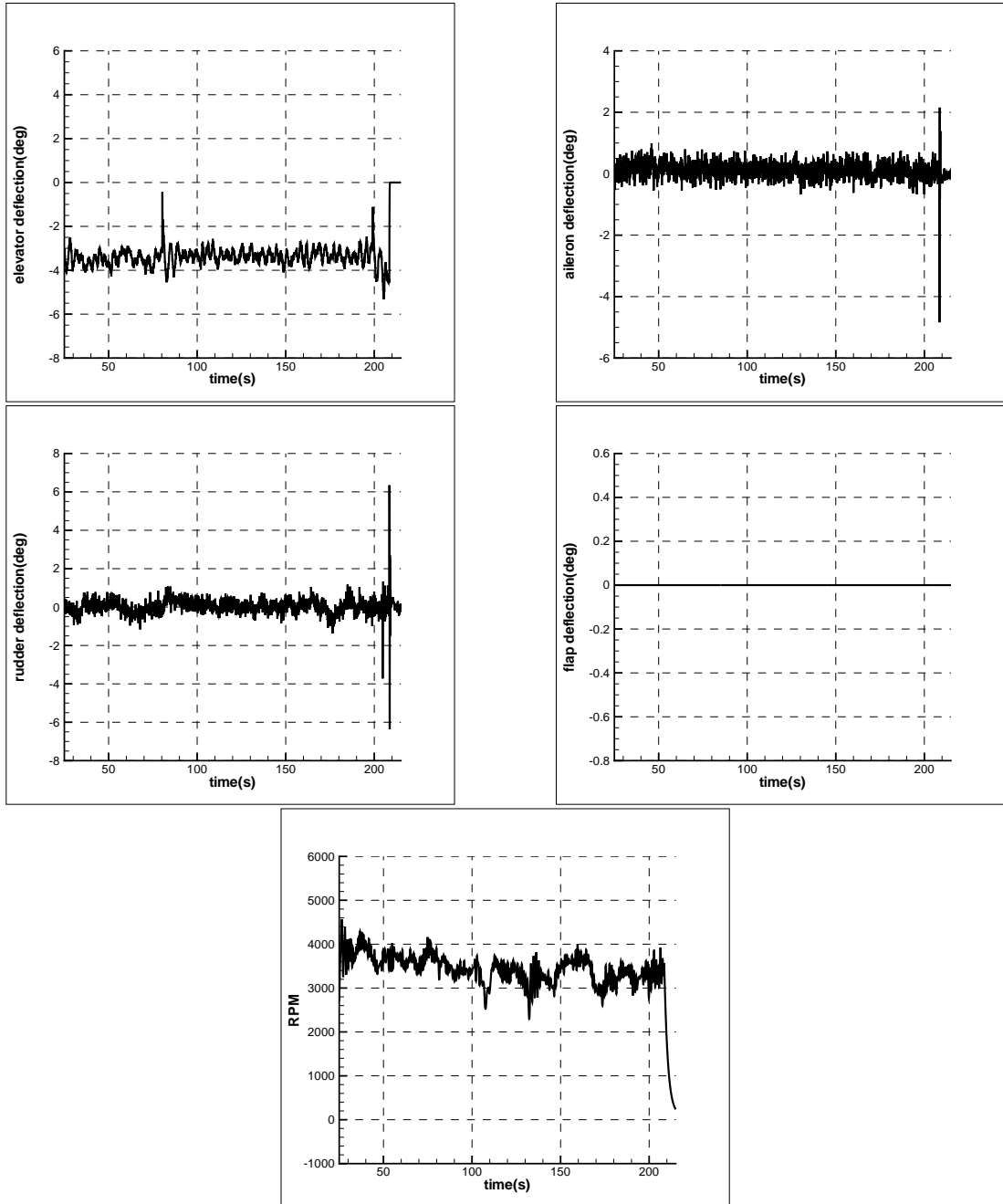


Figure 5.21: Control surface deflections

5.3 Case 3: 2.5 m/s Tail Wind + Turbulence

Wind disturbances are shown in Figure 5.22. Strength of the turbulence is reduced for this simulation. Lateral and longitudinal trajectory errors are reduced quickly as it can be seen in

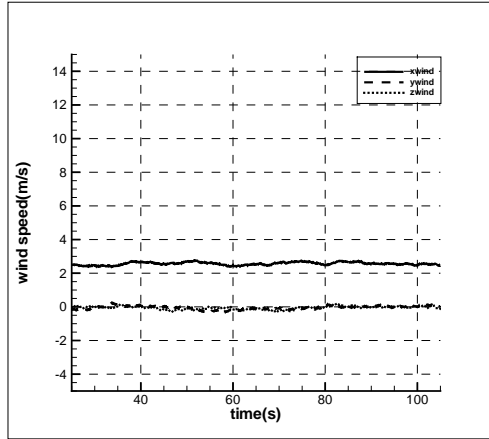


Figure 5.22: Wind profiles

figures 5.24 and 5.25. Major problem in this case is observed in velocity control. Unlike other cases, control authority of throttle over velocity is diminished from the initiation of descent phase. Engine rpm is reduced to its idle condition and no thrust is generated (figure 5.32). However, velocity increases in time until the UAV enters flare phase (figure 5.26). Pitch up maneuver and reduction of flight path angle results in velocity decrease. Flare is initiated at $t=87s$. Control of flare maneuver is harder than other cases because velocity can not be controlled properly. Landing occurs at $t=94s$ with an altitude error of 0.3m. Descent rate is 0.15m/s at touchdown.

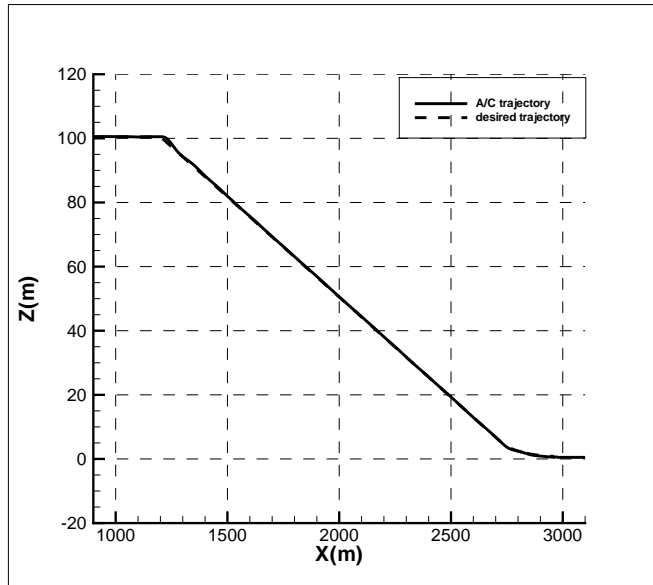


Figure 5.23: Longitudinal trajectory

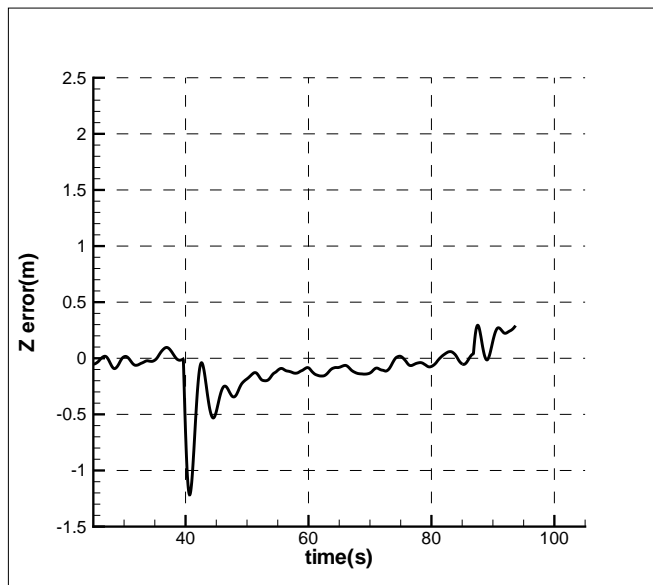


Figure 5.24: Altitude error

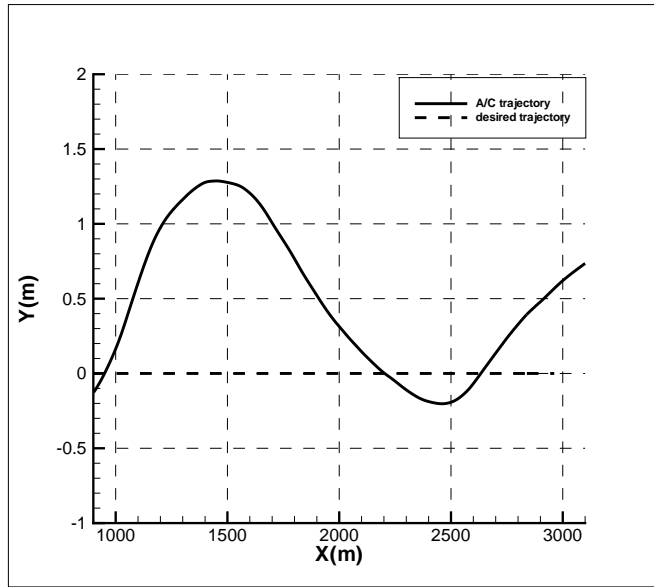


Figure 5.25: Lateral trajectory

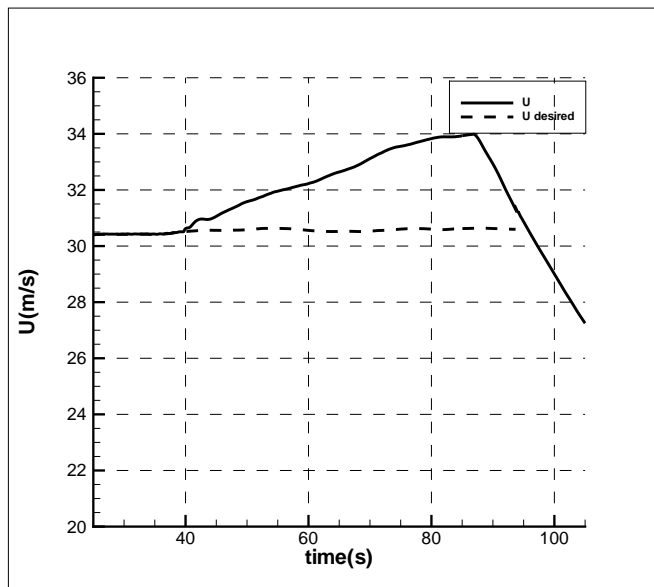


Figure 5.26: Forward velocity

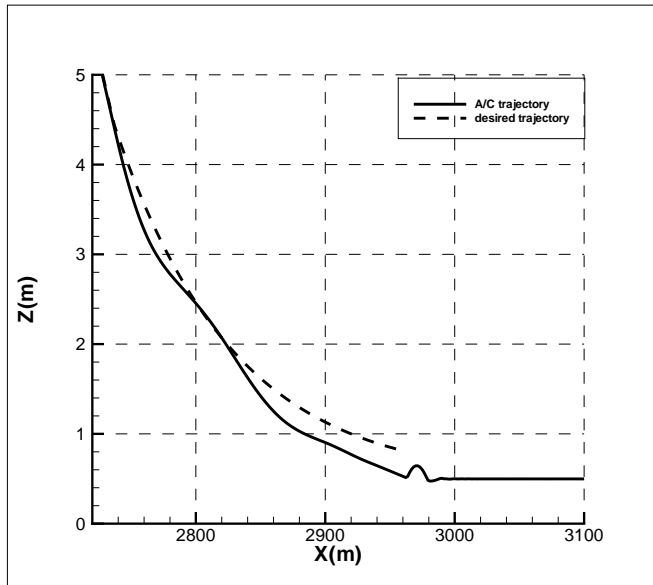


Figure 5.27: Flare maneuver

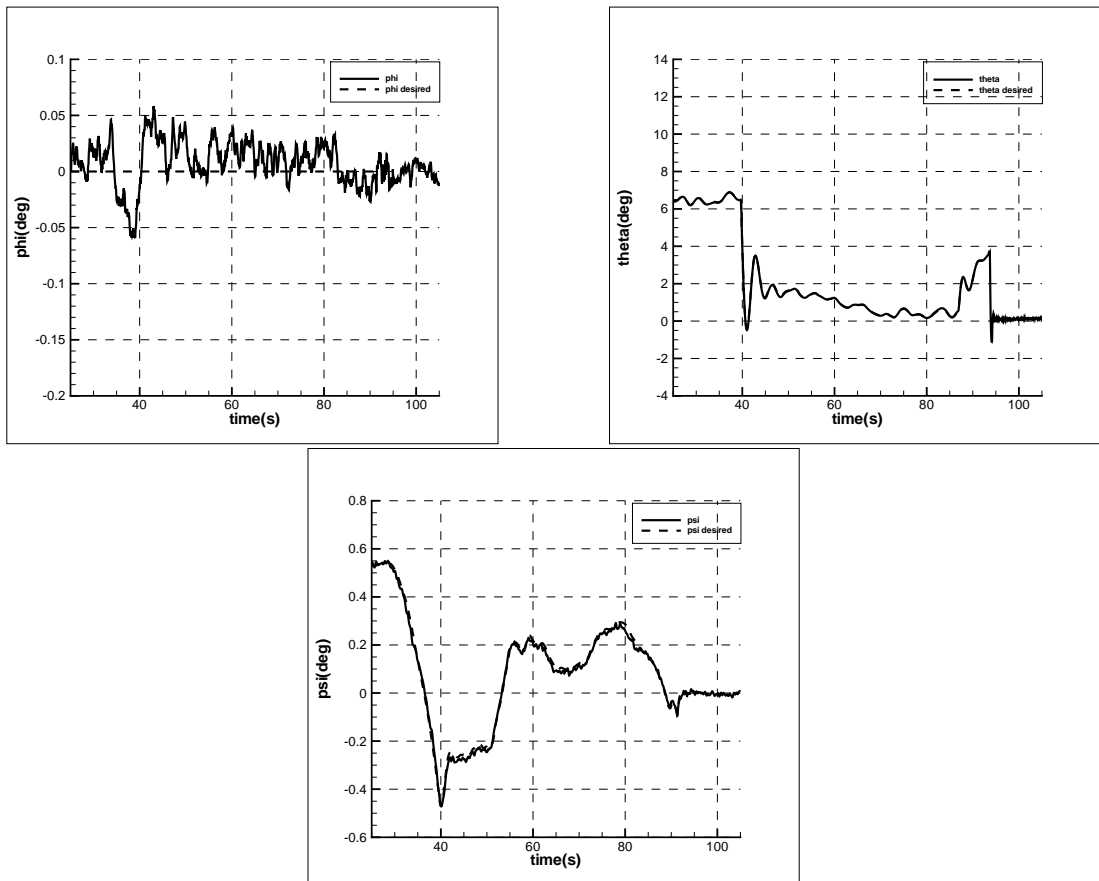


Figure 5.28: Euler angles

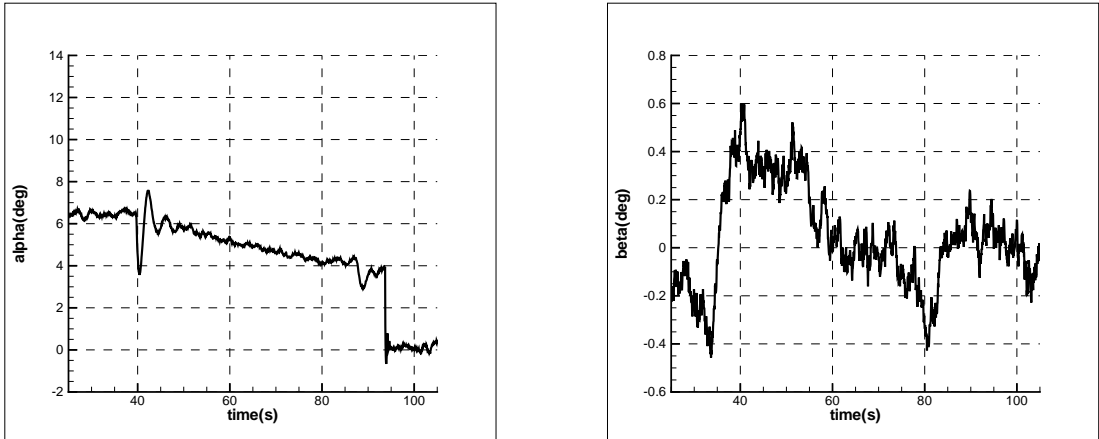


Figure 5.29: Angle of attack and sideslip angle

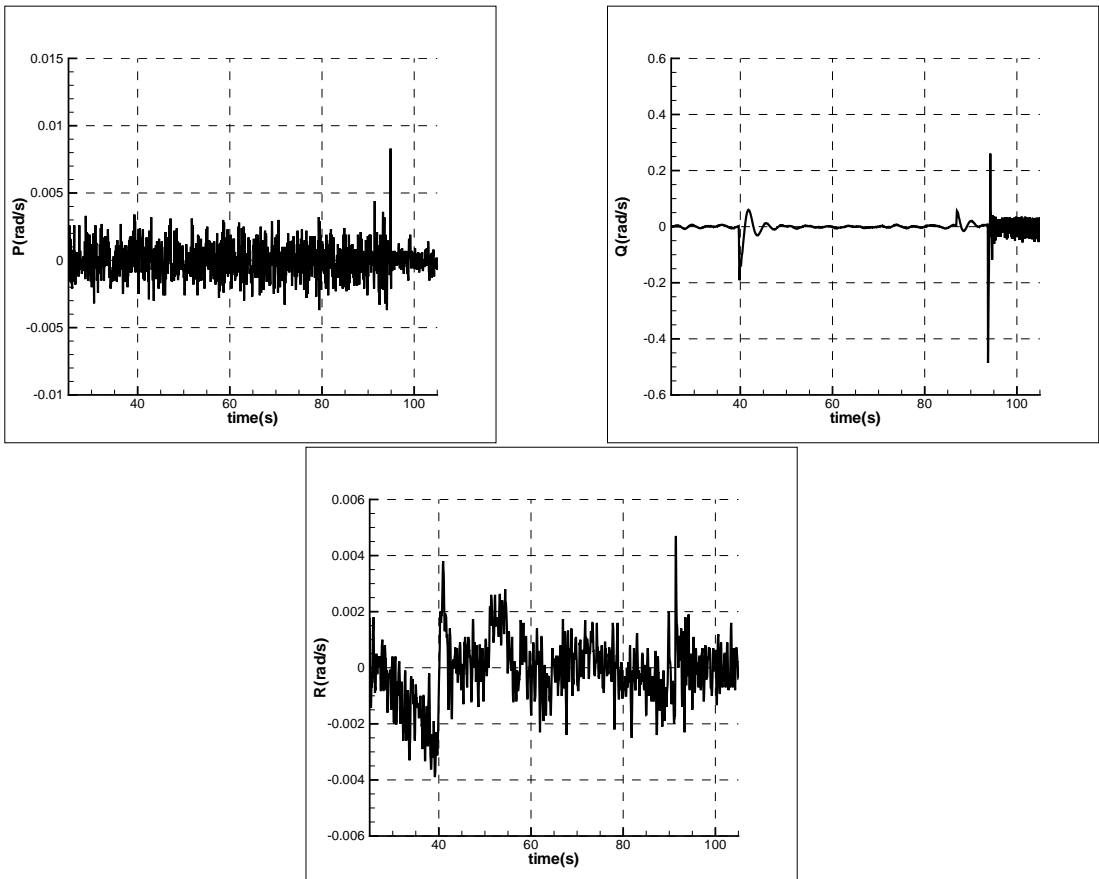


Figure 5.30: Body angular rates

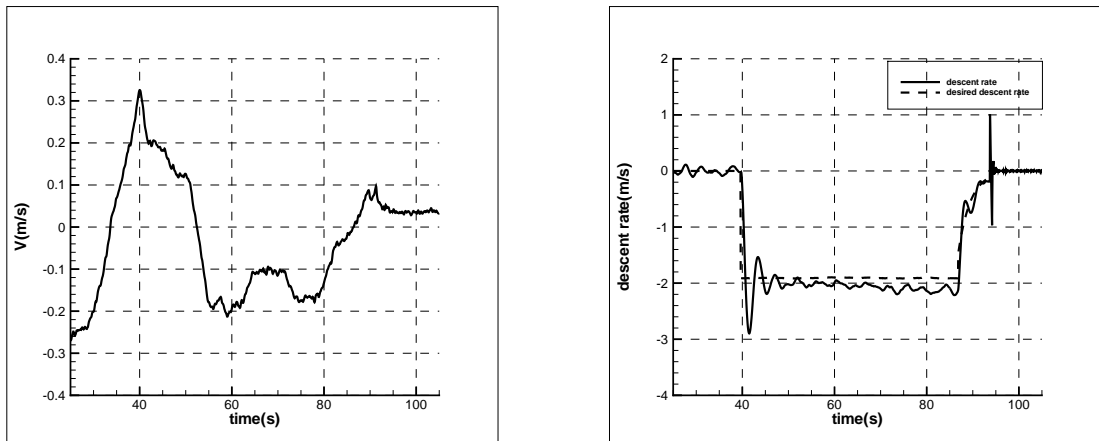


Figure 5.31: Side velocity and descend rate

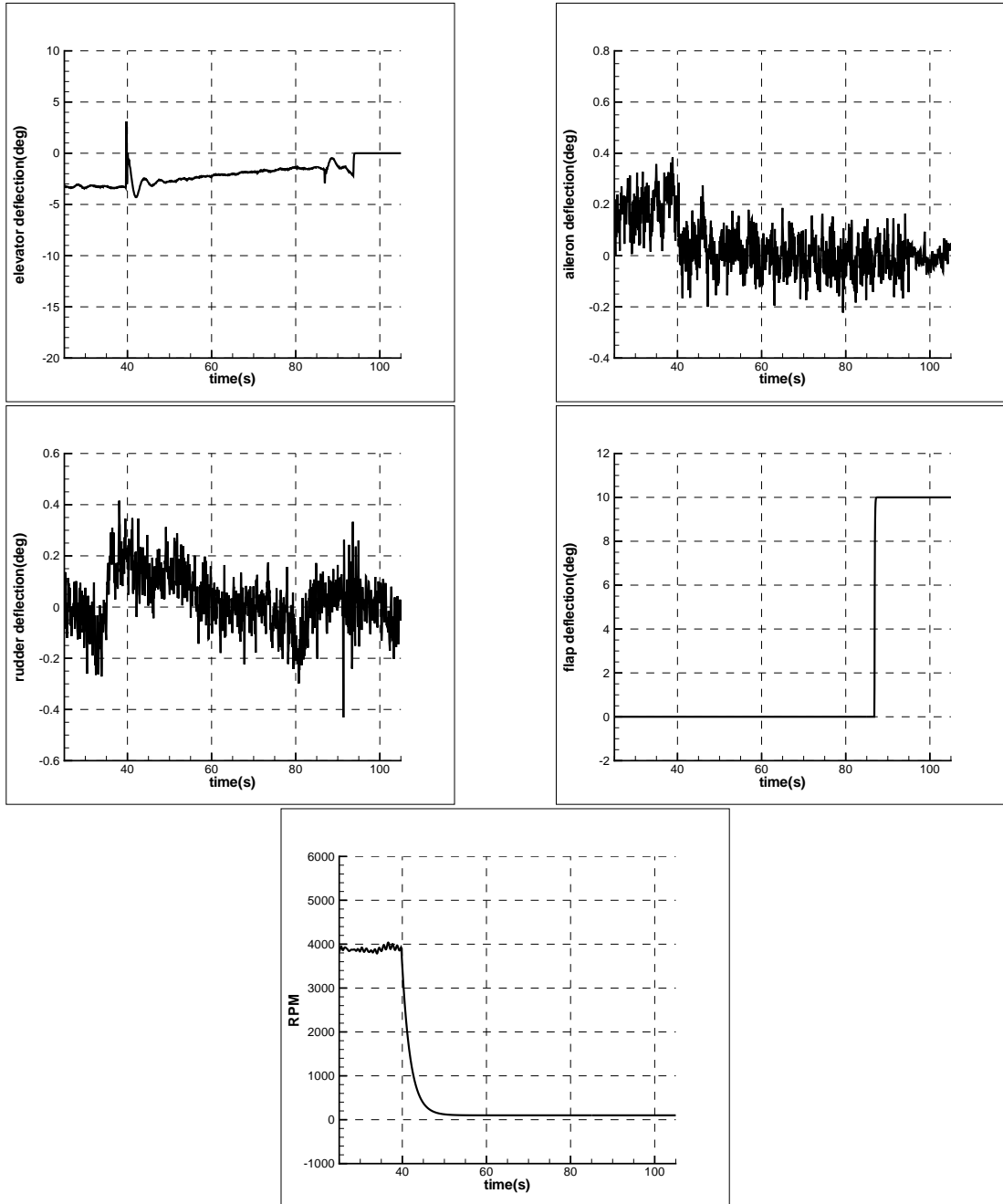


Figure 5.32: Control surface deflections

5.4 Case 4: 10 m/s Crosswind + Turbulence

Wind profile during simulation is given in Figure 5.33. Although aircraft follows the trajectory, there is a noticeable forward velocity error during descent due to throttle saturation (Figure 5.34). In crosswind simulations where there is no turbulence or light turbulence, such a saturation is not observed. In this simulation, A/C converges to a higher velocity than desired during descent because of turbulence and can not slow down later on even when rpm is reduced to its minimum value.

It is decided to change the flight path angle to 3 degrees. As seen in figures 5.38 and 5.44,

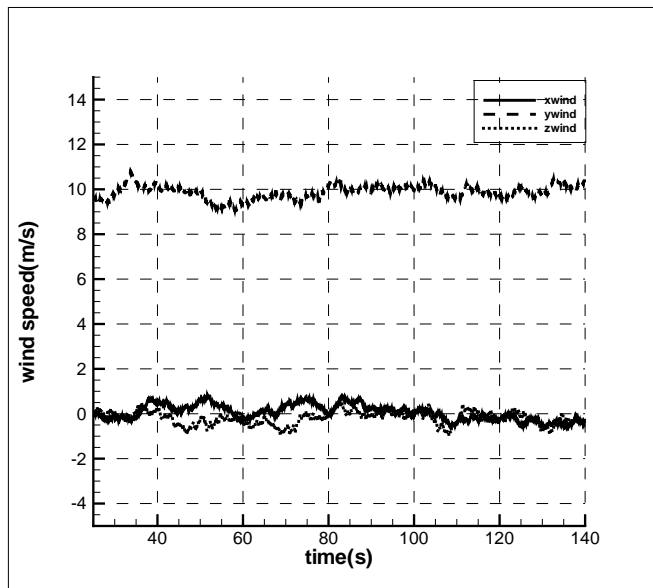


Figure 5.33: Wind profiles

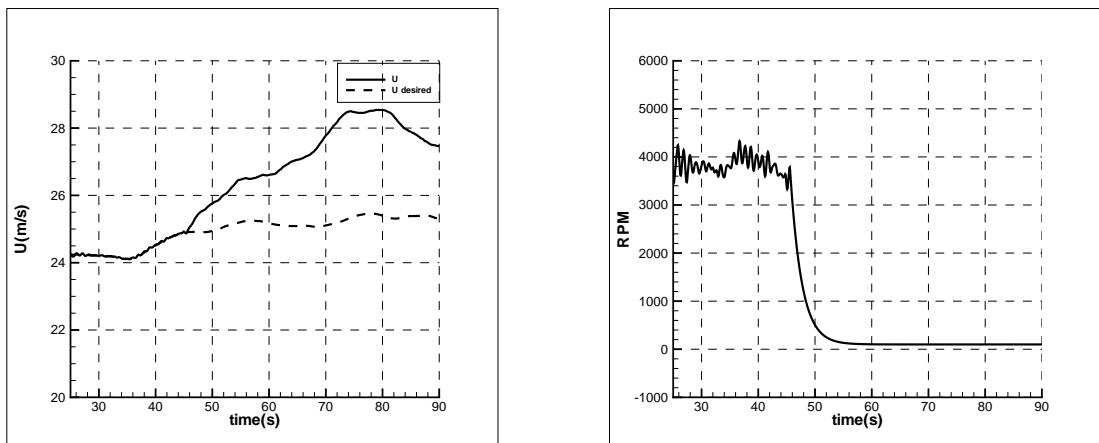


Figure 5.34: Forward velocity and rpm for $\gamma=3.5\text{deg}$

velocity is controlled by throttle although rpm reaches its minimum values between $t=50s$ and $80s$. Altitude error and lateral trajectory of the aircraft are given in Figures 5.36 and 5.37, respectively. It is observed that the A/C flies with a crab angle of -21 deg . The UAV approaches the flare height with no significant error in height or lateral position. The lateral position error never exceeds $5m$. Flare maneuver is initiated at $t=110s$, a pitch up motion is observed as usual. At the height of $1m$, $\psi = 0deg$ is commanded to reduce crab angle. Large rudder and aileron deflections can be observed at $t=118s$. In two seconds, the yaw angle reduces from -20 to a value less than -1 degrees, the side velocity reduces from 10 m/s to a value less than 2 m/s and roll angle is kept below $1deg$. Decrab maneuver results in a lateral deviation of $2m$ and loss of altitude. Touchdown occurs at $t=120s$. Descent rate is $0.3m/s$ which indicates a landing without damage.

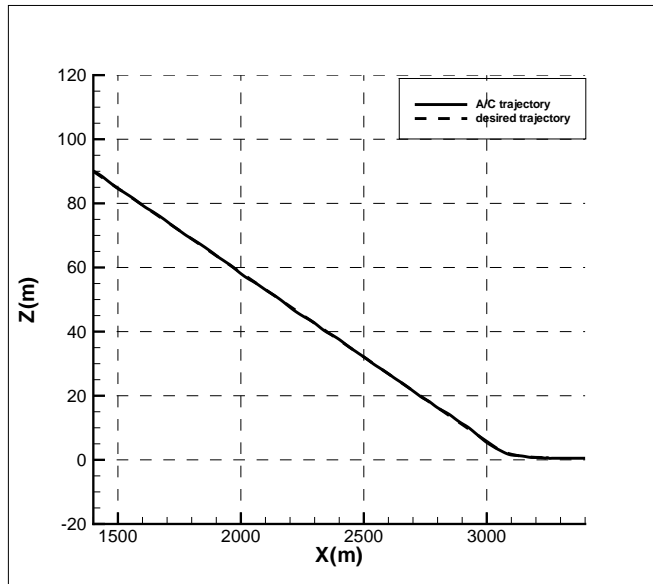


Figure 5.35: Longitudinal trajectory

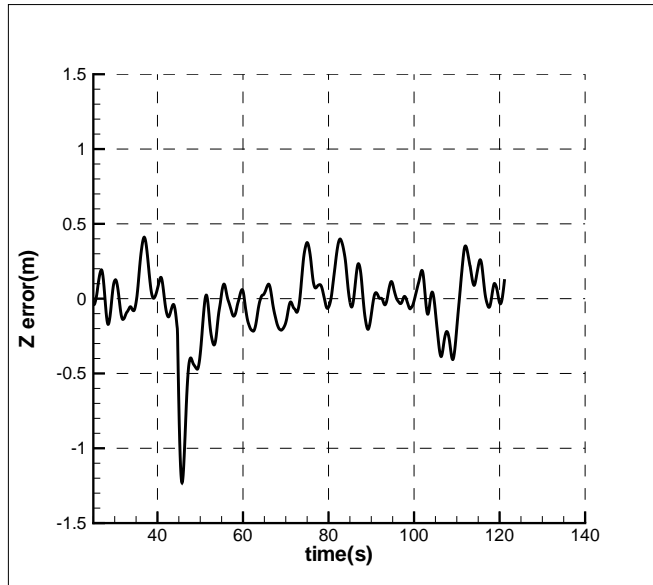


Figure 5.36: Altitude error

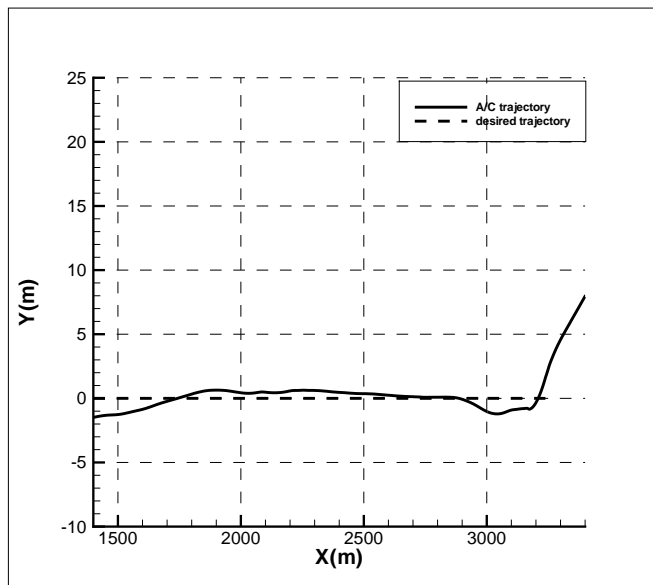


Figure 5.37: Lateral trajectory

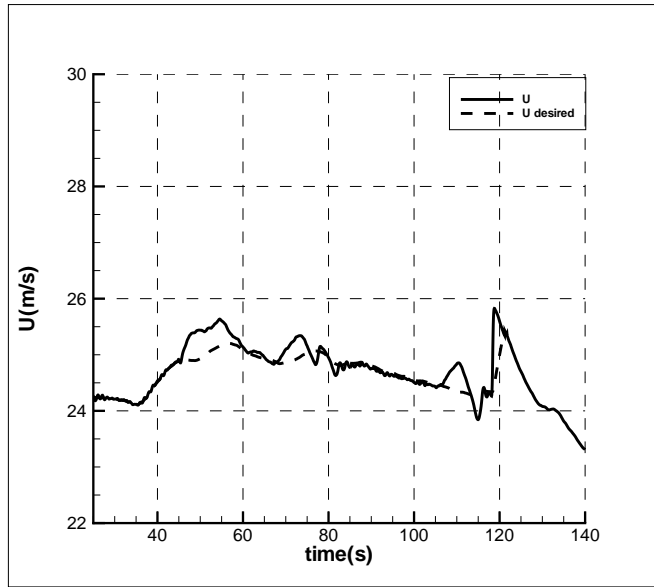


Figure 5.38: Forward velocity

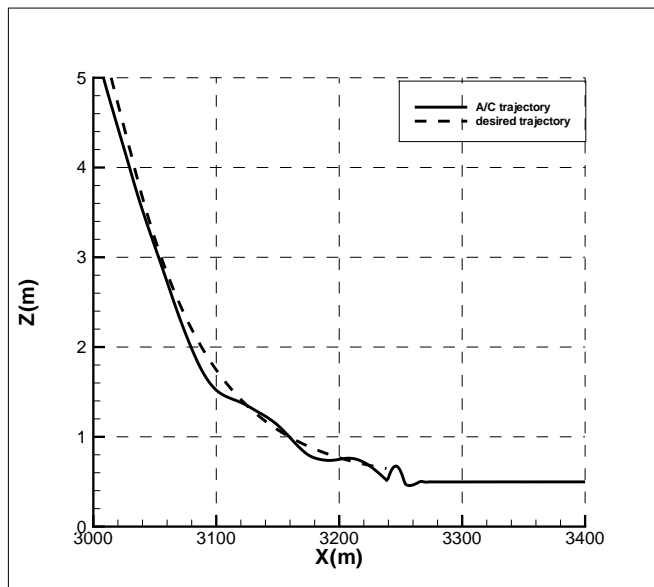


Figure 5.39: Flare maneuver

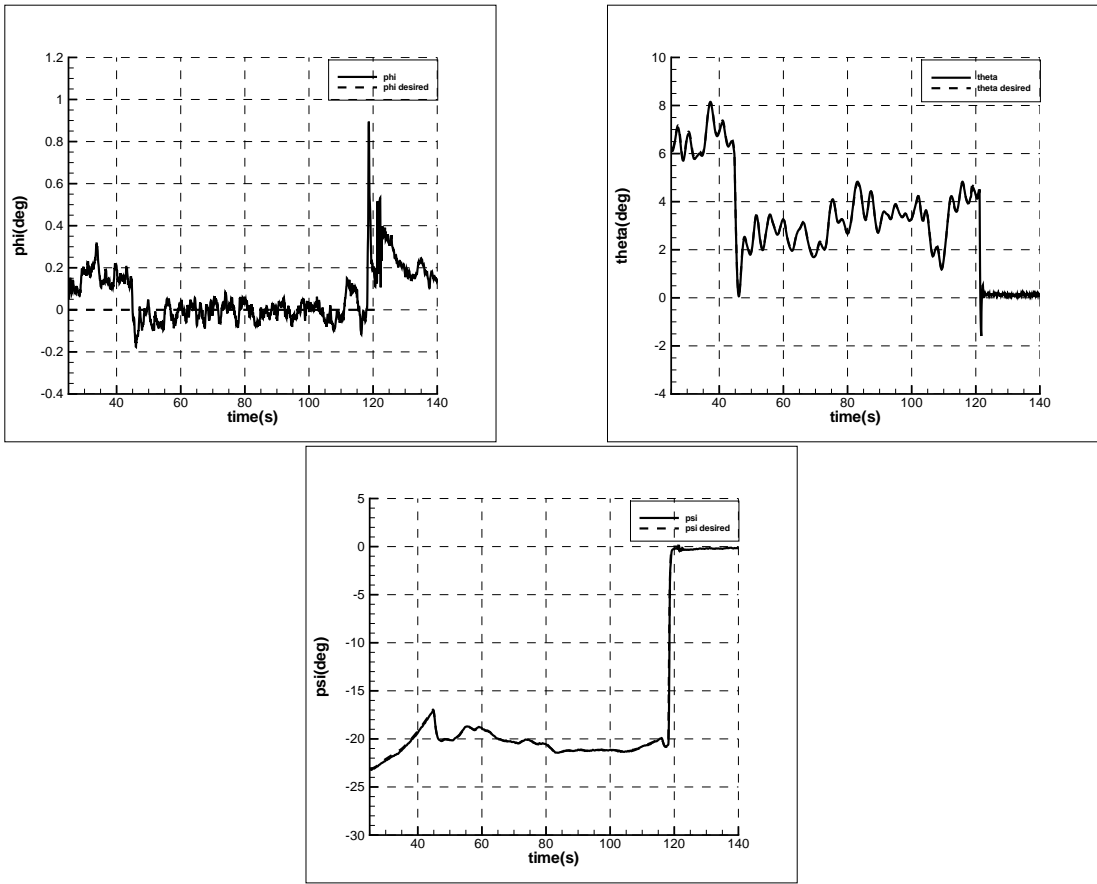


Figure 5.40: Euler angles

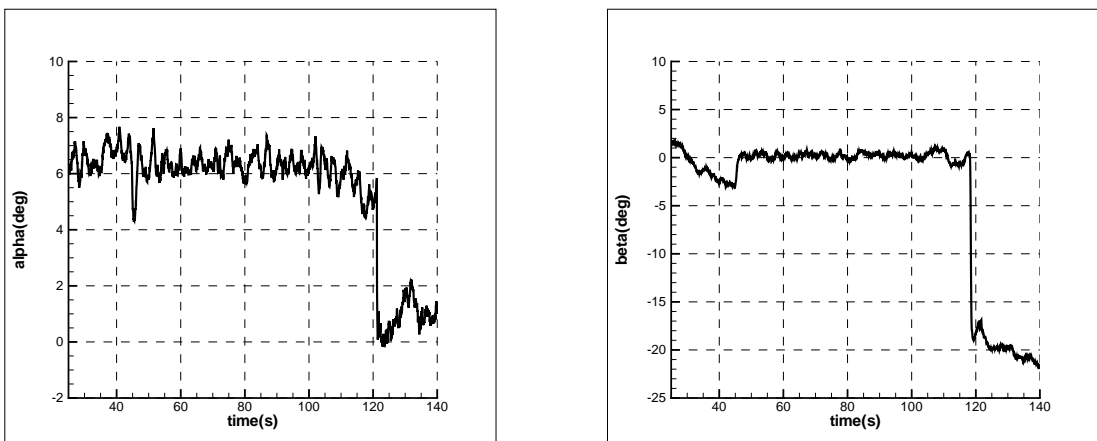


Figure 5.41: Angle of attack and sideslip angle

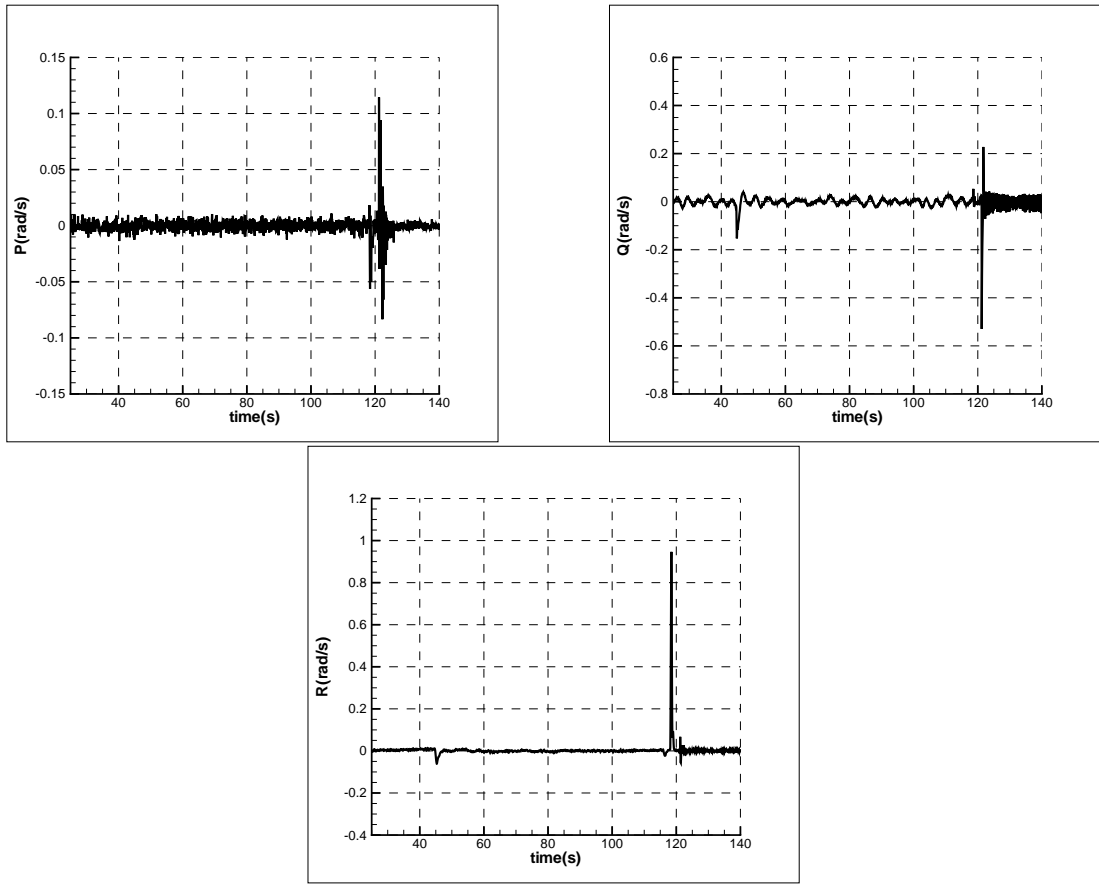


Figure 5.42: Body angular rates

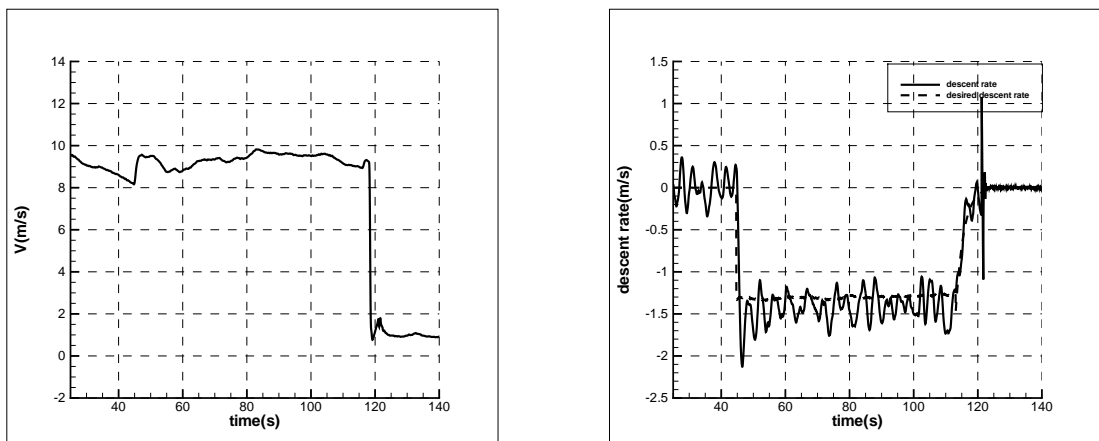


Figure 5.43: Side velocity and descent rate

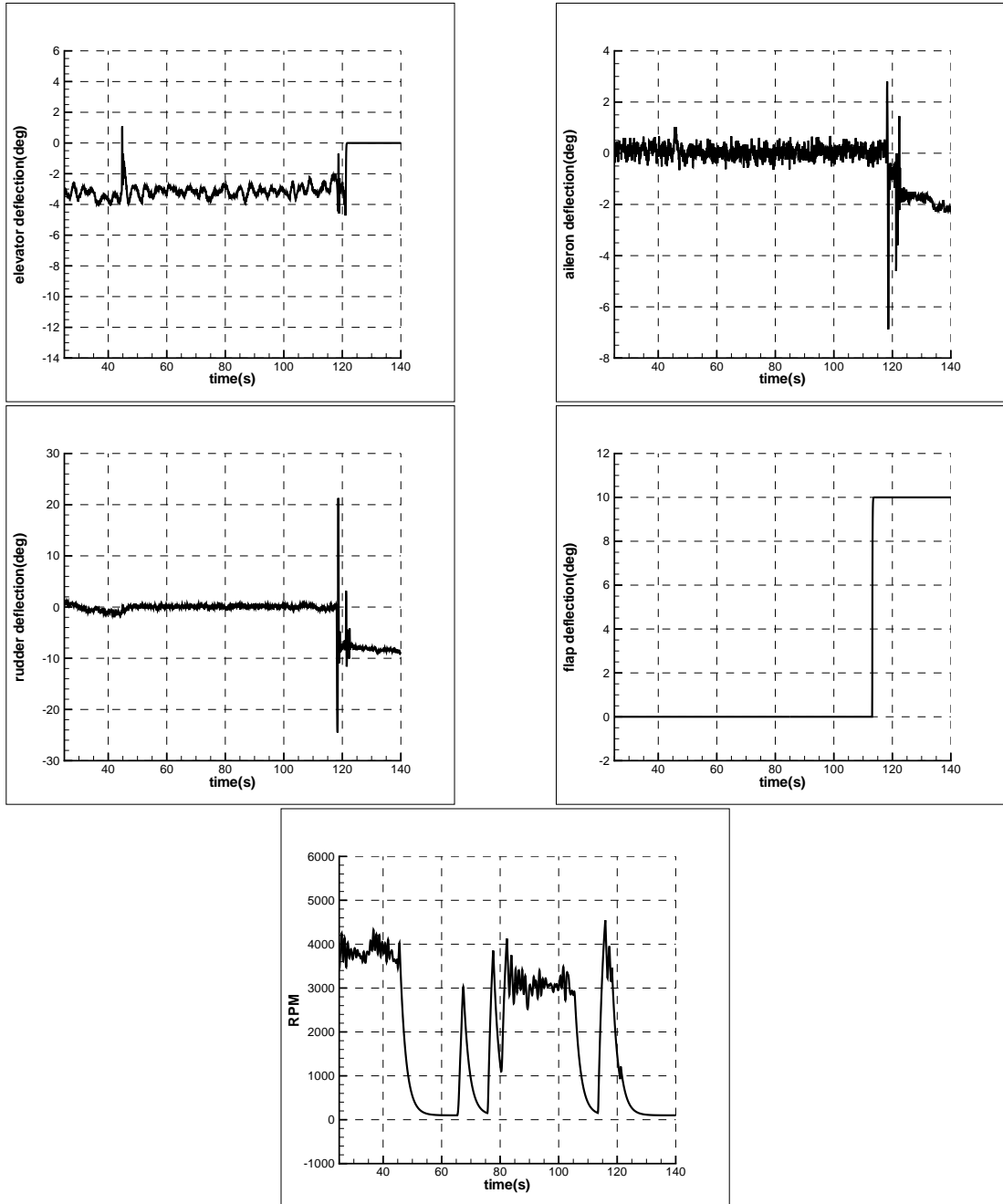


Figure 5.44: Control surface deflections

5.5 Case 5: Windshear + Turbulence

Wind profile of case 5 is shown in Figure 5.45. A/C is flying against a head wind which decreases with altitude and light turbulence. Lateral response of the controller is very good since there

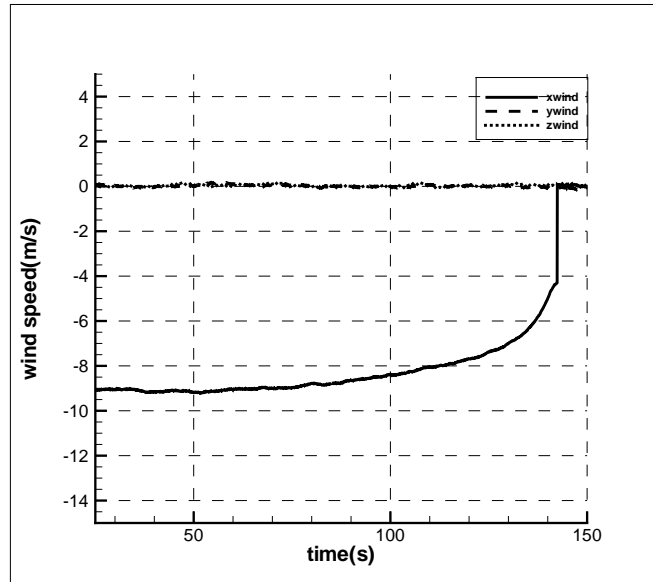


Figure 5.45: Wind profiles

is no dangerous disturbances in that direction. Altitude and velocity are controlled effectively in descent phase(Figures 5.47 and 5.49). At flare phase, the wind speed reduces from 6m/s to zero drastically. This decrease in airspeed causes loss of lift force on the UAV. Dynamics of the system is not fast enough to compensate this loss so, it descends and hits the ground with a downward velocity greater than 1m/s(Figure 5.54). This velocity is high for touchdown and the landing gears of the UAV might be damaged after such a landing.

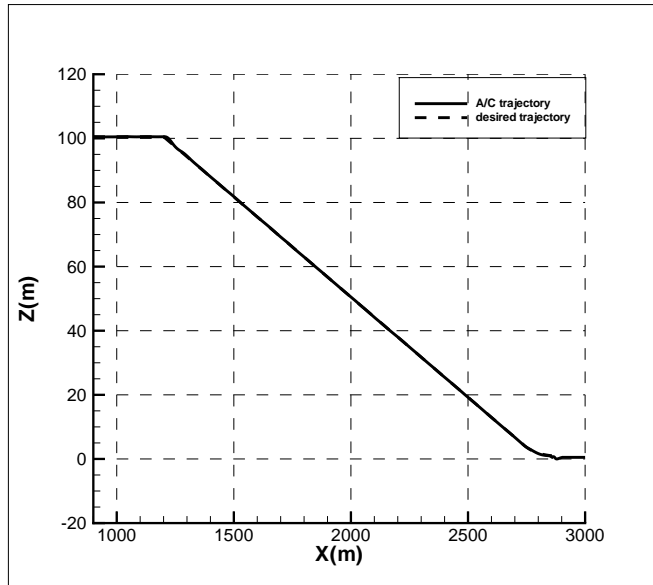


Figure 5.46: Longitudinal trajectory

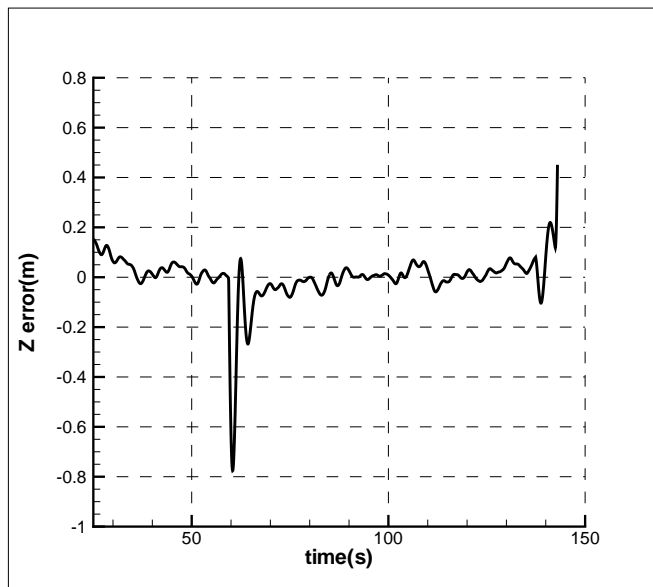


Figure 5.47: Altitude error

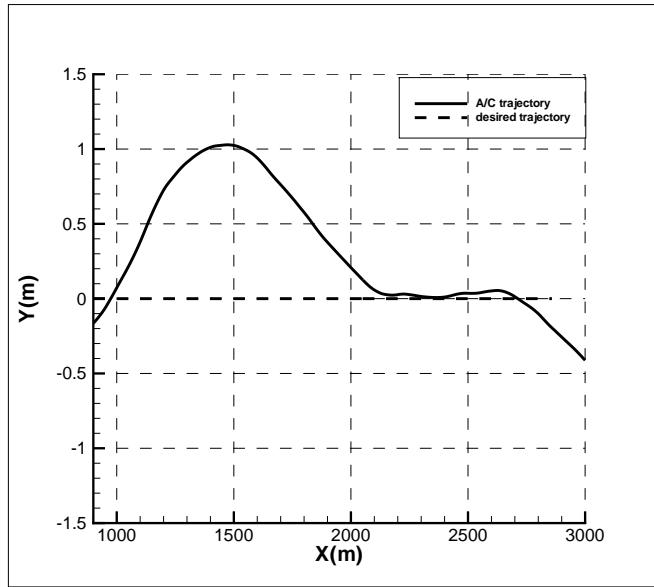


Figure 5.48: Lateral trajectory

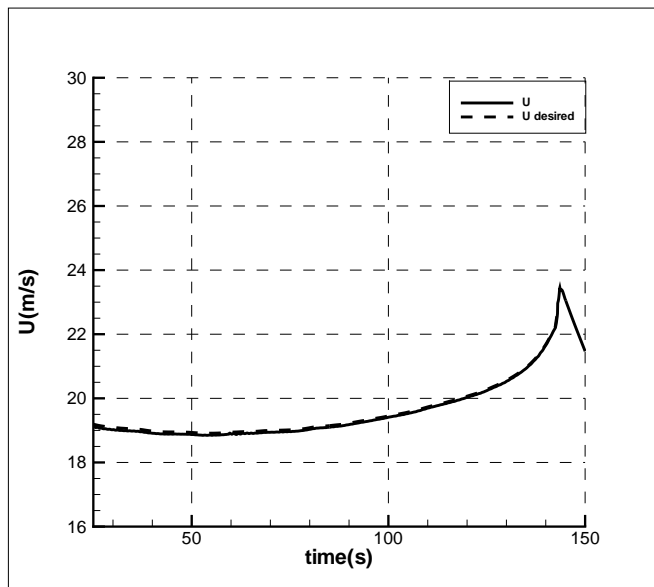


Figure 5.49: Forward velocity

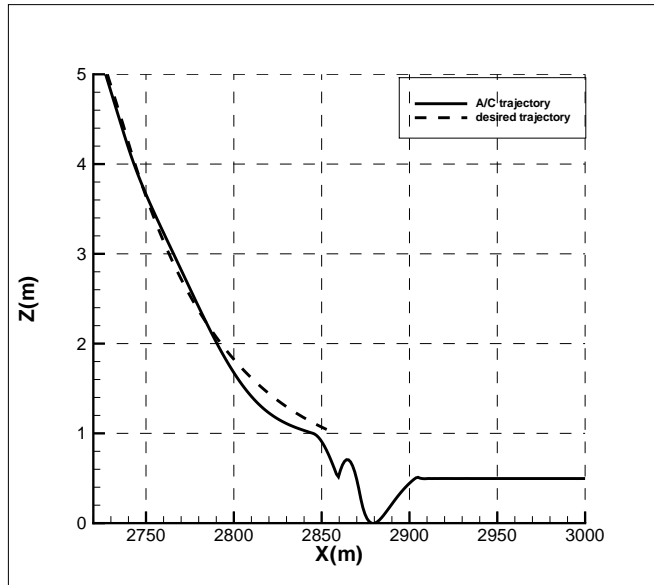


Figure 5.50: Flare maneuver

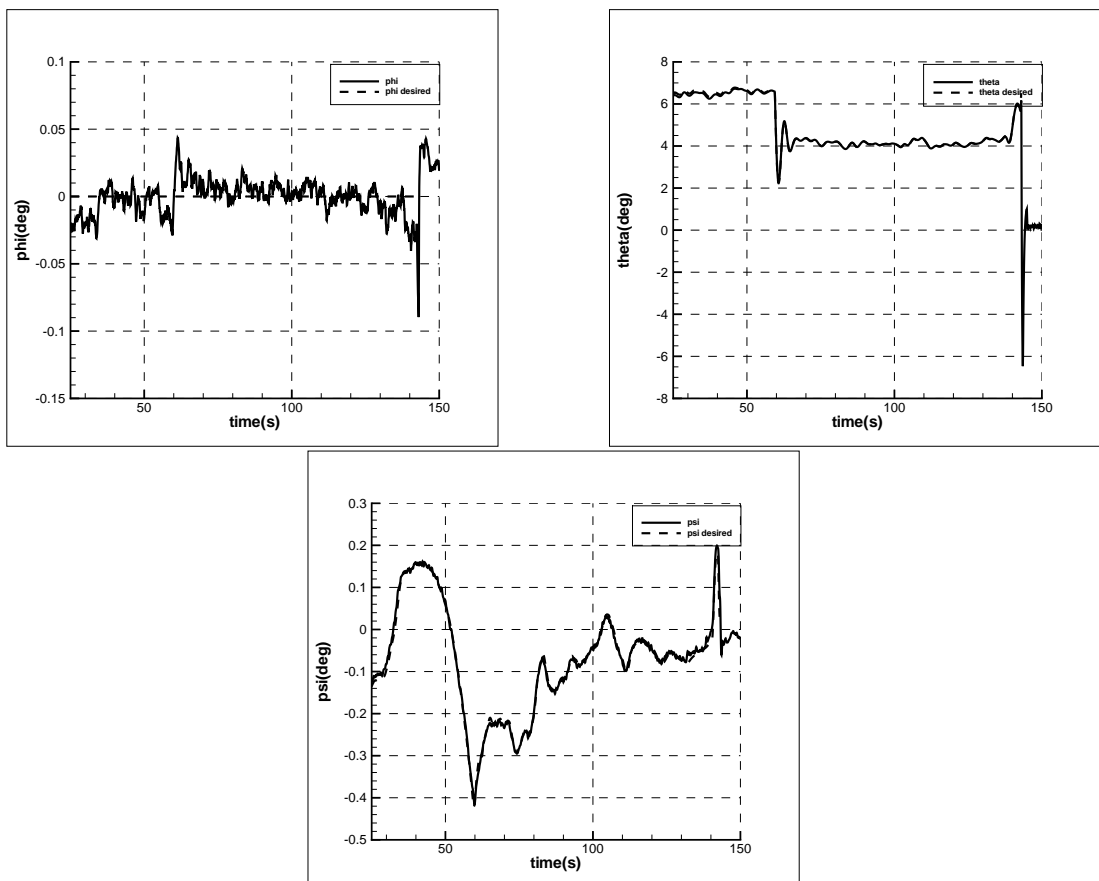


Figure 5.51: Euler angles

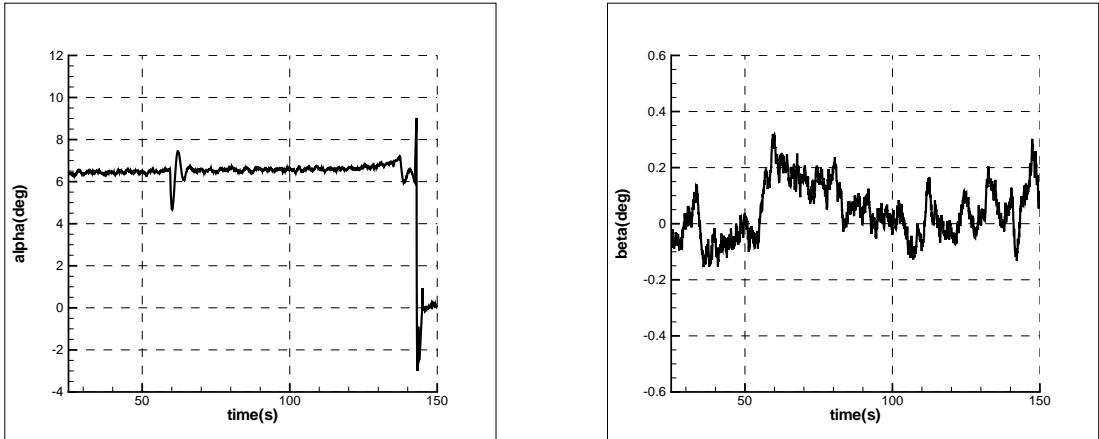


Figure 5.52: Angle of attack and sideslip angle

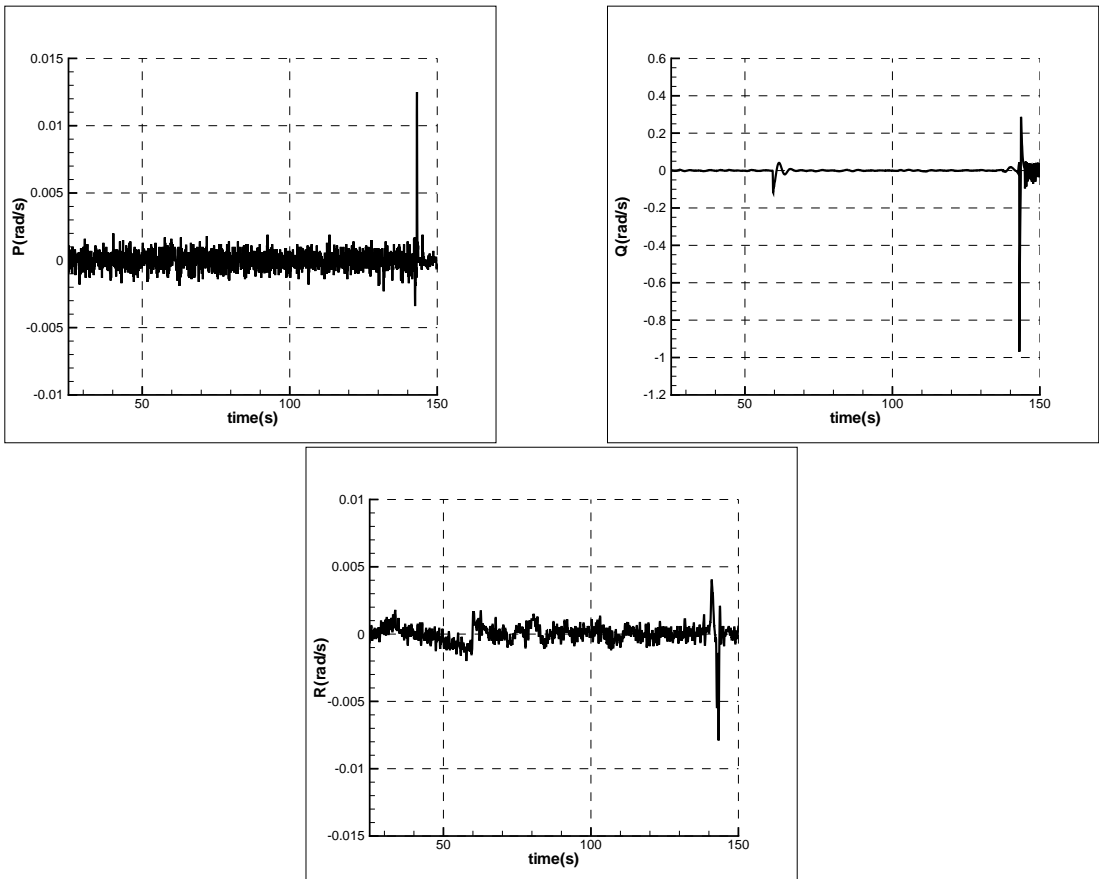


Figure 5.53: Body angular rates

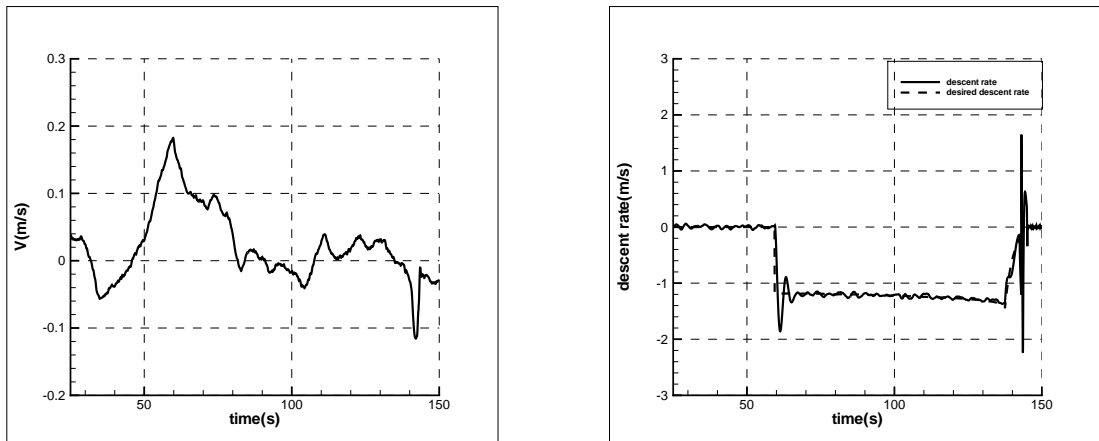


Figure 5.54: Side velocity and descend rate

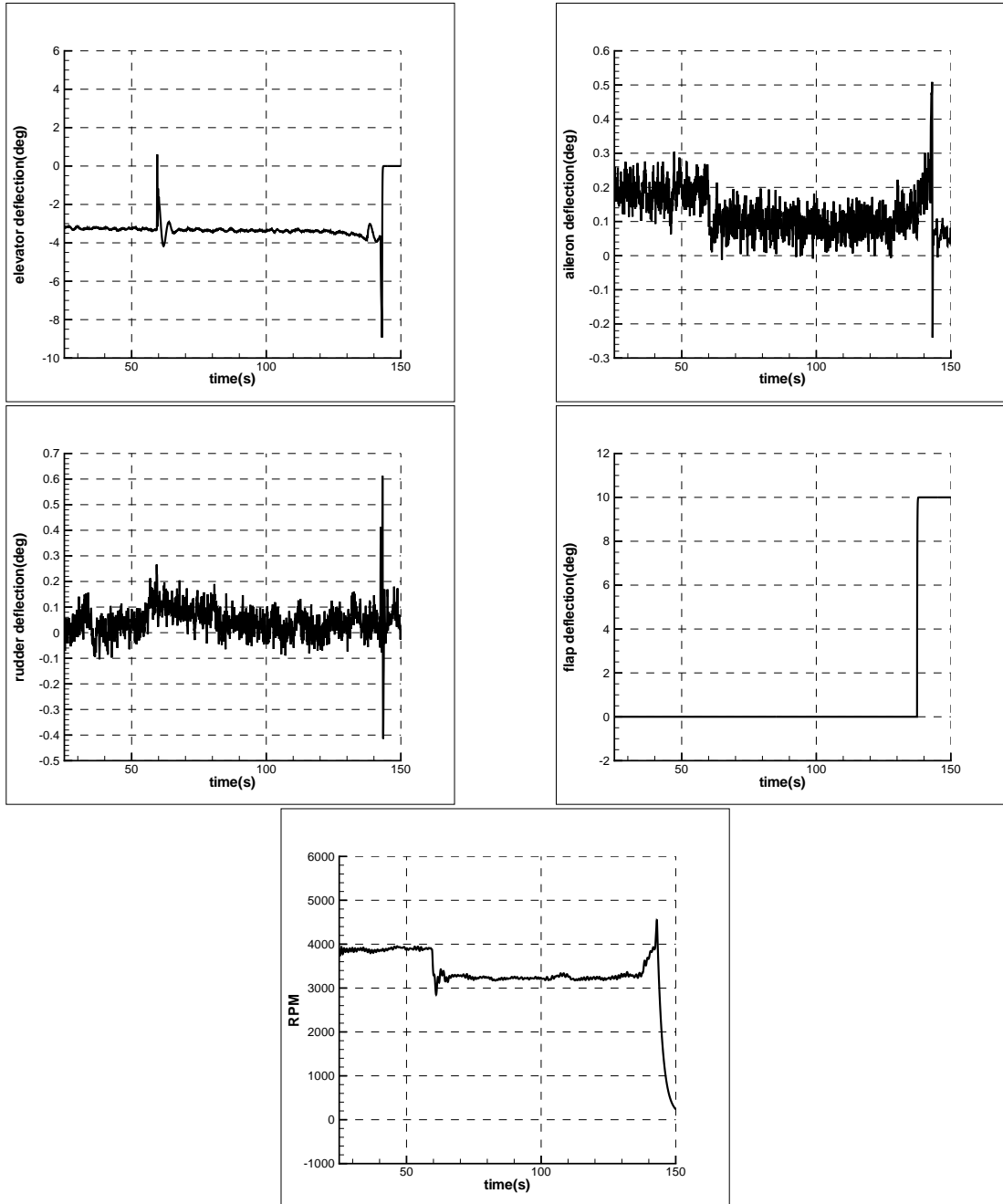


Figure 5.55: Control surface deflections

CHAPTER 6

CONCLUSION

In this study, control algorithms for the autonomous landing of a Tactical UAV are designed and their performances are investigated in simulations for landing scenarios when the UAV is subject to adverse weather conditions.

A focus of this thesis is to create a generic and accurate non-linear 6-DOF dynamic model of the METU TUAV. Aerodynamic, propulsion, ground reaction, mass-inertia, actuator models are generated in FORTRAN. These modules are modular enough to be updated based on geometric properties and characteristics of the aircraft. Atmosphere and wind-turbulence models are written to simulate a realistic environment. Longitudinal and lateral characteristics of the UAV are established by linearizing the nonlinear equations around trim points. All modes except the spiral mode are found to be stable. Results are verified through open loop simulations.

The flight controller is built in a two time scale fashion, an inner and an outer loop. The attitude of the UAV is controlled in the inner loops using model inversion based controllers. Although the inverted model was only valid for one flight condition the results were satisfactory. Improvements can be made by integrating adaptive neural networks to account for model uncertainties.

The translational dynamics are controlled in the outer loop. Special attention is paid to lateral the position control. Three different algorithms are considered and compared for lateral trajectory control. The controller where the cross track error was minimized by the rudder and the roll angle was minimized by the aileron produced the best results. Mixing is added between rudder and aileron in order to provide faster yaw convergence.

Controlling the forward velocity during descent using only the throttle turned out to be challenging. These limitations of the throttle response dynamics prevented landing with higher flight path angles. Moreover, as the attitude was not used for forward speed adjustment, the RPM control would quickly saturate to its minimum (no thrust value) if the descent trajectory was too steep to follow at a slow speed. It is suggested as future work to make use of the elevators during the descent period.

Simulations demonstrated that the UAV is able to land in all of the proposed adverse weather conditions and was able to follow the longitudinal and lateral position commands as well as the descent rate, yaw angle, roll angle and forward velocity commands. It is shown that the use of flaps, the addition of feed forward terms in the controller and the addition of mixing terms benefited the closed loop performance.

The following items are suggested for future work:

- The dynamic model can be verified using flight tests after METU TUAV is produced.
- A more accurate landing gear model can be build by examining the spring and damping coefficients of the landing gear through experiments.
- On board flight sensors, such as GPS, IMU, pressure sensors other basic flight instruments can be modeled to increase the fidelity of the model.
- The model can be implemented into the open source code Flight Gear for real-time sim-

ulation.

- Stability and performance of the system can be verified by adding frequency domain analysis.
- Adaptive controllers can be added to the controller to account for model uncertainty and hence eliminate gain scheduling. Adaptation might also help to land under even worse weather conditions.
- Mixing the elevator control into the forward speed controller loop.

REFERENCES

- [1] Jodeh, N. M., Blue, P. A. and Waldron, A. A. “*Development of Small Unmanned Aerial Vehicle Research Platform: Modeling and Simulating with Flight Test Validation*”, AIAA 2006-6261, 2006.
- [2] Hoak, D. E. and Ellison, D. E., et al. “*USAF Stability and Control Datcom, Unpublished*”, AF Flight Dynamics Laboratory, AFFDL-TR-79-3032, April 1979.
- [3] Roskam, J., “*Methods for Estimating Stability and Control Derivatives of Conventional Subsonic Airplanes*”, Roskam Aviation and Engineering Corporation, 1973.
- [4] Roskam, J., “*Methods for Estimating Drag Polars of Subsonic Airplanes*”, Roskam Aviation and Engineering Corporation, 1973.
- [5] Hoerner, S.F., “*Fluid Dynamic Drag*”, Midland Park, N.J, 1958.
- [6] Box, G. E. P. and Muller, M. E., “*A Note on the Generation of Random Normal Deviates.*”, Ann. Math. Stat. 29, p: 610-611, 1958,.
- [7] ESDU, “*Low Speed Longitudinal Aerodynamic Characteristics of Aircraft In Ground Effect*”, ESDU 72023, 1972.
- [8] Limbach Flugmotoren website, “<http://www.limflug.de/>”, as accurate of 10 August, 2007.
- [9] McCormick, B. W. “*Aerodynamics, aeronautics, and flight mechanics*”, Wiley, 1995.
- [10] Drela, M., “*XFOIL-Subsonic Airfoil Development System*”, ACDL research group webpage, MIT [online database] URL: <http://raphael.mit.edu/xfoil/>, 2004.
- [11] Ragsdale W. A., “*A Generic Landing Gear Dynamics Model For LASRS++*”, AIAA 2000-4303, 2000.
- [12] Roskam, J., “*Airplane Flight Dynamics and Automatic Flight Controls*”, Roskam Aviation and Engineering Corporation, 1979.
- [13] Unmanned Vehicle Systems International web site, “<http://www.uvs-international.org/>”, as accurate of February 23rd, 2007.
- [14] Kotwani, K., Sane, S. K., Arya H. and Sudhakar, K., “*Performance Mapping of Mini Aerial Vehicle Propellers*”, Indian Institute of Technology, Bombay, India, 2004.
- [15] Pashilkar, A.A., Sundararajan, N. ,Saratchandran, P., “*A Fault-Tolerant Neural Aided Controller for Aircraft Auto-landing*”, Aerospace Science and Technology, Volume 10, Issue 1, January 2006.
- [16] Niculescu, M., “*Lateral Track Control Law for Aerosonde UAV*, AIAA 2001-0016, 2001.
- [17] McLean, D., “*Automatic Flight Control Systems*”, Prentice Hall, 1990.
- [18] Riseborough, P., “*Automatic Take-off and Landing Control for Small UAV's*”, 5th Asian Conference, 2004.

- [19] Attar, M., Wahnon, E., Chaimovitz, D., “*Advanced Flight Control Technologies for UAV’s*”, AIAA 2003-6537, 2003.
- [20] Azinheira, R., de Pavia, E.C., Ramos, J.G., Bueno S.S., “*Mission Path Following for an Autonomous Unmanned Airship*”, IEEE International Conference on Robotics & Automation, San Francisco, CA, April 2000.
- [21] Lizarraga, M.I., “*Autonomous Landing System for a UAV*”, Naval Postgraduate School, Monterey, CA, March 2004.
- [22] Rosa, P., Silvestre C., Cabecinhas, D., Cunha, R., “*Autolanding Controller for a Fixed Wing Unmanned Air Vehicle*”, AIAA Guidance, Navigation and Control Conference, South Carolina, 2007.
- [23] Hsiao, F.B., Chan, W.L., Lai, Y.C., Tseng, L.C., Hsieh, S.Y., Tenn, H.K., “*Landing Longitudinal Control System Design for a Fixed Wing UAV*” AIAA Aerospace Sciences Meeting and Exhibit, Nevada, 2007.
- [24] Malaek, S.M.B., Sadati, N., Izadi, H., Pakmehr, M., “*Intelligent Autolanding Controller Design using Neural Networks and Fuzzy Logic*”, 5th Asian Conference, 2004.
- [25] American Meteorological Society web site, “<http://amsglossary.allenpress.com/glossary/>”, as accurate of August 28rd, 2007.
- [26] “*U.S. Military Specification MIL-F-8785C*”, 5 November 1980.
- [27] Calise, A.J., Rysdyk, R.T., “*Adaptive Model Inversion Flight Control for Tiltrotor Aircraft*”, AIAA Guidance, Navigation and Control Conference, August 1997.
- [28] Johnson, E.N., Turbe, M.A., Wu, A.D., Kannan, S.K., Neidhoefer, J.C., “*Flight Test Results of Autonomous Fixed-Wing UAV Transitions to and from Stationary Hover*”, AIAA Guidance, Navigation, and Control Conference and Exhibit, August 2006.
- [29] MIT OpenCourseWare web site, “*Aircraft Lateral Autopilots*”, MIT URL: <http://ocw.mit.edu/OcwWeb/Aeronautics-and-Astronautics/16-333Fall-2004/>, as accurate of September 1st, 2007.
- [30] Etkin, B., Reid, L.D., “*Dynamics of Flight: Stability and Control*”, John Wiley & Sons, Inc., 1995.
- [31] Stanford University Aerodynamics and Design Group web site “*Dynamics Stability*”, Stanford University URL: <http://adg.stanford.edu/aa241/stability/dynamicstability.html>, as accurate of September 2nd, 2007.
- [32] Donohue, C., “*NASA Study To Use a Predator B-class Unmanned Aerial System (UAS) In Support Of Arctic/Antarctic Polar Missions*”, Antarctic Meteorological Observation, Modeling and Forecasting Workshop, 13-15 June 2006. fff
- [33] Nelson, R.C., “*Flight Stability and Automatic Control*”, McGraw-Hill, 1998.
- [34] Clark, D., “*Approach and Landing Accident Reduction (ALAR) and Energy Management*”, Mobility Forum, 2005.
- [35] Flight Safety Foundation, “*FSF ALAR Briefing Note 8.1- Runway Excursions and Runway Overruns*”, 2000.
- [36] Karakaş, D., Orhan, E.H., “*OİUH Sınıfı bir İnsansız Hava Aracının Doğrusal Olmayan Dinamik Modelinin Oluşturulması ve Otomatik Uçuş Kontrol Sistemi Tasarımı*”, TAI - Tusas Havaçılık ve Uzay Sanayii A.Ş., 2006.
- [37] Ippolito, C., Yoo-Hsui, Y., Kaneshige, J., “*FSF Neural Adaptive Flight Control Testing on an Unmanned Experimental Aerial Vehicle*”, AIAA, 2007.
- [38] Ross, A., “*Modeling and Control of the SiMiCon UAV*”, Master of Engineering Thesis, University of Glasgow, 2003.